Changes in Subsurface Hydrological Systems Produced by Earthquakes: Observations from Borehole Monitoring

孔内観測記録を用いた地震に伴う地下浅部の水理特性変化の推定

CHIHIRO KINOSHITA

Division of Earth and Planetary Sciences, Graduate School of Science,

Kyoto University

December, 2017

Abstract

Monitoring of pore pressure in the boreholes is comparable to measurement of strain and stress in a rock mass. Interstitial fluids have been considered as one of the triggering factors of earthquakes and direct measurement of them are important. Although borehole observations have depth limitations, the fundamental mechanical effects of fluids on rock deformation as observed in boreholes, is likely representative of the hydrological system. Then, the behavior of the subsurface water could offer important clues to understanding the fluids and stresses of deeper seismogenic zones.

In this thesis, I mainly used the data of pressure and groundwater level observed in onshore and offshore boreholes located in Japan (measured instrumental quantity is the same for both pressure and water level). Changes in pore pressure in a rock mass is related to the volume of pore space and amount of fluids. It is usually difficult to distinguish these properties in observed pressure data, but the required times for propagation of changes in pore volume and fluid diffusion are different, and this feature provides information for distinguishing properties of hydrological system and physical properties of rock mass such as permeability and hydraulic diffusivity.

I first focused on the appearance of coseismic and postseismic responses of pressure. The former reflects mainly volume changes in pore space and the latter is produced by fluids diffusion. By utilizing changes in tidal response to pressure and volumetric strain variations, we could follow the time series of physical properties of a rock mass. At the time of the 11 March 2011 Tohoku earthquake (Mw 9.0), very large changes in pressure were recorded at both onshore and offshore sites, and inferred associated changes in physical properties were also remarkable. For the onshore sites, these changes were observed at 500-1000 km from the epicenter, and the detailed analyses suggest that the static strains produced by the mainshock was large enough to detectably affect the hydrological systems located within 500-600 km from the epicenter. This result reverses the general idea that static strain cannot be effective at such large distances. In contrast, the effects of dynamic strains might have been

dominant at more than 700-800 km distances.

Changed pressure and physical properties of rock mass at the time of earthquakes tend to return to original values, which is a recovery process. The recovery process suggests that there is a preferential hydrological condition for a local region. For a specific region we searched for a weak point of an aquifer, where changes in water head preferentially occur and induce fluid flow. In the study region, our results suggest that fluid flow from the mountain to borehole was similarly triggered by various earthquakes and follows the simple diffusion equation.

For the oceanic boreholes, there have been recordings of several types of interesting signals, including seismic events and pressure perturbations produced by drilling and coring operations at nearby sites. For relatively large earthquakes, clear step changes in pore pressure as well as the change in physical properties, such as loading efficiency are observed. In order to explain the time-dependent changes in the loading efficiency, I suggest that gas may play an important role in modifying the response of the pore pressure. Interactions between the rock matrix, fluid and gas may explain the observed pore pressure changes.

Unexpectedly observed pressure changes recorded by an ocean borehole observatory and produced by nearby drilling operations, provided an opportunity similar to a cross-hole test. The pressure changes recorded about 100 m from the drilling site were modeled using a simple diffusion model and enabled estimates of permeability between the two boreholes. Combining these results with previous estimates of permeability for distances of centimeters to meters, indicate a scale dependence of the permeability. The permeability over distances of about 100 m is 5 to 6 order of magnitude larger than

at centimeter to meter scales.

Changes in pressure and associated physical properties strongly depend on site-specific characteristics. Even for observed hydrological perturbations that are similar at sites, the mechanisms may be different. In this thesis, I proposed several types of mechanisms that illustrate the observed hydrological perturbations and recovery to the original levels, by integrating the hydrologic, seismic and geological data. The various results in this thesis from onshore and offshore hydrological observations show the valuable information gained from borehole observations on the fluid and stress conditions in seismogenic zones along with the importance of integrated studies and observations.

Contents

List of Figures

List of Tables

Chapter 1. Introduction

Hydrological perturbations produced by earthquakes have been observed as variety of different phenomena, including changes in groundwater level, flow rate in springs and rivers, chemical composition of groundwater, and liquefaction (e,g., Roellofs, 1996; Igarashi and Wakita, 1991 (groundwater level); Brown et al., 2005 (flow rate)). In some cases, they produce greater damage to society than the main shocks, such as drying up wells, disappearing geysers and eruptions of mud volcanoes, which cannot be ignored for societal safety (e.g., Greene et al., 1991; Yasuda et al., 2013). Revealing their underlying mechanisms and reducing the risks of disasters are an important role of hydrogeology.

In addition, we believe that study of hydrological system in the subsurface could lead to the understanding of fluids behavior in the deep underground, such as in seismogenic zones (10-20 km). One mechanism that promotes earthquake occurrence is decrease of effective normal stress on fault by pore pressure increase;

$$\sigma = \sigma_0 - p_p \tag{1.1}$$

where σ is effective normal stress, σ_0 is normal stress and p_p is pore pressure (Hubbert and Rubey, 1959). If we assume that normal stress is relatively constant with time, monitoring of pore pressure corresponds to measurement of effective stress, which could provide valuable evaluations of imminent

earthquake occurrences. For these measurements, the depths of boreholes are important and current observations are relatively shallow. Improved observations should enable monitoring of pore pressure in the rock mass directly in the future.

Anomalies of pore pressure associated with the external forces such as earthquakes have been reported for a long time. Much previous pore pressure monitoring has been done by measurements of water table in the wells. In the past, many people with their own wells for domestic, agricultural or industrial uses, have checked the water level daily and, noticed anomalies in groundwater before or after seismic events (e.g., Hydrographic Bureau, 1948). In particular, earthquakes with larger magnitudes and/or closer epicentral distances tend to produce discernible changes in the groundwater. For the older observations, even though there were no precision observatories, such as those at the present, anomalies of groundwater were observed visually (Hydrographic Bureau, 1948; Onoue et al, 2005), which suggest that large and clear changes were occurred. The 1946 Nankai earthquake (M 8.1) that occurred offshore of southwest Honshu in Japan was also accompanied by precursory hydrologic phenomena. The Hydrographic Bureau (1948) reported the testimonies of witnesses who recognized anomalies in their wells. Based on these accounts, some wells that showed a decrease in groundwater, were located on the Pacific coast from the Kii Peninsula to Shikoku, western Japan, with epicentral distance of less than 100 km. In addition, turbidity and decreases in discharge of hot spring water were observed at nearby sites before this earthquake. The distribution of reported groundwater

anomalies are mostly decreases and may correspond to an uplift or tensile stress field (Onoue et al., 2005).

The 1964 Alaska earthquake (Mw 9.2) produced large changes in groundwater at more than 1450 sites in the United State (Waller, 1966; Vorhis et al., 1967). The variation of pressure corresponding to coseismic water level changes of 7 m was observed near Belle Fourche, South Dakota, and other wells also indicated changes in groundwater by more than 3 m. The effects associated with this event are seen globally, such as in England, Egypt and the Philippine Islands (Vorhis et al., 1967), and are likely produced by propagation of seismic waves. In another case, there have been reports of changes in behavior of subsurface water caused by the 1989 Loma Prieta earthquake that may have had an effect on the long drought conditions at that time in California (Manga, 2001). This event provided an increase in discharge rate by a factor of more than 20, and resulted in an improved hydrological system in many aquifers (Rojastaczer and Wolf, 1992).

Observations of underground fluid using boreholes have been developed not only onshore, but also offshore. Development of oceanic boreholes for pressure monitoring as part of the Integrated Ocean Discovery Program (IODP; formerly Integrated Ocean Drilling Program) have been performed in Cascadia, Barbados, Juan de Fuca Ridge, Mariana flank, Costa Rica Rift south flank, and Nankai Trough (Becker and Davis, 2005). Although the number of boreholes offshore is much smaller than that of onshore, but important results such as changes in pore pressure associated with slow slip events

(SSEs) and tremor have been observed (Davis et al., 2011; Araki et al., 2017).

There are many reports of changes in pressure and groundwater level associated with seismic events, and understanding these mechanisms are required to understand the hydrological system in the subsurface. In this thesis, I mainly analyzed the data of pore pressure and groundwater level recorded in the boreholes. Using data from both land and ocean boreholes, the results of the studies in this thesis contribute to a better understanding of the changes in the hydrological system associated with tectonic stress.

At the time of the 11 March 2011 Tohoku earthquake (Mw 9.0) that occurred off the coast of northeast Japan, changes in groundwater level were observed throughout Japan, and some of these observation sites obtained the largest changes ever recorded. In Chapter 2, we described the details of change in pore pressure and groundwater level associated with this megathrust earthquake. By extracting the tidal responses from observed pore pressure and strain data, changes in physical properties of the local rock mass associated with the Tohoku earthquake were determined, which implies that the aquifers around the boreholes were badly damaged.

In Chapter 3, we investigated the existence of a preferential perturbation of a hydrological system, which indicates that the behavior of groundwater changes is always the same regardless of earthquake focal mechanism and distance. From the simple diffusion equation, the source of the first change in water head in the aquifer can be located. Our results indicate that the sources estimated from all the

changes in groundwater level are located at almost the same distance from the observation borehole and can be explained by the geological features of the observation site.

Borehole monitoring in the oceans has a relatively short history compared to onshore measurement, and it is unclear what physical effects are reflected by the observed pressure changes and how the pressure relates with seismic events, although these observations provide exciting opportunities for future research. In Chapter 4, we documented fundamental behavior of pore pressure monitored in an offshore borehole, especially focusing on the coseismic responses. By comparison with geophysical observations such as coring, physical logging and in-situ experiments, the details of the underground become clearer. As an integrated study of various observations, we focused on permeability in the rock mass and described the scale dependence of the permeability, in Chapter 5.

In this thesis, I use mainly pore pressure and groundwater level data, which are relatively simple measurements but they include invaluable geophysical information of underground, especially using various techniques. By integration with other geophysical and geological data, potential mechanisms of the hydrological perturbations are inferred. Relationships between earthquakes and fluid have been discussed for a long time, and pore pressure in a rock mass and groundwater levels can be measured directly as representative of the fluid behavior in the subsurface. To fully understand and simulate the hydrological systems of the deep seismogenic zones in future, we first have to understand the behavior of shallow subsurface water.

Chapter 2. Shallow Crustal Permeability Enhancement in Central and Western Japan due to the 2011 Tohoku Earthquake

2.1. Introduction

Earthquakes produce several types of changes in groundwater level: (1) step; (2) transient; and (3) oscillations. These can be classified into more detailed categories. The individual mechanisms of these changes are considered to be multiple, because they can depend on not only epicentral distance and event magnitude, but also on the characteristics of the observation site. Even if an observed change in groundwater level is just a "decrease", the main factors for producing the change can vary with distance from the epicenter, and it is difficult to distinguish the type of mechanism from only observations of groundwater levels.

Montgomery and Manga (2003) summarized these mechanisms based on previous studies, which can be reclassified into roughly two possible causes: static and dynamic strains (Fig. 2.1). Distance attenuation for the static and dynamic strains are different, especially dynamic strains associated with surface waves propagate a long distance with $1/\sqrt{r}$ (r: distance). Static strains produced by fault slip cause permanent crustal deformations, which results in step changes. Jónsson et al. (2003) reported the changes in groundwater level induced by static strain. The epicenter of the earthquake (Mw 6.5) they studied was located ~10 km from their site. Observed increases and decreases in groundwater

correspond with the four-quadrants of simulated post seismic deformation. Their observations and analytical results are clearly consistent with the typical mechanisms that increase/decrease in groundwater is produced by static compression/tension of the crust.

Static strain changes can also produce transient change in groundwater. However, the physical explanations for the step and transient changes can be different. If cracks are formed at the time of the static strain change, water pressure in the pores would be further lowered, changing the step response. Then, newly formed cracks enhance the permeability of the rock mass, and that effect appears as a subsequent transient change in groundwater. In other words, there are effective changes in permeability and associated fluid diffusion.

Dynamic strain also can produce both step changes and transient changes in groundwater, but these mechanisms are different from the effects of static strain. Generally, dynamic strain is a temporal crustal deformation associated with the passage of seismic waves. The maximum magnitude of dynamic strains is generally larger than that of static strains at distances larger than a few times fault dimensions. It may be possible that cracks are opened in response to the compression and extension of crust caused by seismic waves. Brodsky et al. (2003) proposed that dynamic strain introduces and/or promotes water flow in the rock mass, and activated water removes the blockages in cracks. This mechanism has been demonstrated in laboratory experiments (Elkhoury et al., 2011; Candela et al., 2014). Kitagawa et al. (2006) investigated the groundwater changes associated with the 2004 Sumatra

earthquake (Mw 9.1), and reported that groundwater changes of a few centimeter were observed in 38 of 45 stations and 52 of 62 wells, in Japan. Although the epicentral distance is more than 5000 km, the maximum amplitude of 10^{-6} in areal strain caused by seismic waves and a static change in areal strain of 10^{-7} were observed at the observation sites. The sampling interval of 0.05 second enabled observations of the multiple Rayleigh waves that traveled several times around the Earth, and produced the oscillations of observed pressure with each passage. This special feature of Rayleigh waves is also a potential factor in groundwater changes. There are other reports that the timing of changes in groundwater level correspond to the passage of Rayleigh waves (e.g., Brodsky et al., 2003; Doan and Cornet, 2007). Kitagawa et al. (2006) proposed that the possibility of changes in fluid diffusion is associated with unclogging of barriers in the cracks.

In terms of changes in permeability, Elkhoury et al. (2006) examined the tidal responses of well water levels and suggested increases in permeability produced by seismic waves or dynamic stress. Xue et al. (2013) also used the tidal response of water levels in a deep borehole to track permeability for a period of 18 months in the damage zone of the 2008 Wenchuan earthquake (M7.9), and noted a sudden permeability increases due to the regional earthquakes.

We examined the tidal response of pore pressure (water level) and volumetric strain observed in central and western Japan associated with the 2011 Tohoku earthquake (Mw 9.0), which occurred off the east coast of Honshu, Japan at a distances of 500-1000 km. Our results suggest the permeability

enhancement of the rock mass associated with the earthquake.

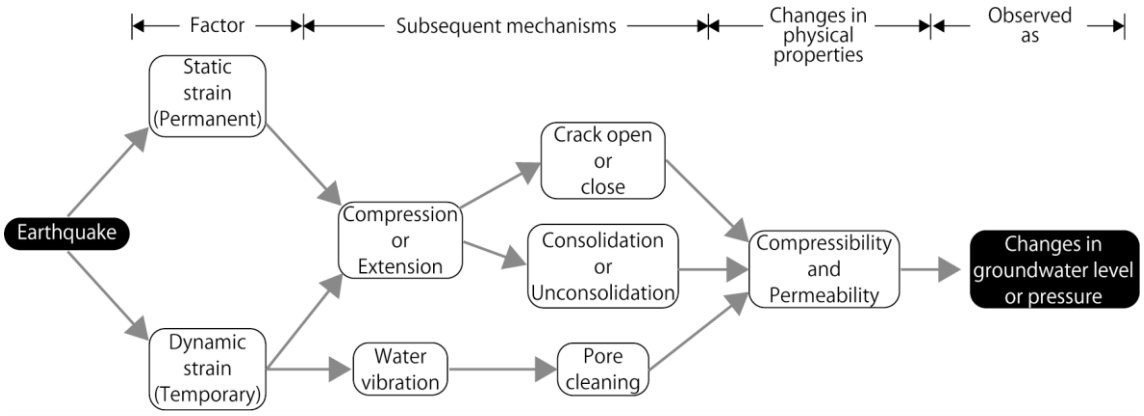

Figure 2.1. Schematic diagram showing processes of hydrological perturbations from earthquake occurrence that produce observed groundwater anomalies.

2.2. Observation Sites and Data

2.2.1. Site Kamioka

The Disaster Prevention Research Institution (DPRI), Kyoto University has been monitoring pore pressure in the boreholes and associated barometric pressure and strain continuously, since 2005 at the Kamioka mine in Gifu prefecture, central Japan (Fig. 2.2). The latitude and longitude of observation site are 36.43°N and 137.29°E, respectively. The Atotsugawa fault system is located in this region and consists of the Atotsugwa, Mozumi-Sukenobu, Midagahara, Ushikubi and Mannami-Touge faults, having a total length of 70 km near the Kamioka mine. In particular, the Atotsugawa fault was ruptured

during the 1858 Ansei Hietsu earthquake (M 7.3 - 7.6), and smaller events often occur along this fault system (Wada and Ito, 1995). Our boreholes cross some small faults that are not seismically active but may act as pathways for water flow (Fig. 2.3). The mine is located in Ikenoyama and had been used for mining, but is now being developed as a scientific research and observation facility such as for the Super-Kamiokande and Large-scale Cryogenic Gravitational wave Telescope (termed KAGURA). The typical rock mass is gneiss, which contains Zn, Pb, Cu, and Ag (Table 2.1). The elevation at the entrance of the mine is 360 m. We selected two boreholes from the existing holes that had been drilled for mining. The two boreholes are located about 6 m apart and extend horizontally with lengths of 350 m west-southwestward (No.1), and 90 m northwestward (No.2). The water table lies above the tunnel and thus water is discharged out of the boreholes. The well heads are sealed by packers and pressure transducers were installed. For shallower boreholes with depths less than 50 m, changes in pressure occurring as pulses caused by rain are often observed, but such features do not appear in our data (Fig. 2.4). However, the Kamioka region has heavy snow in the winter season, thus melted snow percolates into the subsurface, and appears as a seasonal trends in the pressure records (Fig. 2.4). There is a time lag between peaks in the pressure and snowfall records, that can be explained by the time required for melt of snow and percolation to occur. This time lag also indicates that the seasonal changes are produced by the melting snow, and not by the weight of the snow. In addition to pore pressure, barometric pressure and three component strains are being observed continuously.

The inside of the boreholes is not cased, so measurements are sensitive to the existence of cracks and faults. The installed pressure transducers were quartz response pressure gauges, which record changes in pore pressure as changes in the resonant frequency. Pore pressure data are transmitted via a RS232C port and recorded on a hard drive. The sampling interval is 1 second and absolute values of the pore pressure are approximately 500 and 200 kPa for the No. 1 and No. 2 boreholes, respectively. The different pore pressures suggest that they monitor different aquifers, or a part of borehole No. 2 is exposure to outside pressure.

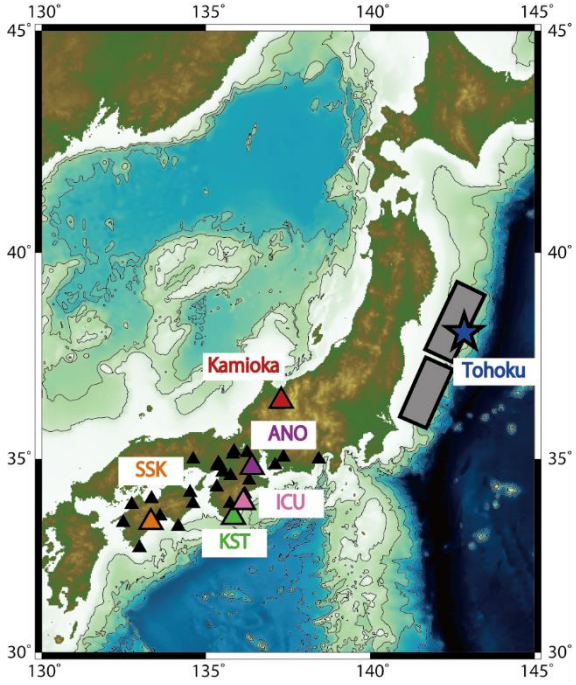

Figure 2.2. Map showing location of groundwater observation sites in Japan used in this study. The red triangle is DPRI, Kyoto Univ. observation site. Black, green, orange, pink, and purple triangles show the National Institute of Advanced Industrial Science and Technology (AIST) well sites. Gray rectangles and blue star indicate the slip area and epicenter of the 2011 Tohoku earthquake, respectively.

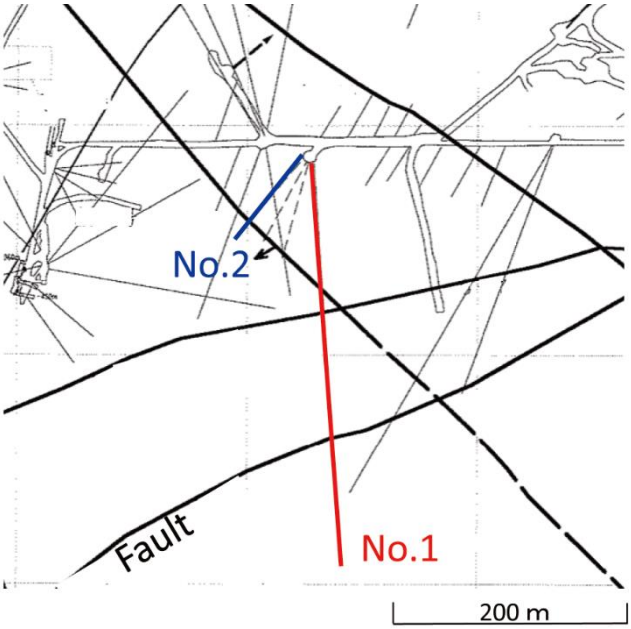

Figure 2.3. Location of boreholes in the Kamioka mine. Red and blue lines indicate the boreholes of No. 1 and No. 2, respectively (reported by Kamioka Mining and Smelting Co., Ltd.).

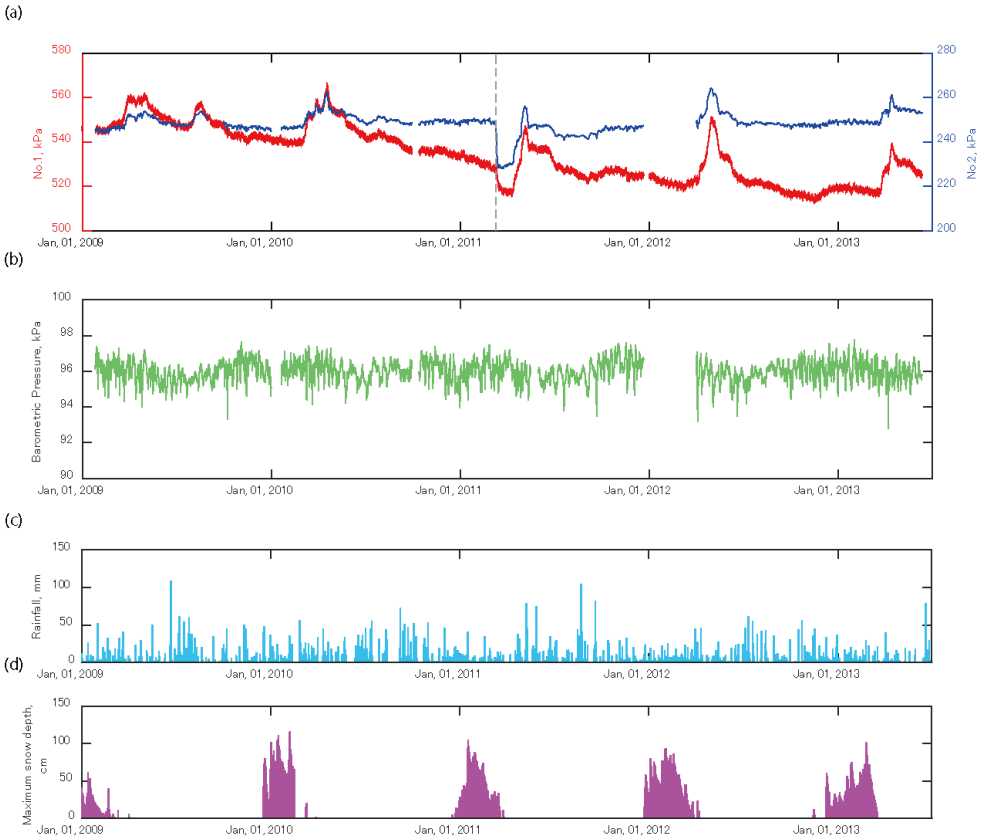

Figure 2.4. Time series of observed data at the Site Kamioka from 2009 to 2013. (a) Pore pressure; red and blue lines show pressure records of Holes No. 1 and No. 2, respectively, and gray dashed line is the time of the 2011 Tohoku earthquake. (b) Barometric pressure monitored at the observation site. The original sampling interval of the pressure and barometric pressure is 1 s, and both (a) and (b) were resampled with 1 hour intervals. (c) and (d) are the daily rainfall and maximum snow depth, respectively, recorded by JMA (JMA site Kamioka is located 13 km south of our observation site).

Table 2.1. Geological information of Site Kamioka.

Site	Kamioka	
The elevation, m	360	
Structural geology	Gneiss	
Bore bole length, m	No.1	No.2
	350	90

2.2.2. AIST observation sites

At other sites for groundwater monitoring, large changes in pressure or water level induced by the Tohoku event were also observed. Kitagawa and Koizumi (2011) reported the groundwater changes observed at the sites in Japan managed by the National Institute of Advanced Industrial Science and Technology (AIST), which were recorded at 52 observation sites and 87 wells. The sampling interval of water level is 1 or 20 Hz with 0.1 mm resolution (Matsumoto and Koizumi, 2013). The maximum change in groundwater was an approximately 926 mm (9.1 kPa) decrease in one day, which was observed 530 km from the epicenter. Increases in groundwater levels and no changes were also observed at some boreholes. These responses do not necessarily depend on epicentral distance and even boreholes located at the same observation site show different responses. Several different types of changes in pressure and water level observed at the same site may be produced by the difference in observed aquifers and physical properties of rock mass at each borehole. Installation construction

techniques and the high resolution of instruments (Matsumoto and Koizumi, 2013) enable detection of these differences.

Niwa et al. (2012) also reported a 15 m increase in groundwater level associated with the Tohoku event, which was observed in Gifu Prefecture central Japan located 500 km away from the epicenter. They suggest that there are effects of nearby fault system such as Tsukiyoshi fault with a 10 km length. At this location small local event can show clear changes in the groundwater records, and this sensitivity of the borehole showed large changes in groundwater at the time of the Tohoku event. The effect of the local site response of the hydrologic system to earthquakes is further discussed in Chapter 3.

Kitagawa and Koizumi (2011) only reported the magnitude of increase or decrease in groundwater level, and the theoretical volumetric strains calculated based on a rectangular fault model. For comparison with our results from Site Kamioka, we selected 4 AIST groundwater observation sites based on the completeness of the data. Sites Anou (ANO), Ichiura (ICU), Kushimoto-Tsuga (KST), Suzaki (SSK) with 11 boreholes in total were selected. The same data processing as used at Site Kamioka was applied for the data. The representative geologies of sites and location and screen depth of each borehole are listed in Tables 2.2 and 2.3. All 11 boreholes responded to the 2011 Tohoku earthquake, and some of them recorded step changes in groundwater levels. We estimated the change in groundwater level by comparing a 5 minute average before and after the earthquake.

In addition to the groundwater level, AIST observation sites are instrumented by strainmeters having < 0.2 nanostrain resolution (Matsumoto and Koizumi, 2013) and, consist of 4 horizontal components differing in direction by 45 degree and a vertical component. Strain data enable evaluation of the stability of the rock stiffness. Here volumetric strains were calculated using 2 orthogonal out of the 4 horizontal components and the vertical component.

Table 2.2. Geological information of AIST observation sites.

Site	Structural geology
ANO	Granite, gabbro, quartz-diorite of Ryoke metamorphic belt Sand stone, silt stone, tuffaceous sandstone and siltstone (Yoshida et al., 1995)
ICU	Granite porphyry and acid tuff
KST	Sandstone, mudstone and alternation of sandstone and mudstone (Geothermal Engineering Co., Ltd, 2008).
SSK	Shale, sand stone and alternation of sandstone and shale of the Northern Belt of the Shimanto Terran

2.3. Methods

2.3.1. Tidal Analysis of pressure/groundwater level

To estimate changes in physical properties of the aquifer associated with seismic events, we utilize

the pressure perturbations caused by the Earth tides, because changes in pressure associated with crustal deformation induced by the Earth tides are very robust and predictable. Generally, pressure response of Earth tide has a periodicity, which can be modeled based on the relative position of astronomical bodies. However, this model does not consider the changes in physical properties of the rock mass, therefore the difference between observed and theoretical tidal pressure response can be considered to be due to the changes in physical properties, such as compressibility, permeability, and storage coefficient. To extract changes in pressure caused by the Earth tides, we used the tidal analysis program BAYTAP-G (Tamura et al., 1991), which can decompose observed pressure data into four components; (1) background noise; (2) trend: slow, long-term seasonal, or interannual variations; (3) barometric response: variations in pore pressure induced by barometric pressure that monitored continuously with pressure data; and (4) Earth tides response. BAYTAP-G requires the information of site location, observed pore pressure (groundwater level) and barometric pressure which were resampled from 1s to 1 h. The hyperparameter controls the smoothing of the trend which is selected based on ABIC (Akaike Bayesian Information Criteria; Akaike 1980; Tamura et al., 1991). For the component of (4) Earth tide response, we can obtain the amplitude and phase lag of observed pressure relative to the theoretical pressure (strain) associated with the tidal loading. The semi-diurnal (e.g., M_2:12.42 h) and diurnal (e.g., O_1: 25.82 h) components are often used in this type of analysis, because their amplitudes are larger than other components. In this study, we use an analysis time window

determined by trial and error to obtain the most representative amplitude and phase lag of the tidal signal. Wider time windows are more compatible with the filtering and reduce the error of estimation, whereas shorter time windows enable clearer determination of the timing of the amplitude and phase anomalies, but can be sensitive to outliers that produce errors. We tried various time windows from 15 days to 6 months and chose a 3 month time window, considering the accuracy and time resolution seen in the data. It is possible that a 3 month time window is too large to detect small changes in tidal response produced by earthquakes, but is appropriate to detect the clear change produced by large earthquakes. We should also keep in mind that long time windows might include the effects of aftershocks which cannot be distinguished in this time window. To help reduce the effects of aftershocks and other geological phenomena occurred that may occur within in a 3 month time window, we shifted this time window by intervals of one day and obtained the amplitude and phase lag of pressure (groundwater level) tidal response.

2.3.2. Model for Estimation of Hydraulic Diffusivity

Anomalies in tidal response of water pressure reflect changes in physical properties of the aquifer. Roeloffs (1996) suggests a model for the estimation of vertical hydraulic diffusivity, which utilizes the characteristic of frequency dependence of aquifer compressibility. In general, an aquifer transitions its behavior from undrained to drained conditions in low-frequency bands such as tidal loading:

$$\frac{\Delta p(z)}{\Delta \varepsilon} = -BK_u \left[1 - \exp\left(-[i\omega(z - z_w)^2/c]^{\frac{1}{2}}\right)\right] \quad (2.1)$$

where $\Delta p(z)$ and $\Delta \varepsilon$ are the tidal response of pressure and strain, B is the Skempton's coefficient, K_u is the bulk modulus at an undrained condition, ω is frequency of the Earth tide, $z - z_w$ is the depth from water table to the observation point, and c is the hydraulic diffusivity. Here extension of the crust is positive. This equation is derived from the linear pore elastic theory with the diffusion equation. There are two boundary conditions: (1) $p(z_w) = 0$, which indicates that pore pressure in the rock mass (p) is zero at the water table; and (2) $p(\infty) = -BK_u \epsilon_0 exp(i\omega t)$, which indicates that pore pressure in the rock mass at the deep underground depends on BK_u. Eq. (2.1) has complex components with real and imaginary parts representing amplitude and phase lag in the pore pressure relative to the strain, respectively. Fig. 2.5 shows the trend of amplitude with frequency, and the hydraulic diffusivity (c) can be estimated from $\Delta p/\Delta \varepsilon$ in the frequency range of Earth tides (~ 2 cycles/day). In contrast, $\Delta p/\Delta \varepsilon$ approaches values of BK_u at high frequency (~ 1 Hz) which represents that pressure propagates without fluid diffusion. BK_u can be estimated from observation of $\Delta p/\Delta \varepsilon$.

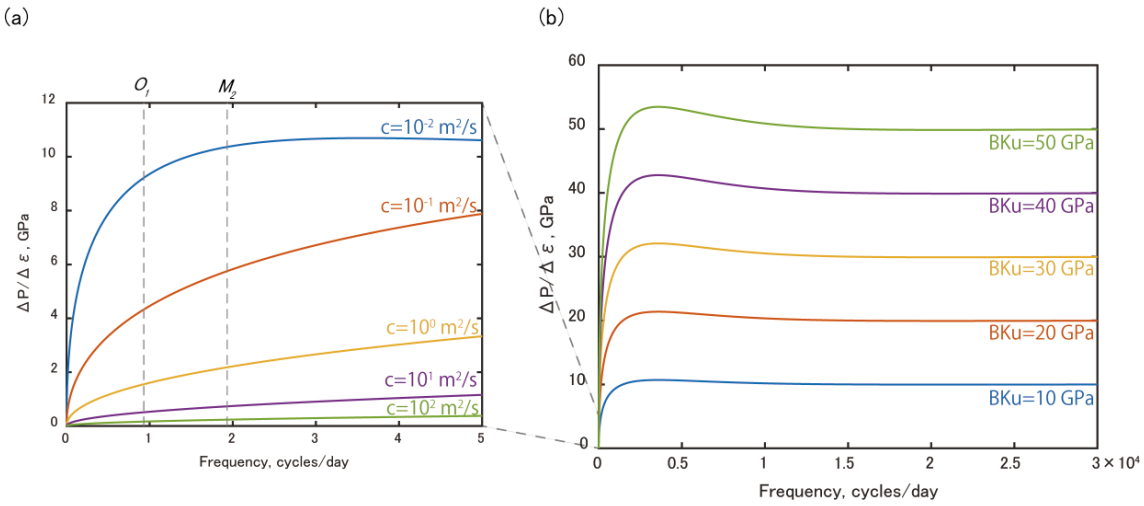

Figure 2.5. The amplitude of pressure relative to the strain as a function of frequency. (a) The ratio of changes in pressure to strain in the low frequency range, assuming $BK_u = 10$ GPa and c=10 m^2/s in Eq. (2.1), respectively. (b) Convergence of the ratio of changes in pressure to strain, in the high frequency range, with several values of BK_u and c= 10 m^2/s.

2.4. Results

2.4.1. Results of Site Kamioka

2.4.1.1. Decrease in Pore Pressure

Both step-like and subsequent transient changes in pressure associated with the Tohoku earthquake were observed at our observation site (Fig 2.6). The steps may reflect the deformation of pore space, which pressure changes are transmitted instantaneously (Roeloffs, 1996). Strains also have been observed with three horizontal components and one vertical component at Site Kamioka. The coseismic change in volumetric strain observed at Site Kamioka was 5.0×10^{-7} (extension is positive) at the time of the Tohoku earthquake, which could produce the changes in pore pressure of -5.3 and -8.9 kPa for boreholes No. 1 and No. 2, respectively. This can be quantitatively explained by

a relationship between pressure and strain under undrained condition ($\Delta p = -BK_u\Delta\varepsilon$).

The gradual changes in pressure are attributed to fluid diffusion, which depend on the changes in physical properties of the rock mass. Decreases in pore pressure were 2.1 kPa, and 12.9 kPa in a day for boreholes No. 1 and No. 2, respectively. The maximum decrease in pressure of 11.2 kPa and 19.5 kPa were eventually recorded, which took almost one month (Fig. 2.6(a)). These are the largest changes of our data ever recorded. Generally, pressures in March-April tend to increase due to the percolation of melted snow and the apparent recovery of pressures in March – April, 2011 could include these effects (Fig. 2.4).

Water pressure is also affected by changes in physical properties of the rock mass, and if the permeability of the rock mass is changed by earthquakes, it could be observed at boreholes as groundwater anomalies. Changes in physical properties appear in the tidal response of pressure and we describe them in the following at the section.

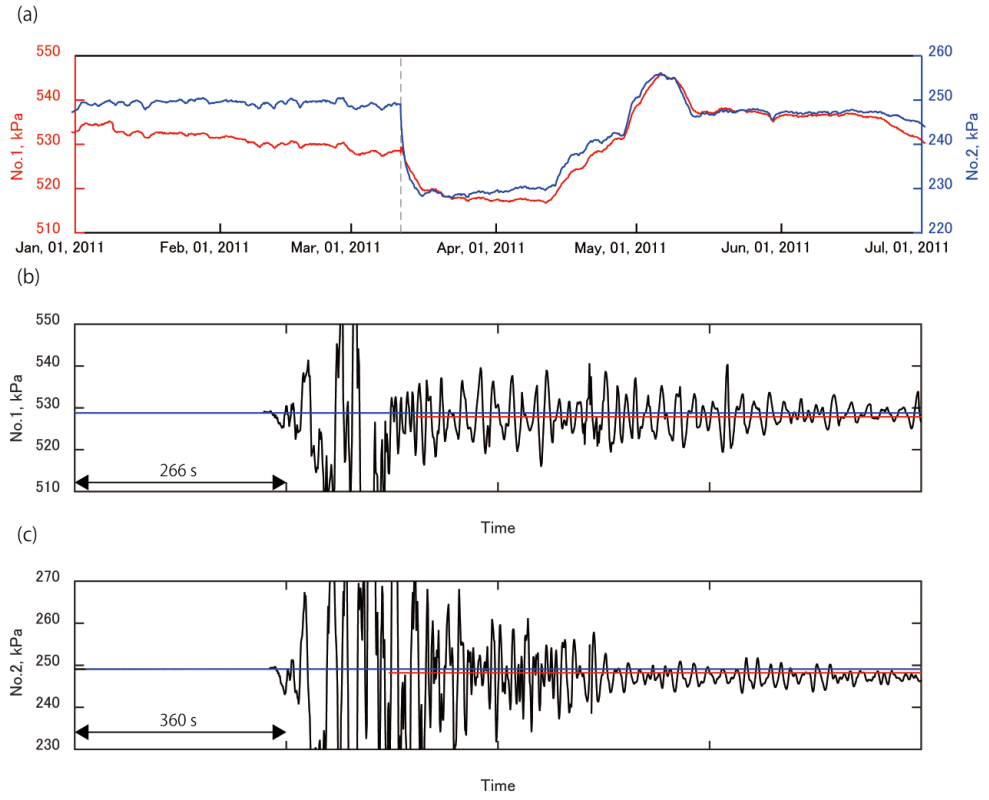

Figure 2.6. Coseismic and postseismic changes in pore pressures. (a) Magnified figure of Fig. 2.4(a), and coseismic responses of (b) No.1 and (c) No.2. Gray dashed line in (a) is the occurrence time of the 2011 Tohoku earthquake. The clock of the pressure logger was off at the time of the Tohoku event and blue and red lines in (b) and (c) represent average pressure values before and after the earthquake, respectively.

2.4.1.2. Tidal Responses of Pore Pressure

Previous studies reported that the pressure response to the M_2 component is clearer than that of the O_1 component (Elkhoury et al., 2006; Xue et al., 2013). We show the results of borehole No.2 for the estimated amplitude and phase delay of the M_2 component. The estimation errors that includes the time of the Tohoku event are larger than for other periods, which were derived by the pressure offset and seismic waves with large amplitude. These time periods should be ignored, when we compare

amplitude and phase delay of tidal response before and after the earthquake. The results show a clear decrease in amplitude of the M_2 component after the Tohoku earthquake (Fig. 2.7(a)) but there is not an understandable change in the phase (Fig. 2.7(b)). The cause for the ambiguous changes in phase are not well explained, therefore we focus only on the tidal amplitudes, and future work must done to investigate the effect of permeability on the phase changes. We obtained similar results for borehole No.1, although the appearance is less clear than borehole No.2 (Kinoshita et al., 2015; Supporting Information).

We have monitored strains, but their data is intermittent and cannot be used for long period analysis. Thus, we calculated the theoretical strain response to the Earth tides using the GOTIC2 program incorporating the Earth and ocean tides model (Matsumoto et al., 2001). Although the time series of tidal responses of strain cannot be extracted from only the observed strain records, short time periods of strain are available during earthquakes which enables us to estimate BK_u in Eq. (2.1) from the ratio between the peak to peak values of observed pressure and strain during the passage of the seismic waves. Then, we assumed that the obtained BK_u of 10.6 and 17.7 GPa for boreholesNo.1 and No.2, respectively, are constant with time. The boreholes at Site Kamioka extend horizontally, so we assumed that observed pressures correspond with water heads ($p = \rho g h;\ \rho = 10^3$ kg/m^3, g=9.8 m^2/s) and substituted the average pressure in a 3 month time window for $z - z_w$. The contribution of fluctuations in $z - z_w$ for estimation of hydraulic diffusivity is smaller than that of Δp in Eq. (2.1),

thus we ignore the excess pressure possibly produced by borehole sealing. Although the estimated hydraulic diffusivity may differ by changing some of these assumptions, the relative change in hydraulic diffusivity before and after the earthquake can be used for discussion. The time series of hydraulic diffusivity was calculated for intervals of one day. The apparent variations of hydraulic diffusivity estimated from the M_2 component amplitude is opposite to that of the M_2 component amplitude, because we assumed a constant BK_u in Eq. (2.1), which is a proportionality factor.

The amount of changes in hydraulic diffusivity of borehole No.2 at the time of the Tohoku earthquake is larger than No.1, with a change of 3.3 m^2/s to 6.7 m^2/s. At the same time, the change in hydraulic diffusivity of No.1 was from 3.3 to 3.8 m^2/s.

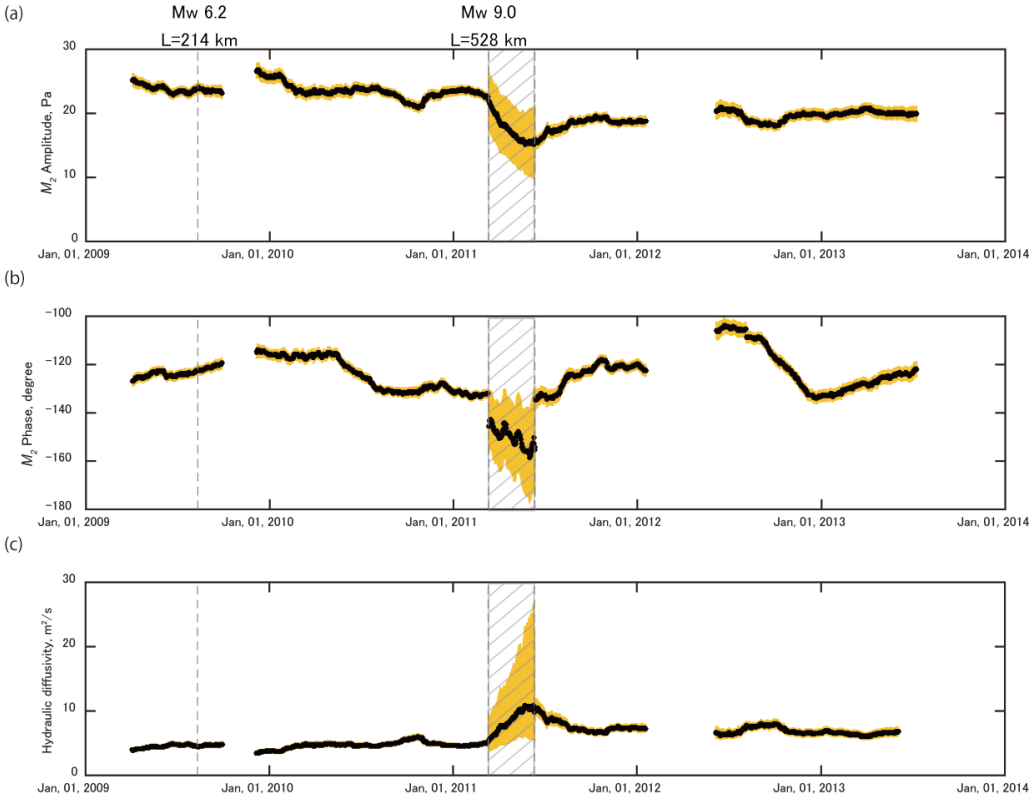

Figure 2.7. Borehole No.2 results of pressure responses to the semidiurnal tide (M_2 component). Time series of (a) amplitude, (b) phase and (c) hydraulic diffusivity estimated based on (a) amplitude. The yellow bars in panel (a) and (b) indicate the standard deviation of each plots (2σ). Yellow bars in panel (c) represents the acceptable range of hydraulic diffusivity considering standard deviation of panel (a). The gray dashed line shows the times of the earthquakes, listed in Table 2.4. The width of the diagonal hatching corresponds with the analysis time window, and the relative large errors after the Tohoku event arise from the pressure perturbations of the Tohoku event.

2.4.2. Results of AIST Observation Sites

2.4.2.1. Coseismic Changes in Groundwater Level and Volumetric Strain at AIST sites

The perturbations of groundwater level produced by the 2011 Tohoku earthquake were observed at all 4 chosen observation sites and all 11 boreholes. The clear step changes in groundwater level were observed at Sites ANO, KST and SSK, but not Site ICU. Whereas subsequent transient changes

were observed at all 4 observation sites. A maximum step change in groundwater level of 671 mm was recorded at Hole 2 in Site ANO (Fig. 2.8), which was the largest change this site ever recorded (Fig. 2.8(a)). In addition, the largest step change in volumetric strain of 1.9×10^{-7} was also observed at site ANO (Table 2.3). Unfortunately, the borehole heads at Site ANO were not sealed, and it is difficult to estimate the conversion factor (BK_u in Eq. (2.1)) from the observed strain and pressure data. Generally, changes in pressure in the formation propagate to the borehole as undrained poroelastic deformation of rock mass and fluid diffusion, and the former is dominant at closed boreholes. In contrast, open boreholes requires much fluid movement to produce fluctuation of water table, and pressure loss is generated, which is the so-called well bore storage effect.

Detournary and Cheng (1993) compiled Skempton's coefficient and bulk modulus at an undrained condition for several types of rocks such as sandstone, granite and marble, and suggested that range of BK_u is $5 - 40$ GPa. According to the values of BK_u reported by Detournary and Cheng (1993), the observed change in static volumetric strain at Site ANO might produce changes in groundwater level of 96-776 mm. Note that these amounts of change in water level do not include the effects of fluid diffusion. This rough estimation is also true for other observation sites that the observed changes in groundwater level at the time of the Tohoku earthquake can be explained by coseismic change in volumetric strain, and depends on the value of the conversion factor (as BK_u in Eq. (2.1)). However, the directions of the coseismic changes in groundwater level do not correspond with the

contraction or extension of observed static strain at some boreholes (Table 2.3). For example, the groundwater level of Hole 1 at Site KST increased at the beginning of the passage of seismic waves and reversed to a decrease (Fig. 2.9(b)). In contrast, the volumetric strain at Site KST indicated step increased, but does not have a transient change like the groundwater level. The cause may be due to a type of liquefaction, where shear stress from seismic waves enhances pressure in the rock mass, and that exceed the decrease in pore pressure attributed to the crack opening. Shear stress returns to zero after the passage of seismic waves, and pore pressure decreases beyond original state due to the newly formed cracks.

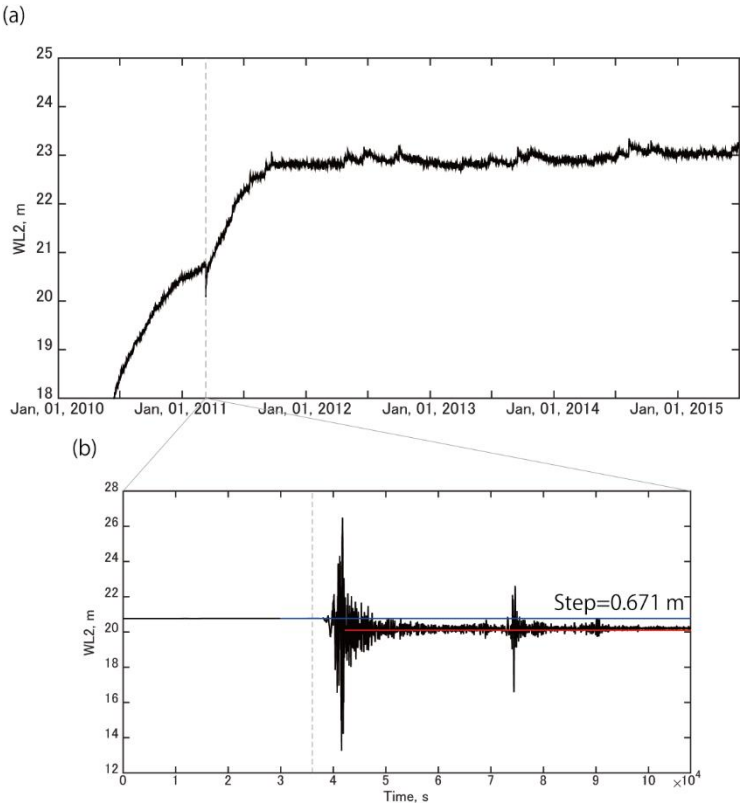

Figure 2.8. Times series of groundwater level of Hole 2 at Site ANO. (a) The period from Jan. 2010 to Jun. 2015. (b) Hydroseismogram of groundwater level for the Tohoku earthquake. The gray dashed lines indicate the occurrence time of the event. Blue and red lines represent a 5 minute average of water level before and after the earthquake, respectively.

2.4.2.2. Tidal Response of AIST Borehole observation sites

Using the same methods described in Section 2.3.1, we analyzed the tidal response change at the AIST sites. In this section we show the results for sites KST and SSK. Other observation holes did not show large changes in tidal response associated with seismic events. The sensitivities of these other boreholes are lower by 1-3 orders compared to the boreholes where tidal changes were detected, which can be seen by the absolute value of amplitude of tidal response in Table 2.3.

Clear change in tidal response of pore pressure associated with the Tohoku earthquake appeared in the data recorded at Site Kamioka as described in Section 2.4.1. To further investigate the effect of this event, we applied the same tidal analysis to the AIST observation sites. Changes in tidal response at the time of the Tohoku event were detected at Holes 1 and 2 at Site KST and Hole 2 at Site SSK. Here we show the results of Hole 1 at Site KST as a typical example of the anomalies of tidal response of groundwater levels, for the M_2 component. We obtained similar results for Hole 2 at Site KST, although the appearance is less clear than Hole 1. The observed groundwater levels of Hole 1 at Site KST showed step increase of 11.5 mm and decrease of 260 mm in half a day (Fig. 2.9(b)). The decreased groundwater level recovered within 4.5 days after the earthquake. Associated clear changes in the tidal response of Hole 1 appeared after the Tohoku earthquake, with an amplitude increase of 14.5 mm in 91 days and a phase advances of 13.8° in 93 days (Fig. 2.9(c), (d)). These changes have appeared to gradually recover, but it have not returned to the original levels within periods of the available data. The time from earthquake occurrence to the maximum values in amplitude and phase advance of the M_2 component are 307 and 188 days, respectively. The gradual changes in tidal responses may correspond to the transition periods of physical properties and the associated migration of groundwater. This could lead to reconstruction of hydrological system. Although the decrease in water level of 0.247 m was eventually recorded at Hole 1 in Site KST after the Tohoku earthquake which is 8 times smaller than that of Site Kamioka ($p = \rho g h;\ \rho = 10^3$ kg/m^3, g=9.8 m^2/s), the

change in amplitude of the M_2 component observed at Site KST is clearer than that of Site Kamioka (Figs 2.7 and 2.9).

Unlike Site Kamioka, Site KST has continuous strain data. Tidal response of strain could reflect the stiffness of the rock mass. Although the changes in tidal responses of groundwater level are very clear at Site KST, the tidal response of static volumetric strain did not show a large change at the time of the Tohoku earthquake (Fig. 2.10). This result suggests that the Tohoku earthquake did not produce any changes in the elastic response of rock mass, but changed the hydrological properties. It is difficult to estimate the conversion factor (BK_u in Eq. (2.1)) at Site KST because the borehole head is opened and absolute value of hydraulic diffusivity cannot be calculated.

Site SSK at an epicentral distance of 1008 km is the farthest sites we studied, where tidal response of groundwater also changed clearly (Fig. 2.11). The tidal response of volumetric strain is relatively stable before and after the Tohoku earthquake, similar to Site KST, which suggests the anomaly in groundwater level was produced by changes in permeability of the rock mass. A long term change in amplitude of strain is seen, and may be due to the unstable installation of strainmeter or transition period of coupling between observatory and rock mass. The strainmeter installation was completed in 2010. Large change in amplitude of volumetric strain did not appear before and after the Tohoku earthquake, which suggests that the long term change in amplitude is not related to the Tohoku earthquake.

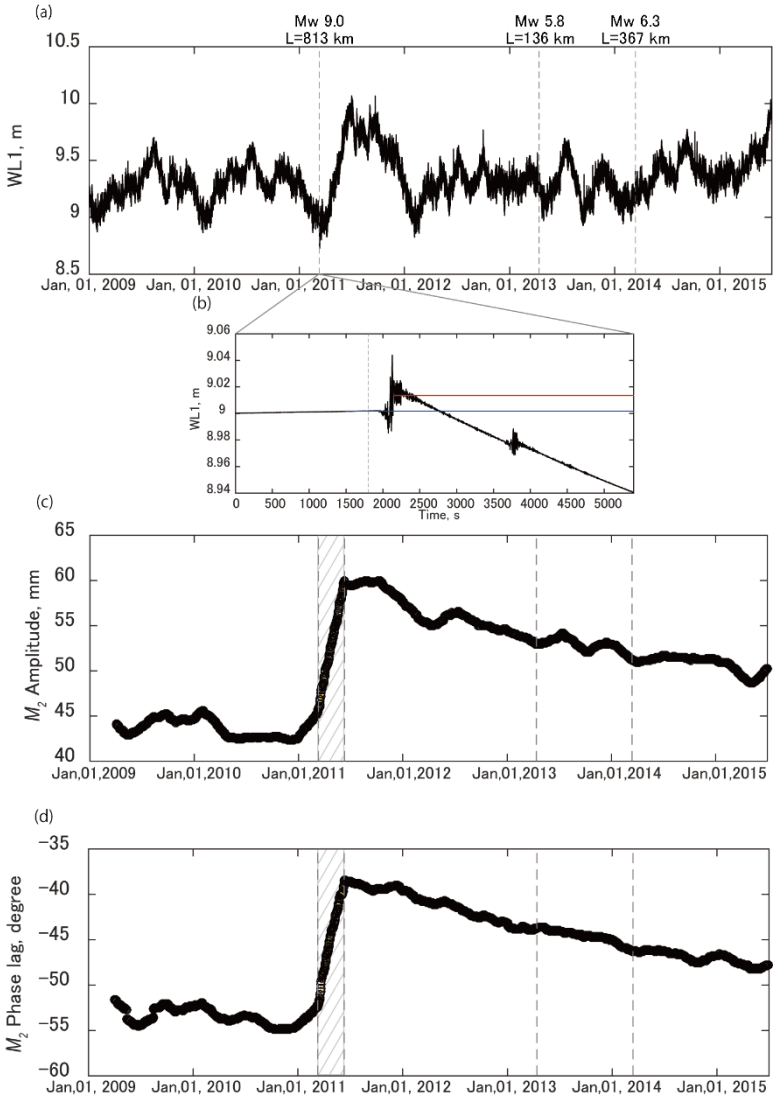

Figure 2.9. Tidal responses of groundwater level observed at Hole 1 of Site KST. (a) Time series of groundwater level, (b) perturbations of groundwater level produced by the Tohoku earthquake. Blue and red lines indicate 5 minute averages of water level before and after the earthquake. (c) amplitude and (d) phase lag of M_2 component. The yellow bars indicate the standard deviation of each plot (2σ), which is very small in this case. The gray dashed lines show the times of earthquakes listed Table 2.4. The width of the diagonal hatching corresponds with the analysis time window.

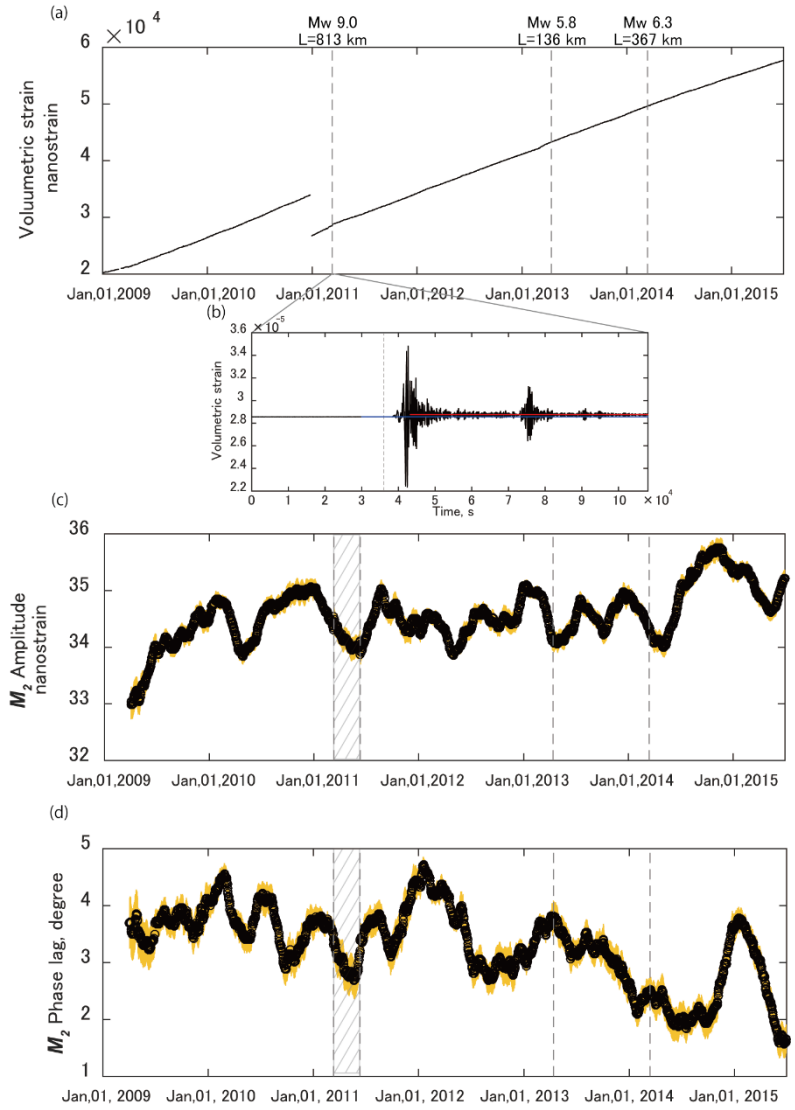

Figure 2.10. Tidal responses of volumetric strain observed at Hole 1 of Site KST. (a) Time series of volumetric strain and (b) perturbations of volumetric strain produced by the Tohoku earthquake. Blue and red lines indicate 5 minute average of volumetric strain before and after the earthquake. (c) Amplitude and (d) phase lag of M_2 component. The yellow bars indicate the standard deviation of each plot (2σ). The gray dashed lines show the times of the earthquakes listed in Table 2.4. The width of the diagonal hatching corresponds with the analysis time window. Strain data is not calibrated and actual amplitudes could be slightly smaller than shown.

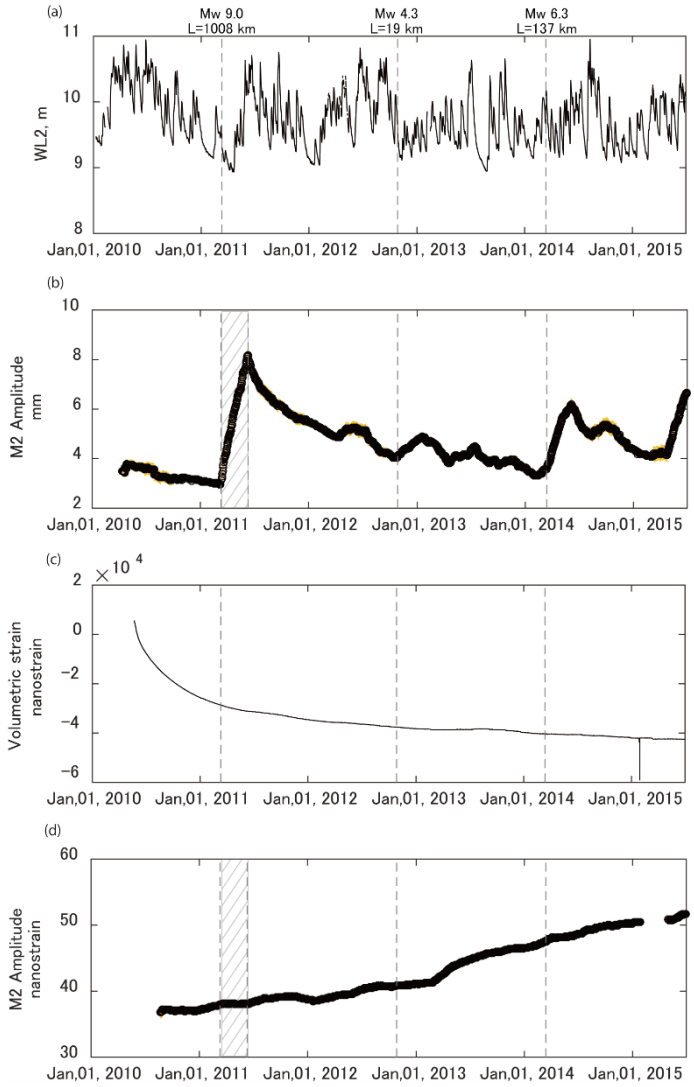

Figure 2.11. Tidal responses of groundwater level observed at Hole 2, Site SSK and volumetric strain observed at Site SSK. Time series of (a) groundwater level, (b) change of the M_2 component amplitude derived from (a), (c) volumetric strain, and (d) changes of the M_2 component amplitude derived from (c). The yellow bars indicate the standard deviation of each plots (2σ), which is very small in this case. The gray dashed lines show the times of the earthquakes listed in Table 2.4. The width of the diagonal hatching corresponds with the analysis time window. Strain data is not calibrated and actual amplitudes could be slightly smaller than shown.

Table 2.3. AIST groundwater observation sites studied in this paper and responses to the 2011 Tohoku earthquake.

Site	Borehole	Lat., °	Lon., °	Casing depth, m	Epicenral distance, km	Coseismic change		Tidal response		
						Groundwater, mm	Volumetric strain	M_2 Amplitude, mm	M_2 Phase, degree	Sensitivity, mm/nanostrain
ANO (Ano)	WL1	34.79	136.40	569.7	686	-353.87	1.9×10^{-7}	0.19 (±0.15)	-3.12 (±1.55)	1.6×10^{-3}
	WL2			240.0		-671.06		-0.12 (±0.10)	1.16 (±0.66)	2.1×10^{-3}
ICU (Ichiura)	WL1	33.90	136.14	580.0	764	-0.39	8.9×10^{-8}	-0.24 (±1.16)	16.10 (±1.46)	2.8×10^{-2}
	WL2			128.6		0.16		2.18 (±0.58)	-1.52 (±9.63)	5.9×10^{-2}
	WL3			30.0		-0.21		0.08 (±0.65)	-11.36 (±80.53)	7.5×10^{-3}
KST (Kushimoto -Tsuga)	WL1	33.52	135.84	580.0	813	11.51	1.9×10^{-7}	14.17 (±0.14)	13.78 (±0.92)	1.6×10^{0}
	WL2			200.9		-16.22		0.49 (±0.20)	2.39 (±1.94)	5.0×10^{-1}
	WL3			42.2		1.36		0.17 (±0.04)	-15.97 (±15.98)	2.0×10^{-3}
SSK (Suzaki)	WL1	33.39	133.32	569.5	1008	-54.14	1.4×10^{-8}	0.10 (±0.26)	0.88 (±1.93)	1.2×10^{0}
	WL2			204.8		-92.16		5.02 (±0.17)	24.27 (±0.82)	9.3×10^{-2}
	WL3			27.5		0.06		0.75 (±0.12)	0.22 (±5.03)	2.4×10^{-2}

The definitions of coseismic changes in groundwater level and volumetric strain are described in the text.

The columns of tidal response indicate the differences between preseismic and postseismic values, and the values in parentheses represent standard deviation (±1σ).

Clear changes in tidal response of groundwater at the time of the Tohoku earthquake were observed at Holes 1 and 2 Site KST, and Hole 2 at Site SSK.

The sensitivities were calculated by the tidal response ratio between pressure and volumetric strain using the data of January, 2013. The average values of one month are shown.

2.5. Discussions and Summary

Changes in groundwater level associated with the Tohoku earthquake were reported from many regions across Japan. In this study, we focused on the tidal responses of groundwater level (pore pressure) and strain data as an indicator of change in physical properties such as permeability of the aquifer. The cause of the permeability change can be related to strain changes, which are classified into dynamic and static strains (Section 2.1).

Both static and dynamic strains produced by the 2011 Tohoku earthquake were the largest ever, recorded by the hydrological monitoring systems, and it is difficult to distinguish which type of strain causes the changes in groundwater levels and associated tidal responses. In particular, the conversion factor of strain into pressure (BK_u in Eq. (2.1)) could not be estimated at most boreholes of studied sites, because the borehole heads are not sealed or the groundwater levels are less sensitive to strain. To understand the mechanism of change in hydrological system produced by seismic events, we also analyzed other earthquakes and found one event (Mw 6.3 on Mar. 14th, 2014) that changed the tidal response of groundwater level at Site SSK (Table 2.4 and Fig. 2.11). The epicentral distance of this earthquake was 137 km, and the size of change in tidal response was smaller than that of the Tohoku event (Fig. 2.11). For other events, they did not produce any changes in tidal response at each site. Although the epicentral distances of the Tohoku earthquake are the farthest among compared earthquakes, the static volumetric strain is larger by 1-2 orders than that of other events because of its

large size (Mw 9.0), and this trend was true of all of observation sites. Whether the observed changes in groundwater level (pore pressure) associated with the Tohoku earthquake could be produced by only static volumetric strain, can be evaluated by the value of the conversion factor (BK_u in Eq. (2.1)). However, the increase in groundwater level observed at Hole 1 in Site KST is inconsistent with the extension of observed static strain. This inconsistency suggests that the effect of dynamic strains is more dominant than static strains. The correspondence of timings between step change in groundwater and the passage of the seismic waves also suggests the large effects of dynamic strains (Figs. 2.9(b) and 2.10(b)). In particular, the change in groundwater level at Hole 2 in Site SSK at the time of the Tohoku event cannot be explained only by static strain, and requires the effects of dynamic strain to produce observed large change in groundwater level.

For the evaluation of dynamic strains, we compared peak to peak amplitudes of volumetric strain during the passage of seismic waves. The largest dynamic strains of the order of 10^{-5} among all the events and sites were observed at Sites Kamioka and KST for the Tohoku earthquake. In contrast, Site SSK at an epicentral distance of more than 1000 km to the Tohoku earthquake, had a peak to peak amplitude of dynamic strain of 5.0×10^{-6}, which was comparable with strains from other earthquakes. In addition, peak ground acceleration (PGA) and peak ground velocity (PGV) were also considered for the evaluation of strong motions at the site (Wang et al., 2006; Elkhoury et al., 2006). AIST observation sites have accelerometers and seismometers, but Site Kamioka did not have this

instrumentation, and the values for PGA and PGV at Site Kamioka were estimated from the records of 14 KiK-net (Kiban-Kyoshin net) three-component borehole strong motion seismographs near Site Kamioka. The records were band-pass filtered between 0.05 and 10 Hz before the estimation of PGA and PGV. The earthquakes that occurred near Sites KST and SSK produced larger values of PGA and PGV compared to the Tohoku earthquake by a factor of ~6 (Table 2.4), but surprisingly did not produce any change in tidal response of groundwater, except for the Mw 6.3 event of Site SSK.

The peak to peak amplitude of strain at the time of the Tohoku earthquake observed at Site KST was 1.3×10^{-5}, which is larger than the strains for the other events. It is likely that the large peak to peak amplitude of strain and small PGA and PGV for the Tohoku event at Site KST reflects the frequency dependence of seismic waves that affect the hydrological system. If permeability change of aquifer is sensitive to low frequency perturbations, the trends observed at Site KST can be explained by considering the dominant frequencies recorded by the strainmeter compared to the dominant frequencies of the ground acceleration and velocities. Brodsky and Prejean (2005) proposed that oscillations of groundwater level responding to seismic waves is proportional to the square root of period. In the case of changes in groundwater level produced by distant earthquakes, the effective frequencies often corresponds with the arrival time of surface waves, which also indicates the frequency dependence of subsurface hydrological systems (e.g., Brodsky et al., 2003). Also, Miyazawa (2011) reported that the attenuation with distance of static and dynamic stress produced by

the Tohoku earthquake showed that dynamic stress is 1~2 orders larger than static stress at 500~1000 km from epicenter.

In these results, we speculated that there is a possibility that hydrological perturbations observed within 500-600 km from the epicenter, are partially produced by static strains. Note that the effects of dynamic strains is also large at this epicentral distance. In contrast, the dynamic strains might be dominant at more than 700-800 km distances.

For the Tohoku earthquake, both static and dynamic strains have potential to produce hydrological perturbations of the aquifer that resulted in large changes in pore pressure (groundwater level) and that of tidal response. We need to investigate other events that produce change in tidal response to better understand the characteristics of these effects. The details of the dynamic strain such as duration, dominant frequency and back azimuth of seismic waves also should be investigated. In particular, the seismic waves of the Tohoku event are characterized by not only large amplitudes but also components of low frequency, which may propagate a long distance. We do not have the data for groundwater level located at distance of more than 1000 km from the Tohoku earthquake, and the tidal response of such observations could be important for understanding the effects of the Tohoku earthquake. Variations in groundwater level with a maximum change of 48 cm, and associated fluctuations in temperature and electrical conductivity were observed in Korea (Lee and Woo, 2012). These observations indicate the possibility that change in permeability may occur at distance 1500 km from the epicenter.

The clear phase differences in tidal response were produced by the Tohoku earthquake at Sites KST and SSK, but not Site Kamioka. This difference needs to be investigated considering other factors, such as gas effect (Matsumoto et al., 2003b; See Chapter 4).

The behavior of groundwater has received attention as a triggering factor for earthquakes, because fluids can directly reduce effective stress on the fault by increasing pore pressure (See Section 1; e.g., Brodsky et al., 2003). If the permeability of an aquifer is changed by a mainshock on a large scale, associated migration of large amount of groundwater may trigger aftershocks. As shown in this and other chapters of this thesis, borehole observation can be used to monitor not only groundwater and pore pressure but also continuous behavior of permeability of the rock mass.

Table 2.4. Estimation static and dynamic strains for earthquakes that had observed/unobserved changes in tidal response of ground water

Site	Event Date	Event Mw	Epicentral distance, km	Static strain (Okada(1992))	Dynamic strain			Tidal response of groundwater level		
					Peak to peak amp.	PGA, cm/s^2	PGV, cm/s	Change or No change	Effect of static strains	Effect of dynamic strains
Kamioka	2009/8/11	6.2	214	1.1×10^{-9}	-	1.29	0.22	No change	-	-
	2011/3/11	9.0	528	3.4×10^{-7}	1.2×10^{-5}	4.11	2.82	Change	likely	likely
KST	2011/3/11	9.0	813	4.2×10^{-9}	1.3×10^{-5}	0.59	0.06	Change	unlikey	likely
	2013/4/13	5.8	136	2.1×10^{-10}	7.7×10^{-7}	3.27	0.29	No change	-	-
	2014/3/14	6.3	367	-6.7×10^{-11}	4.9×10^{-7}	0.74	0.09	No change	-	-
SSK	2011/3/11	9.0	1008	2.6×10^{-8}	5.0×10^{-6}	0.72	0.05	Change	unlikey	likely
	2012/10/27	4.3	19	1.7×10^{-10}	1.4×10^{-6}	4.08	0.15	No change	-	-
	2014/3/14	6.3	137	-2.2×10^{-9}	6.7×10^{-6}	5.08	0.35	Change	unlikey	likely

Static strains were estimated based on the solutions of Okada (1992) and the focal mechanisms reported by F-net (the National Research Institute for Earth Science and Disaster Prevention). We assumed two rectangular faults (Imakiire and Kobayashi, 2011) for the 2011 Tohoku earthquake.

Dynamic strains were estimated from peak to peak amplitude of seismic waves.

Chapter 3. Repeated Hydrological Perturbations and Subsequent Recovery Associated with Earthquakes

3.1. Introduction

Hydrological perturbations in aquifers produced by earthquakes can induce liquefaction, cause eruption of mud volcanoes, reduce of spring flow and change groundwater levels. These phenomena tend to be observed repeatedly at the same site, and some places have suffered from repeated hydrological disasters. The 2010 Darfield (Mw .7.1) and 2011 Christchurch (Mw 6.2) earthquakes occurred near the Canterbury region in Christchurch and caused damage to the hydrological system of subsurface, which induced liquefactions and destroyed the infrastructure (Cox et al., 2012; Rutter et al., 2016). In another example, Itaba et al. (2007) investigated the groundwater levels near a hot spring located in western Japan, and found that the changes associated with earthquakes appeared in a similar manner, represented by an exponential curve. Woodcock and Roeloffs (1996) also reported that the changes in groundwater levels near the city of Grants Pass, Oregon showed a similar appearance regardless of the focal mechanism and distance to the earthquakes. This suggests that there is a dependence on site-specific characteristics for the hydrological changes. Time series of permeability estimated from tidal loading at the Pinon Flat Observatory in Southern California also indicated that coseismic changes in this quantity are always increases and recovered gradually after each event (Elkhoury et al., 2006). These previous studies suggest that each site has preferential hydrological response induced by the earthquakes.

In Chapter 2, I described the changes in pressure and groundwater level, especially tidal responses produced by the earthquakes. The tidal response of Site SSK (Suzaki) managed by the Geological Survey of Japan, AIST was disturbed by not only the 2011 Tohoku earthquake (Distance: 1008 km) but also a Mw 6.3 event (Distance: 137 km). The magnitude of amplitude changes was different for each event, but both earthquakes caused increases and showed similar recovery (Fig. 2.11).

To investigate the details of the repeated hydrological perturbations produced by earthquakes and following recoveries, we focused on changes in groundwater level of Hole 2 at Site KST (Kushimoto-Tsuga) managed by AIST. The groundwater response to earthquakes often looks similar: a transient increase and subsequent decrease for recovery. Gradual changes in water level suggest occurrence of fluid diffusion. We assumed that there is a stable distribution of the state of the hydrological system in the aquifer, especially a stable distribution of water heads. The state may be disturbed by earthquakes which produces unusual fluid flow. There could be an onset point where the anomaly of the water head is first generated and unusual fluid flow starts. We searched for this point (source) in the aquifer using the postseismic groundwater behavior observed at Hole 2 at Site KST. If the sources of change in water head estimated from groundwater changes of a number of earthquakes are located in a particular region, it suggests the existence of a stable source which triggers fluid flow. In addition, to resolve the main contribution of changes in groundwater level associated with earthquakes, we focused on dynamic strains produced by the seismic waves and evaluated this quantity from the data of a nearby

accelerometer, seismometer and strainmeter, especially their maximum amplitudes. These three quantities represent the size of dynamic ground motions, but are distinguished in terms of the dominant frequencies.

3.2. Observation and Data

AIST developed a groundwater observation network in south-western Japan since FY 2006 with 16 sites (Kitagawa et al., 2013). We investigated the sensitivity of some of the boreholes to earthquakes, based on whether the response of groundwater level can be discriminated from general perturbations, and whether these changes have similar appearance. From the preliminary results, we focused on Hole 2 at Site KST (Kushimoto-Tsuga) located in the southern Kii peninsula. The groundwater level of this hole responds well to large earthquakes, with exponential increases immediately after the earthquakes and then a gradual decrease to the original value. Transient changes in groundwater level usually reflect migration of fluids, and we focused on this behavior to understand the hydrological system of the subsurface. A different response of groundwater level was observed at this borehole only at the time of the 2011 Tohoku earthquake. The response at for that earthquake was a step decrease and recovery that took more than 50 days. Step changes in groundwater level are produced instantly and could be caused by a change in the pore volume without fluid diffusion ($\Delta p = -BK_u\Delta\varepsilon$). In this chapter, we focus on the transient change in groundwater

level rather than the step change.

The elevation of Site KST is ~25 m, and this site is composed of three boreholes having different lengths (Table 2.3; Hole 2 is 200 m long). In addition to the water level meter, seismometers, strainmeters, tiltmeter, and other instruments for measurement of external factors including atmospheric pressure, precipitation, temperature and magnetic force are also installed. The sampling interval of the water level and strain are 1 Hz and 20 Hz, respectively. Accelerometers and seismometers are sampled at 200 Hz and 100 Hz, respectively (Matsumoto and Koizumi, 2013).

3.3. Geological Setting

The geological features around Site KST consists of the Shimosato and Shikiya formations, which contain sandstone, mudstone and alternation of sandstone and mudstone (Geothermal Engineering Co., Ltd, 2008). Intrusion of Kumano Acidic Rocks occurred 14 Ma ago significantly affected the geological structures of this area, and some hot springs are considered to have a relationship with this volcanic activity (Yoshimatsu et al., 1999). Intrusion rocks and dikes suggest the existence of water flow and associated cracks still may affect the behavior of groundwater.

When Site KST was constructed, several preliminary surveys including coring, physical logging and in situ experiments were conducted. From the core samples, the width of fracture zone < 11 cm was found in Hole 2, and there are some mineralized veins which are partially open.

3.4. Methods

3.4.1. Studied Earthquakes

To detect the changes in groundwater level produced by as many as possible earthquakes, we first defined the selection criteria for earthquakes. From Site KST (latitude 33.520° and longitude 135.836°), we selected events with epicentral distance < 1000 km and seismic magnitude (Mw) > 5.0. In addition, larger events having Mw > 7.0 within 1500 km distance were also included. Some multiple earthquakes which occurred within in a short time cannot be clearly distinguished, and were removed from our data set. From the above definition, 139 events in total were selected from the F-net Catalog compiled by the National Research Institute for Earth Science and Disaster Prevention between 2009 and 2015 (Fig. 3.1).

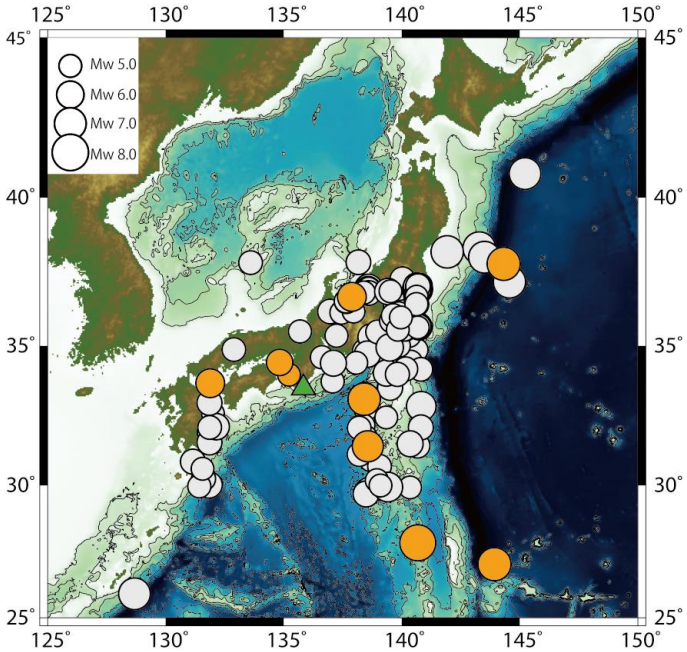

Figure 3.1. The epicenter distribution of earthquakes studied. The green triangle shows the location of Site KST. The circles indicate the epicenters of earthquake studied. The orange and gray circles are

events which produced changes and no change in groundwater level, respectively.

3.4.2. Removal of Tidal Effects in the Observed Groundwater level

We searched the coseismic and preseismic changes in groundwater level associated with the earthquakes from observed data without any correction. Absence of changes in groundwater level are usually distinguishable in the original data because the time period of coseismic change is much shorter than tidal loading. However, for some detectable and questionable changes in groundwater, the effects of earth tides should be removed to estimate the amount of actual changes and recovery periods. In particular, Site KST is located near the cost of the Pacific Ocean, where the amplitudes of the ocean tides are significant. We used the tidal analysis program BAYTAP-G (Tamura et al., 1991) to extract the perturbations of groundwater level produced by the solid earth tides and ocean tides. BAYTAP-G can predict the variations originated from the tides based on observed groundwater level and site location. We resampled original data from 1 s to 1 h and applied BAYTAP-G to the resampled data with a two week analysis time window. The middle of the time window corresponds to the time of the earthquake, which produces groundwater perturbations associated with tides. These theoretical tidal groundwater perturbations were interpolated to 1 Hz sampling interval using a spline curve. By subtracting the interpolated theoretical tidal groundwater perturbations from the original observations, the transient changes produced by the earthquakes become clearer. Then, the amount of maximum

change in groundwater level, the time periods of the change and duration of the recovery can be estimated for each detectable change. Correction for precipitation was not performed, but we confirmed that there was no heavy rains during the periods before and after the detectable changes in groundwater level, as reported by the JMA precipitation catalog.

3.4.3. Fluid Flow Models

3.4.3.1. Model A

Generally, fluids in an aquifer follow Darcy's law and flow from high to lower water heads, which is typical fluid diffusion. Here, increases in groundwater level were observed at the times of the earthquakes, which were produced by increase of water head at the source (Fig. 3.2). From the time series of water level and hydraulic diffusivity of the surrounding rocks, the amount of change in water head at the source and that location can be estimated;

$$H = \Delta A erfc(d/\sqrt{4ct}) \tag{3.1}$$

where H (m) is water level after earthquake at the borehole, ΔA (m) is the change in water head at the source, d (m) is distance from the source to the groundwater observation site and c is hydraulic diffusivity (m^2/s) (Brodsky et al., 2003).

In this model, hydraulic diffusivity is an important parameter that controls the fluids diffusion in the aquifer. We used a hydraulic diffusivity of 5.3×10^{-3} m^2/s in Eq. (3.1), which was estimated from the pumping test performed at Hole 2 (Geothermal Engineering Co., Ltd, 2008), and corresponds with general value of sandstone (Roeloffs, 1996). We assumed that fluid flows in one direction from higher to lower water heads and searched for the values of ΔA and d at 1 m intervals by fitting the model to the observed perturbations of groundwater level. The fit was evaluated by the root mean square (rms) between observed and simulated groundwater levels.

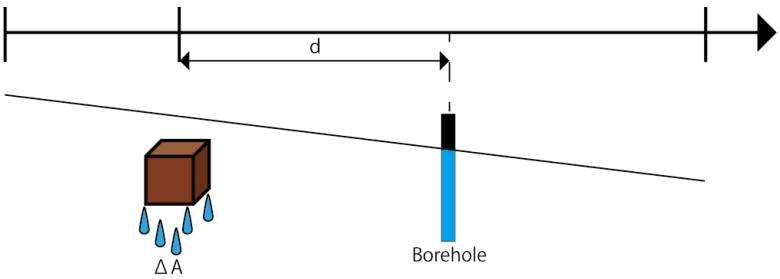

Figure 3.2. Schematic image of fluids flow model (A). Each variable is illustrated in text (Eq. (3.1)).

3.4.3.2. Model B

The Model A assumes that the excess water head does not decrease with time. However, it is natural to expect that the excess water head decreases with time and returns to the original state. Roeloffs (1998) simulated this type of time dependent source, which considers not only the initial

perturbations of groundwater level but also recovery processes. In this case, the fluid model is represented by adding the rate of recharge to the aquifer per unit volume (w) to the 1-D diffusion equation (Wang and Manga, 2010).

$$\frac{\partial h}{\partial t} = c\frac{\partial^2 h}{\partial x^2} + w \tag{3.2}$$

The model based on Wang and Manga (2010) (Model B) is shown schematically in Figure 3.3. There is an aquifer having length L and fluid flows upstream (x $= L'$) and downstream($x = L$). For boundary conditions, we assumed $\frac{\partial h}{\partial x} = 0$ at $x = 0$ which represents no-flow at $x = 0$, and $h = 0$ at $x = L$ (Fig. 3.3). If w is a function of x only, the solution is given by Carslaw and Jaeger (1959);

$$h(x,t) = \frac{4L}{\pi^2 K}\sum_{n=1}^{\infty}\frac{1}{n^2}\left[1 - \exp\left[-\frac{cn^2\pi^2 t}{4L^2}\right]\right] cos\frac{n\pi x}{2L}\int_{-L}^{L} w(x) cos\frac{n\pi x'}{2L}dx' \tag{3.3}$$

where

$$c = \frac{K}{S_s} \tag{3.4}$$

where K is hydraulic conductivity and S_s is specific storage. In this study, the source should be a

function of *x* and *t*, then the solution is given by Eq. (3.5) applying Duhamel's principle (Carslaw and Jaeger, 1959; Wang and Manga, 2010);

$$h(x,t) = \frac{1}{LS_s}\sum_{n=1}^{\infty} cos\frac{n\pi x}{2L}\int_{-L}^{L}\int_{0}^{t} \exp\left[-\frac{cn^2\pi^2(t-\lambda)}{4L^2}\right] w(x,\lambda)\, cos\frac{n\pi x'}{2L}\, d\lambda dx' \tag{3.5}$$

$w(x,t)$ is the coseismic change of water head per unit time which should have some value at *t*=0 but should be zero for other times, because the coseismic release of water at the source is considered to be instantaneous:

$$w(x,t) = w_o(x)\delta(t=0) \tag{3.6}$$

where $w_o(x)$ is the amount of recharge of water per unit volume and $\delta(\mathrm{t}=0)$ is a delta function. Total recharge $H_o(x)$ is given by;

$$H_o(x) = \int_0^t w_o(x)\delta(t)dt \tag{3.7}$$

where $H_o(x) = H_o$ at $\mathrm{x} \leq L'$ and $H_o(x) = 0$ at $\mathrm{x} \geq L'$ (Wang and Manga, 2010; Fig. 3.3). Then, Eq. (3.5) can be represented as;

$$h(x,t) = \frac{4H_o}{\pi S_s}\sum_{n=1}^{\infty}\frac{1}{n}sin\frac{n\pi L'}{2L}cos\frac{n\pi x}{2L}exp\left[-n^2\frac{\pi^2 ct}{4L^2}\right] \quad (3.8)$$

Eq. (3.8) can be rewritten as (Wang and Manga, 2010);

$$h(x,t) = \frac{4\,w_o}{\pi}\sum_{n=1}^{\infty}\frac{1}{n}sin\frac{n\pi L'}{2L}cos\frac{n\pi x}{2L}exp\left[\frac{n^2\pi^2 ct}{4L^2}\right] \quad (3.9)$$

We first estimated $A = \frac{L'}{L}$, $B = \frac{x}{L}$, $D = \frac{c}{L^2}$ and w_o in Eq. (3.9), and then determined x, L and L'.

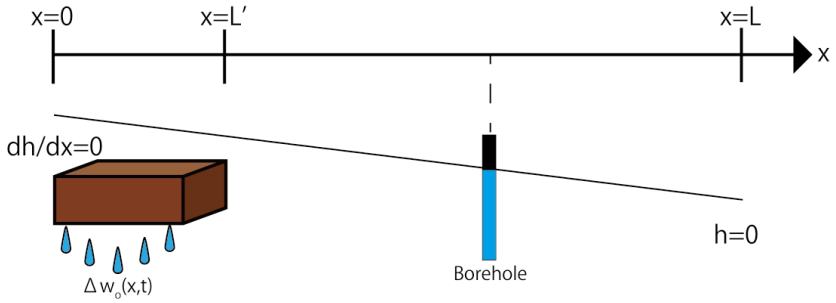

Figure 3.3. Schematic image of fluids flow model (B). Variables and boundary conditions mentioned in the text are illustrated.

3.4.4. Ground Motions Associated with the Earthquakes at Site KST

Considering the epicentral distances of the earthquakes, the contribution of dynamic strains associated with seismic waves are generally larger than static strains. AIST observation sites have accelerometers, seismometers and strainmeters, which can be used for evaluation of the details of dynamic effects of earthquakes. Using a band-pass filter of 0.05 to 10 Hz, we calculated the peak ground acceleration (PGA), peak ground velocity (PGV) and peak to peak amplitudes of volumetric strain for each earthquake.

3.5. Results

Among the 139 earthquakes, 9 events had detectable changes in groundwater (Figs. 3.1 and 3.4). The signals showed increases immediately after the earthquakes, which took more than 1 hour to reach the maximum changes of 138-297 mm and the longest period for the increase was 2.5 days (Table 3.1). There is roughly a positive relationship between the maximum changes in groundwater level and the times required for the changes. Increased groundwater later reversed to decreases returning the preseismic value, which took a longer time than that of the increase.

For the results of Model A, although the hydraulic diffusivity of 5.3×10^{-3} m^2/s estimated from the pumping test independently constrains the distance of fluid diffusion, simulated transient changes in groundwater level based on Eq. (3.1) correspond well with observed data (Fig. 3.5). The magnitude

of estimated ΔA depends on the maximum change in water level observed at the borehole, and the range of d is relatively close to the observation site (3-20 m).

The results of Model B also correspond well with observed transient changes (Fig. 3.6). However, the misfit between observed and modeled groundwater levels for the increasing part are larger than that of Model A due to fitting of the recovery part. Although the range of flow distance in the aquifer (L) estimated is 50-1000 m, the width of source (L') of ~80 m and distance from source to borehole (x) of ~35 m have relatively smaller variations than that of L. These results suggest the existence of a conventional source where abnormal fluid flow produced by earthquakes starts.

The modeled groundwater level changes fit well to the observations. Both Models A and B suggest that the groundwater level of Hole 2 at Site KST is affected by nearby the hydrological system. Note that the hydraulic diffusivity, estimated independently, also controls the location of the source for recharge. The solutions depend on the time period used for fitting the data, and using longer time periods, or changing onset time of diffusion may yield somewhat different solutions.

The borehole at Site KST is located on the slope from hills to hollow and the distance between top of the hill and borehole is ~50 m. From the results of Models A and B which give a distance between the borehole and source of ~35 m, the source may exist near the top of the hill (Fig. 3.7).

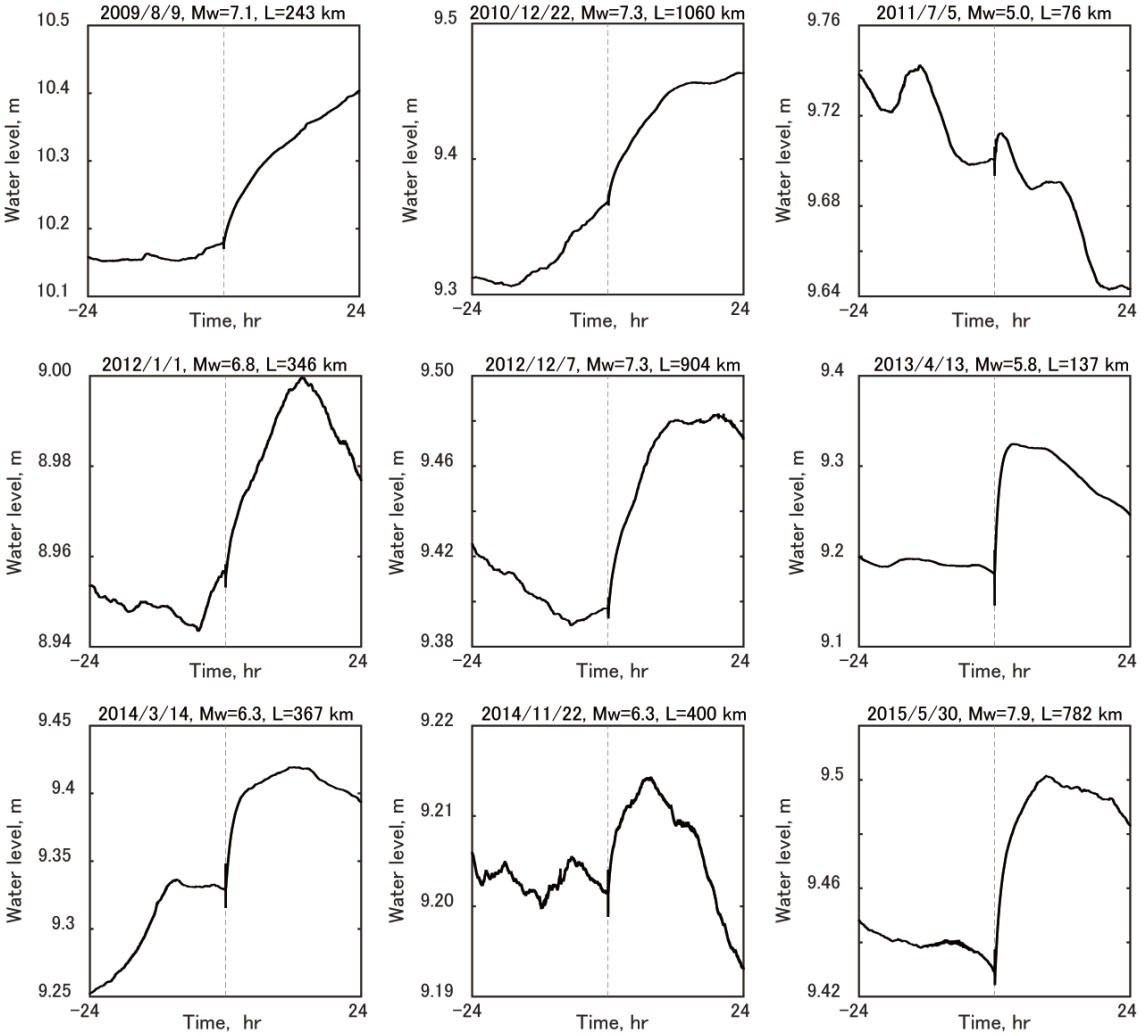

Figure 3.4. Changes in groundwater level produced by nine earthquakes. The dashed line indicates the origin time of each earthquake. The details of each event are shown in Table 3.1.

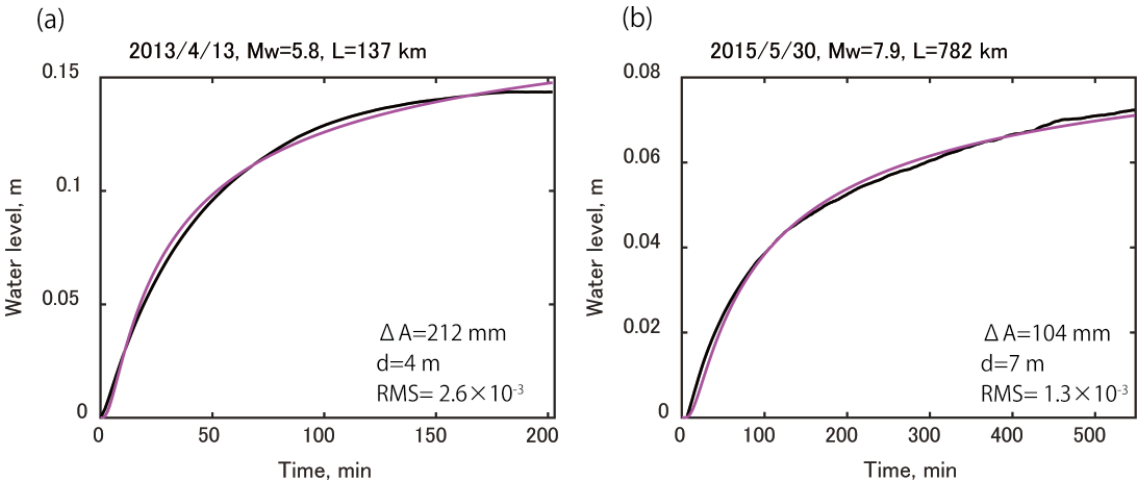

Figure 3.5. Examples of simulated groundwater level for Model A with observations. Response of groundwater level to a nearby earthquake that occurred on Apr. 13, 2013 (a), and a deep intermediate distance earthquake that occurred on May. 30, 2015 (b). Black and magenta lines indicate observed and simulated groundwater level, respectively.

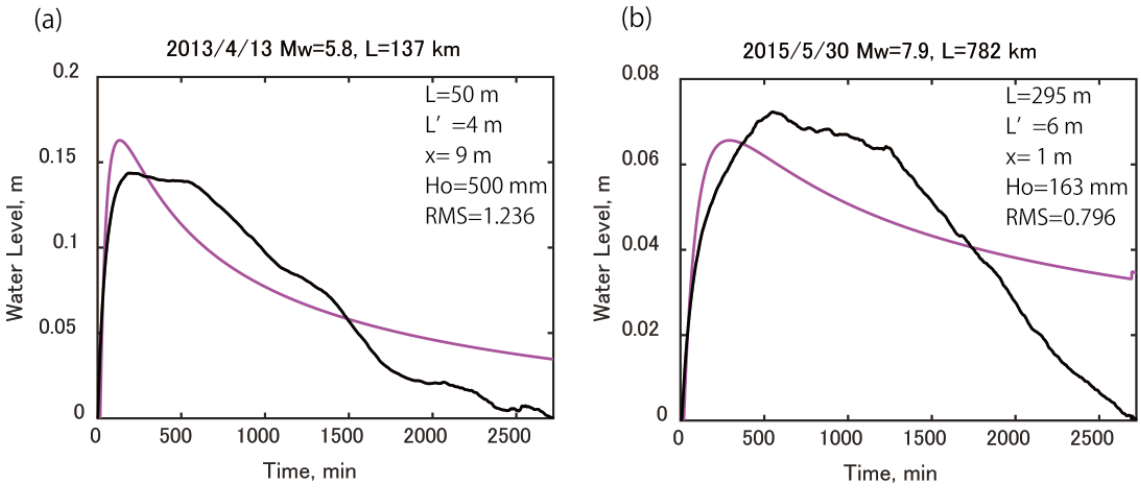

Figure 3.6. Examples of simulated groundwater level for Model B with observations. Response of groundwater level to a nearby earthquake that occurred on Apr. 13, 2013 (a), and a deep intermediate distance earthquake that occurred on May. 30, 2015 (b). Black and magenta lines indicate observed and simulated groundwater levels, respectively.

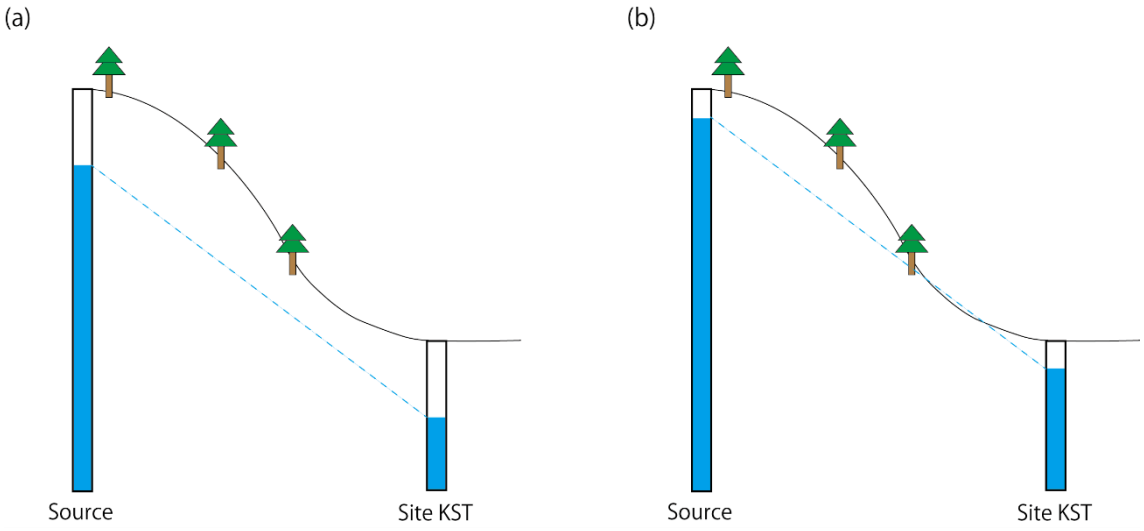

Figure 3.7. Schematic image of fluid flow at Site KST surrounded by hills. Image of water heads (a) before and (b) after earthquakes.

Table 3.1. Results of specific events.

No.	Date (JST)	Lat., °	Lon., °	Epicentral Distance, km	Depth, km	Mw	Static	Dynamic			Maximum change in groundwater level, mm	Time required for maximum change in groundwater level, min	Recovery time, min	Time constant, min	Model A (Brodsky et al., 2003)		Model B (Roeloffs, 1998)			
							Theoretical volmetric strain	PGA, cm/s^2	PGV, cm/s	Peak to peak amp. of volumetic strain					ΔA, mm	d, m	Wo, mm	L, m	L', m	x, m
1	2009/8/9	33.13	138.40	243	333	7.1	4.6×10^{-9}	7.6×10^{-1}	1.4×10^{-1}	5.9×10^{-7}	297.16	3546	9400	592	483	20	640	747	14	34
2	2010/12/22	27.05	143.94	1060	8	7.3	2.7×10^{-10}	2.9×10^{-2}	2.0×10^{-3}	4.8×10^{-7}	122.90	3819	10667	207	141	12	49	1000	80	10
3	2011/7/5	33.99	135.23	76	7	5	4.5×10^{-10}	2.7×10^{0}	1.7×10^{-1}	5.2×10^{-7}	13.76	67	206	17	20	3	11	77	0	3
4	2012/1/1	31.43	138.57	346	397	6.8	4.8×10^{-10}	2.1×10^{-1}	3.8×10^{-2}	2.3×10^{-7}	44.44	559	1953	293	80	14	120	133	5	17
5	2012/12/7	37.82	144.32	904	46	7.3	-4.5×10^{-11}	1.5×10^{-1}	1.9×10^{-2}	5.4×10^{-7}	92.71	1125	4348	268	128	10	10	107	5	17
6	2013/4/13	34.42	134.83	137	15	5.8	2.1×10^{-10}	3.3×10^{-1}	2.9×10^{-1}	1.4×10^{-6}	138.71	177	1947	76	212	4	500	50	4	9
7	2014/3/14	33.69	131.89	367	78	6.3	-6.7×10^{-11}	7.4×10^{-1}	8.9×10^{-2}	3.0×10^{-7}	92.80	685	3840	203	112	5	630	297	2	12
8	2014/11/22	36.69	137.89	400	5	6.3	-9.1×10^{-11}	9.9×10^{-2}	1.2×10^{-2}	4.6×10^{-7}	31.40	376	1129	160	19	7	77	297	2	12
9	2015/5/30	27.86	140.68	782	682	7.9	1.1×10^{-9}	5.1×10^{-1}	3.6×10^{-2}	1.2×10^{-6}	82.43	999	2695	559	104	7	163	295	6	14

Static volumetric strains were estimated based on the solutions of Okada (1992) and the focal mechanisms reported by F-net (National Research Institute for Earth Science and Disaster Prevention).

PGA, PGV and peak to peak amplitude of volumetric strain were estimated with data band-pass filtered between of 0.05 and 10 Hz.

Volumetric strains were calculated using 2 out of 4 horizontal components and the vertical component.

3.6. Discussion

The gradient of the increasing part of observed groundwater perturbations is different for each earthquake, which can be estimated from a fit using a simple exponential function (Roeloffs, 1998);

$$h(\mathrm{t}) = h_0(1 - \exp(-t/t_r)) \tag{3.10}$$

where h_0 is the preseismic groundwater level, t is time and t_r is a time constant. The range of t_r in our data is 17 to 592 minutes and the average value is 264 minutes (Table 3.1). The t_r for Events 3 and 6 are relatively small values of 17 and 76 minutes. These events are characterized by close epicentral distances from the borehole and associated values of PGA and PGV are 10 times greater than for the other events. We deduce that these events induced large perturbations in the aquifer by the large seismic waves. Even for other detectable events, the contribution of dynamic strains should be larger than static strains, for these epicentral distances. The PGA, PGV and peak to peak amplitudes of volumetric strain for specific earthquakes that produced changes in groundwater level, tend to be larger than that of other events that were not accompanied by any perturbations. However, there is no clear threshold value that triggers the hydrologic change (Fig. 3.8). Brodsky and Prejean (2005) proposed that a PGV threshold for earthquake triggering varies with time, and this idea is consistent with our results. Whereas there are other possibilities such as trends of groundwater level which may

coincide with seismic events. Even though we corrected the tidal effects in the data, there are still fluctuations associated with seasonal trends, precipitation, crustal deformation and other uncertain causes. If the occurrence of a seismic event happens at the same time as one of these changes, it would be incorrectly identified as a "coseismic change". For example, the Mw 7.3 event on December 22, 2010 recorded small PGA and PGV values, but produced detectable change in groundwater level, because background trends of groundwater level increased at that time (Fig. 3.9). These types of trends may cause apparent and ambiguous changes in groundwater level at the time of the earthquakes.

Another possibility pointed out by Brodsky and Prejean (2005), is the frequency dependence of pore pressure of interstitial fluids. In particular, the effects of Rayleigh waves characterized by lower frequency waves have been reported as a cause of changes in groundwater levels (Chadha et al., 2008; Shin et al., 2013). In our case, some of the changes in groundwater level correspond with the passage of Rayleigh wave but not for all events (Fig. 3.10). Therefore, we speculate that there are at least two contributing factors of dynamic strains to changes in groundwater level; (i) amplitude and (ii) frequency.

To investigate the possible frequency dependence, we applied several low-pass filters (cut-off frequencies of 5, 1, 0.5 and 0.2 Hz), and calculated the values of PGA, PGV and peak to peak amplitudes of volumetric strain for the earthquakes. However, there are no clear threshold of PGA, PGV and peak to peak amplitude of volumetric strain to produce changes in groundwater level. The

PGA and PGV are usually produced by body waves for close earthquake, and are usually associated with lower frequency surface waves for more distant earthquakes. If there are the events with similar amplitude and with different frequency content, we can study frequency dependence. However, our dataset is limited and we could not investigate the details of this issue.

Other holes at Site KST (Holes 1 and 3) did not show the changes in water level at the times of the events listed Table 3.1, although seismic oscillations appeared in the groundwater levels. The logging data indicates that large fractures exist in Hole 1 compared to Hole 2, but they may be local fractures. For changes in borehole water level, permeable layers on a large scale are important. The difference in borehole penetration depth enables observation of several types of fractures, and thus might have produced the difference in responses of groundwater level. If a borehole penetrates a permeable layer having many and large fractures, interstitial water can flow easily into the borehole. This phenomena would enhance the sensitivity of Hole 2 compared to other boreholes which penetrate into less permeable layer.

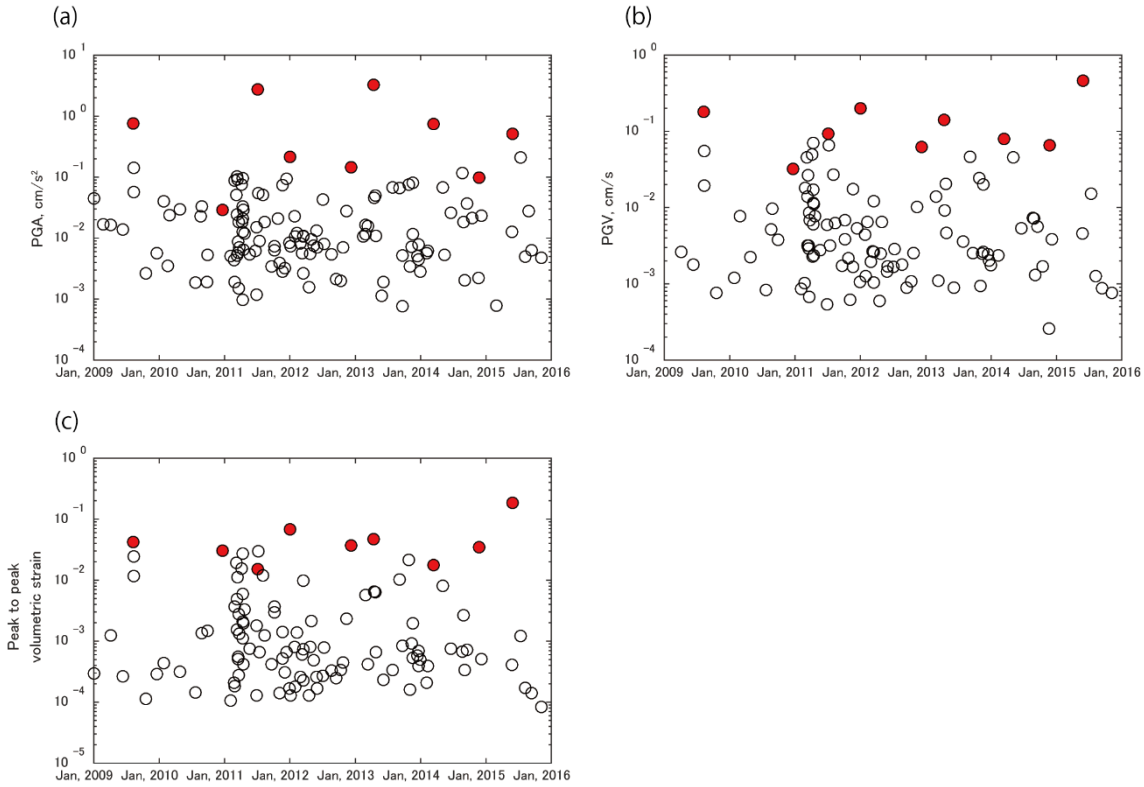

Figure 3.8. Estimates of (a) PGA, (b) PGV and (c) peak to peak amplitudes of volumetric strain for the studied earthquakes. Red circles are events that produced detectable changes in groundwater levels, and black circles represent other events that did not produce any change in groundwater levels.

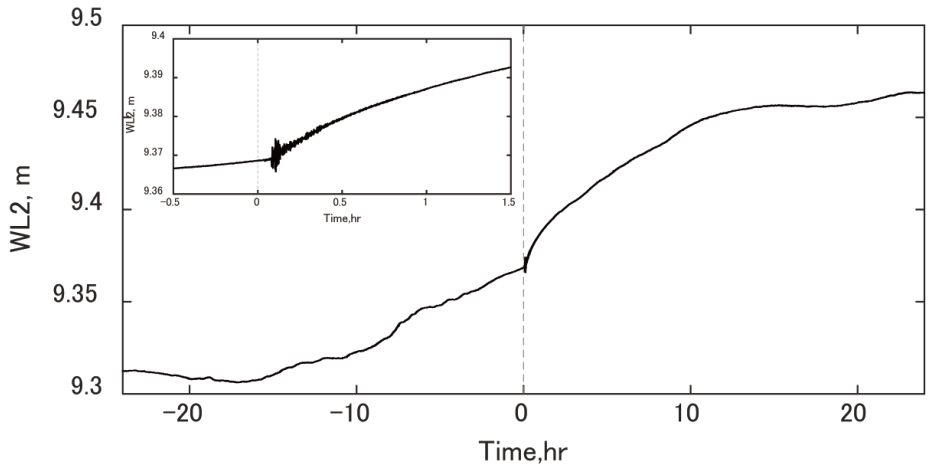

Figure 3.9. Response of groundwater level produced by the Mw 7.3 earthquake on Dec. 22, 2010 (Table 3.1). Dashed line is the time of earthquake occurrence. Insert is enlarged figure of the coseismic

response of groundwater level.

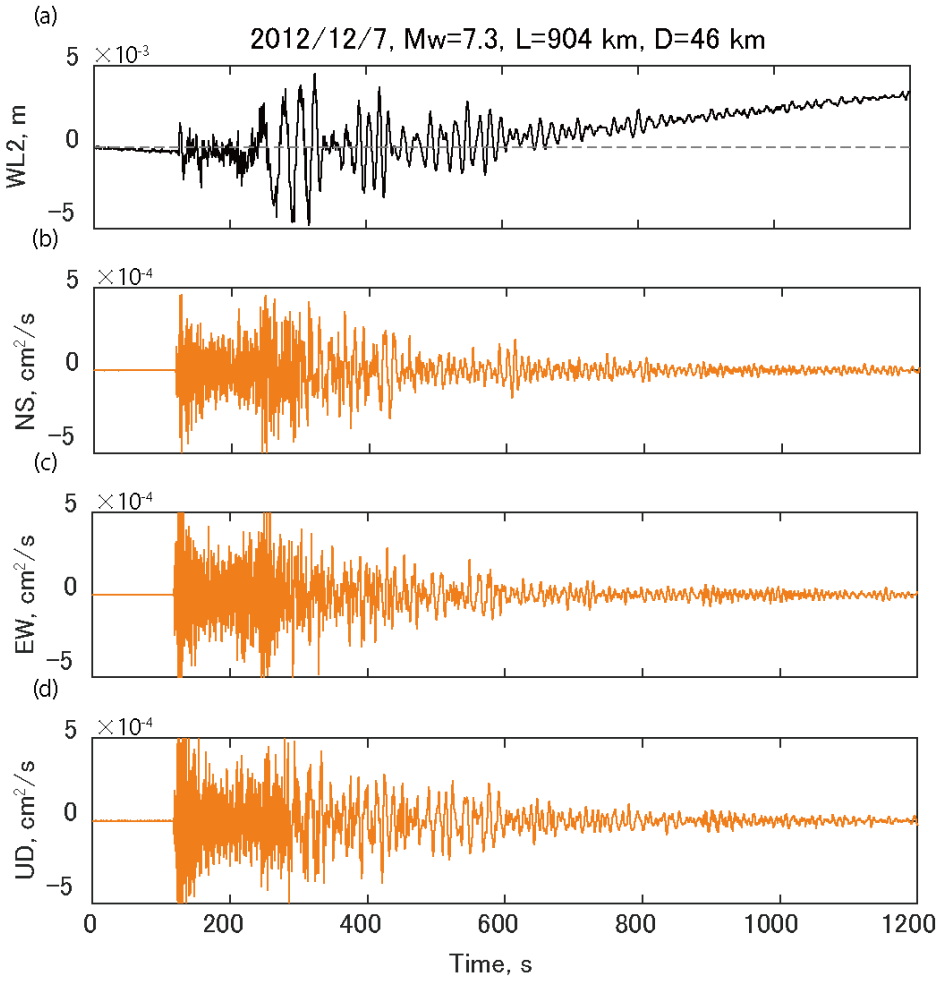

Figure 3.10. Response of groundwater level and ground velocity produced by the Mw 7.3 earthquake on Dec. 7 2012. (a) Water level and acceleration of (b) NS, (c) EW and (d) UD components.

3.7. Summary

Hole 2 of Site KST is sensitive to the hydrological perturbations of the subsurface produced by the earthquakes. Responses of groundwater level to the earthquakes and the existence of a fixed source location for the change in water head suggest that there is a particular mechanism for the similar hydrologic response to a variety of earthquakes. The sensitivity of hydrologic measurements is strongly affected by the local geologic conditions of the borehole. Sensitivity of water level depends significantly on the local permeability of the rock layer at the penetration depth. We were not able to identify clear thresholds in the amplitude and/or frequency of ground motions that produced the water level changes, but our results indicate that the earthquakes with larger seismic waves amplitudes tend to induce the changes in groundwater level. The specific level of triggering for the hydrologic response may be related to variable thresholds with time, effects of amplitude and frequency and other factors related to the local conditions of the borehole and aquifer. These effects will be investigated in future studies.

Chapter 4. Changes in Physical properties of the Nankai Trough Megasplay Fault Induced by Earthquakes, Detected by Continuous Pressure Monitoring Observed in an Oceanic Borehole

4.1. Introduction

In addition to the onshore boreholes, oceanic boreholes also have been developed for the last several decades and contributed to the elucidation of relationships between interstitial fluids and seismic nucleation. In particular, at specific subduction zones such as Cascadia, Barbados, Juan de Fuca Ridge, Mariana flank, Costa Rica Rift south flank, and Nankai Trough, oceanic borehole monitoring systems have been deployed (Becker and Davis, 2005). Objectives of oceanic boreholes are not only detection of general earthquakes, but also recording of slow slip events (SSEs), tectonic tremors (TT), and very low frequency earthquakes (VLFEs). Davis et al. (2011) observed the gradual changes in pore pressure with amplitudes of tens of kPa produced by SSEs and subsequent VLFE activities, which were recorded by oceanic boreholes in the subduction prism off the Nicoya Peninsula, Costa Rica. They suggested that the time delay between pressure transients and VLFE activities would be evidence for slow slip propagation or delayed deformation at the outer part of the prism. In addition, Araki et al. (2017) reported repeated SSEs from pore pressure records monitored by two boreholes located at the Nankai Trough, Japan. Estimated slip regions of the SSEs correspond with the slip zone of past great

earthquake (Tonankai earthquake; Kikuchi et al. (2003)), which also supports the assertion that accumulated stress by plate subduction is released by SSEs.

However, borehole monitoring in oceans has a relatively short history compared to onshore observations and the number of boreholes is also significantly smaller. More offshore observations will be required for a better understanding of the fundamental response of pore pressure monitored in the oceanic boreholes to regular seismic events which are studied in the paper.

In this study, we use continuous monitoring of formation pore fluid pressure in a sealed borehole to define changes in pore pressure and associated rock properties within a fault zone in the Nankai subduction zone, located offshore southwest Honshu in Japan (Fig. 4.1). The borehole observatory was installed at Integrated Ocean Drilling Program (IODP) Site C0010 as part of the Nankai Trough Seismogenic Zone Experiment (NanTroSEIZE) (Expedition 332 Scientists, 2011a). From a timeseries of formation pore pressure within the fault zone, we investigate two phenomena: (1) pore pressure (formation pressure) responses to ocean tidal loading which can be indicators of formation hydraulic properties; (2) step changes in pore pressure and associated changes in the tidal loading efficiency induced by earthquakes. We then explore possible mechanisms for the earthquake-induced changes in pore pressure and loading efficiency by considering the effects of static and dynamic strains.

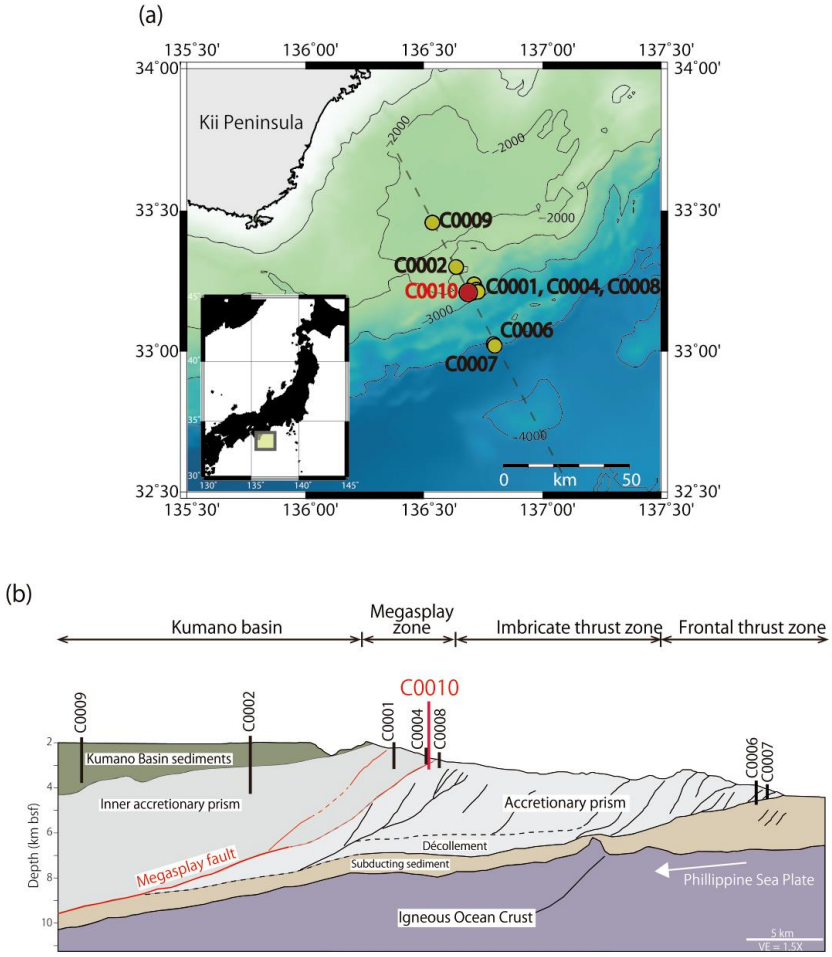

Figure 4.1. Location of NanTroSEIZE drillsites (modified from Kopf et al., 2016). (a) Map of the drilling sites (circles). We focus on analysis of data from a temporary observatory installed at Site C0010 (red circle), which penetrates the shallow megasplay fault at 407 meters below sea floor (mbsf). (b) Schematic image of cross section along gray dashed line in (a).

4.2. Geological Setting

4.2.1. Nankai Trough Subduction Zone

The Nankai Trough is one of the best globally studied subduction zones, with numerous drilling efforts, geophysical surveys and earthquake studies aimed at understanding the margin's structure,

earthquake processes, hydrogeology, and tectonic history (e.g., Moore et al, 2007; Strasser et al., 2009; Hirose et al., 2010; Kinoshita et al., 2011). The Nankai Trough is located offshore southwest Honshu Japan, where the Philippine Sea plate subducts northwestward beneath the Eurasian Plate at ~ 6.5 cm per year (Seno et al., 1993; Miayazaki and Heki, 2001). Offscraping of trench fill and hemipelagic sediments of the Shikoku Basin on the Philippine Sea Plate has formed a wide accretionary prism with well-developed fold-and-thrust belt structures (e.g., Aoki et al., 1982; Park et al., 2000; Moore et al., 2009) (Fig. 4.1(b)). The megasplay fault forms a boundary between the active outer accretionary prism and a less active inner prism that is overlain by Pleistocene sediments of the Kumano Basin.

IODP Site C0010 intersected the megasplay fault near its updip termination, at a depth of 407 meters below sea floor (mbsf) (Expedition 319 Scientists, 2010; Fig. 4.2(a)). The borehole penetrated three lithological units as defined on the basis of logging while drilling (LWD) and coring (McNeill et al., 2010). These are thought to represent the regional geology of the shallow megasplay, and include: (i) Pleistocene slope sediments (Unit I, 0-182.8 mbsf) composed of hemipelagic mud and minor turbidite interbeds; (ii) a thrust wedge (Unit II, 182.8-407 mbsf) composed of Pleistocene clay and mudstones uplifted by movement on the fault; and (iii) overridden Pleistocene slope sediments (Unit III, > 407 mbsf) composed of hemipelagic mud (Table 4.1; Expedition 319 Scientists, 2010).

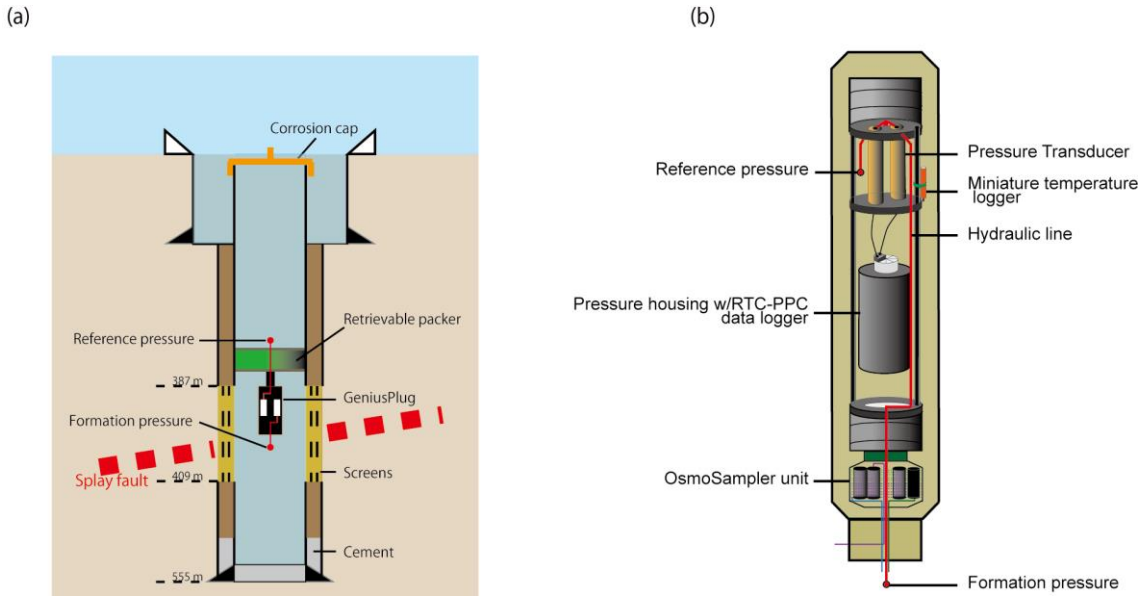

Figure 4.2. Schematic images of (a) Hole C0010A and (b) GeniusPlug (modified from Kopf et al., 2016). (a) The total depth of borehole is 555 mbsf, and it crosses the megasplay fault at 407 mbsf. Screened casing joints provide access to the formation over a zone spanning 387-409 mbsf. (b) The GeniusPlug is equipped with two pressure sensors (for formation and reference pressures) and three different temperature sensors (after Expedition 332 Scientists, 2011c).

Table 4.1. Lithologies of Site C0010.

Site	C0010
Water depth, m	2524 m
Unit	Structural geology
Unit I (0-182.8 mbf)	Slope sediments Hemipelagic mud Minor turbidite
Unit II (182.8-407.0 mbf)	Accreated sediments (Thrust wedge) Mudstone and claystone
Unit III (407.0-555.1 mbf)	Slope deposits Hemipelagic mud

4.2.2. Borehole Observatory Configuration and Deployment

Hole C0010A was drilled in 2009 during IODP Expedition 319, in 2524 m water depth, and to a total depth of 555 mbsf. The borehole was completed by installing casing with screens spanning the depth interval from 387-409 mbsf, allowing hydraulic access to the fault zone (Fig 4.2(a)). At the time the hole was drilled and completed, an initial temporary instrument package (termed a "SmartPlug") was suspended in the hole below a retrievable packer (a bridge plug) that was set within the casing and above the screened interval (Expedition 319 Scientists, 2010). The bridge plug served to isolate the monitoring interval from the overlying ocean, and the instruments initially recorded pore pressure and temperature at the depth of the screens, as well as an overlying ocean reference pressure from

August 2009 until December 2010 (Expedition 332 Scientists, 2011b). This instrument package was recovered in 2010 as part of IODP Expedition 332, and replaced with a "GeniusPlug" having fluid sampling capabilities (Expedition 332 Scientists, 2011b). Analysis of the SmartPlug deployment records has provided initial information about pore pressure and temperature responses to earthquakes, as well as preliminary estimates of formation properties (Hammerschmidt et al., 2013a, b). However, these analyses are limited by the short duration of the deployment, and by partial decoupling of the reference pressure sensor from the overlying ocean by a cap at the wellhead, which led to incomplete accounting for oceanographic and tidal signals (Hammerschmidt et al., 2013a, b).

Like the Smartplug, the GeniusPlug included two pressure sensors, a "downward-looking" sensor to record formation pore pressure in the screened interval, and an "upward-looking" sensor to measure an oceanographic reference pressure, both with a sampling interval of 30 s and ± 0.7 Pa pressure precision (Fig. 4.2(b)). Both of the pressure sensors can measure 7000 m water depth as the full scale pressure (Saffer et al., 2017) and a calibration test was conducted before the installation. In addition, the observatory was equipped with three temperature sensors, primarily for compensation of the pressure transducers (e.g., Expedition 332 Scientists, 2011b; Hammerschmidit et al., 2013a), and a ~30 cm-long extension at its lower end housing a fluid sampling and in situ microbiological experiment designed to collect a time series of samples for geochemical and microbiological research (Expedition 332 Scientists, 2011b). The GeniusPlug monitored pressure continuously from its initial

deployment on November 6, 2010 until recovery of the instruments on April 3, 2016 (Expedition 332 Scientists, 2011b; Kopf et al., 2016). Here, we restrict our analysis to a 5.3 year time series of pressure data.

4.3. Methods

Ocean tidal loading results in periodic variations in total stress at the seafloor. The formation response to this transient oceanographic loading includes an elastic component, which is instantaneous and characterized by amplitude damping that depends on formation and pore fluid stiffnesses; and a diffusive component generated at boundaries (i.e., the seafloor or at the top and base of layers in the subsurface having differing elastic properties) (e.g., Wang and Davis, 1996). The amplitude damping results from contributions from both the elastic and diffusive responses, and is described by a 1-D loading efficiency (γ), given by the ratio of the amplitude of variations in pore pressure to that of the ocean tidal loading at the seafloor. The diffusive component of the response can also result in phase lags or leads of pore fluid pressure in the formation relative to the oceanographic signal, but for typical sediment hydraulic diffusivities this effect becomes negligible by a few tens of meters away from boundaries at dominant ocean tidal frequencies.

An added complication arises in the measurement of pressure in sealed borehole observatories, in

which both amplitude damping and phase lags may also be generated by the transfer of fluid mass between the formation and the borehole sensing volume, necessary to measure and record pressure changes (Sawyer et al., 2008). This effect is governed by the hydraulic diffusivity of the formation, which controls the rate of fluid movement into and out of the borehole, and by the ratio of formation to instrument compliance, which defines the pressure change associated with a given fluid mass transfer (Sawyer et al., 2008; Hammerschmidt et al., 2013b).

As described in detail in the following sections, we define the overall average tidal loading efficiency, and use the observed in-phase pore pressure to seafloor loading to provide bounds on formation hydraulic diffusivity. We then determine a time series of small but clearly resolved variations in pressure and loading efficiency over the 5.3 year deployment, and evaluate the relationship between these perturbations and regional earthquakes.

4.3.1. Removal of Tidal and Oceanographic Signals

The GeniusPlug monitored pressure continuously from its initial deployment on November 6, 2010 until recovery of the instruments on April 3, 2016 (Expedition 332 Scientists, 2011b; Kopf et al., 2016). The monitoring period included both the installation and recovery of the GeniusPlug, during which there are large pressure excursions related to the drillstring operations in the hole. To avoid these

effects and the transient equilibration following initial deployment, we limited our analysis to the time window from one week following the end of installation (Nov. 13, 2010) until the time of recovery. The pressure data are dominated by the diurnal ocean tidal signal with an amplitude of approximately 10 kPa, along with a semi-diurnal component of roughly half this amplitude (Fig. 4.3(a)). The tidal signal is far larger than transient changes in pressure associated with earthquakes or other tectonic phenomena, and analyses of the latter therefore requires that the effects of ocean tides be removed. We observe essentially no phase lag in pore pressure relative to the reference pressure, which simplifies the removal of tidal signals (e.g., Wang and Davis, 1996; Davis et al., 2009, 2013). In this case, we simply remove the tidal effects from the pore pressure directly to define a corrected pressure (P_{corr}) using the "upward looking" reference pressure and accounting for amplitude damping by the 1-D loading efficiency (γ) (e.g., Davis et al., 2009 and 2013):

$$P_{corr} = P_{form} - \gamma P_{ref} \tag{4.1}$$

where P_{form} and P_{ref} are the formation and reference pressures, respectively.

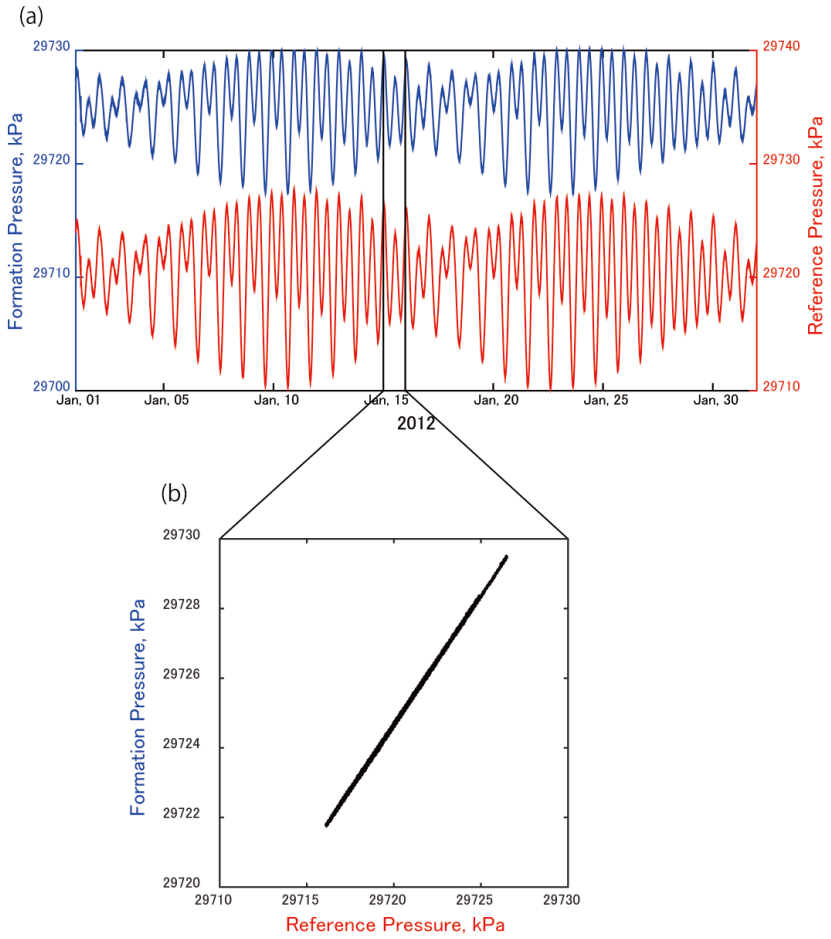

Figure 4.3. Example of tidal and oceanographic signals in the observed pressures. (a) Time series observed pressures from Jan.1 - Feb. 1, 2012. Blue and red lines show formation and reference pressures, respectively. (b) Example of loading efficiency estimation for a 1 day time window (Jan. 15-16) which includes both diurnal and semi-diurnal components. The slope between formation to reference pressures indicates the loading efficiency.

4.3.2. Definition of tidal loading efficiency (γ)

In most analyses, loading efficiency is assumed to remain constant over time, and is used to remove tidal and oceanographic signals from pressure records as described above (e.g., Sawyer et al., 2008; Hammerschmidt et al., 2013b). However, the loading efficiency reflects the formation's elastic and

hydraulic properties, and therefore can vary over time due to tectonic or other processes. This has been recognized in the analysis of groundwater observations in onshore boreholes, and combined observations of amplitude damping and phase lag have been used in several studies to define variations in formation hydraulic diffusivity caused by earthquakes (e.g., Elkhoury et al., 2006; Kinoshita et al., 2015).

To explore potential temporal variations in loading efficiency, we computed γ on a daily basis by cross-plotting the reference and formation pressures for each 24 h window (Fig. 4.3(b)); this captures the diurnal variations in both datasets. For this analysis, we first applied a low-pass filter (cut-off frequency 10^{-4} Hz) to the pressures to extract the tidal frequencies and remove any perturbations induced by seismic waves.

4.3.3. Identification of Regional Earthquakes and Definition of Pressure Changes

Guided by previous work that demonstrates a clear relationship between hydrologic signatures and earthquake magnitude and distance (e.g., Wang, 2007; Manga et al, 2016), we identify earthquakes to compare with the observatory data by focusing on regional events with epicenters located between latitude 25-45°, and longitude 125-150° (epicentral distances < 1200 km), and having moment magnitude (Mw) ≥ 6.0. We also consider events with Mw 5.0-5.9 having epicentral distances < 300

km. Aftershocks of the 2011 Mw 9.0 Tohoku earthquake from March 11-14, 2011 are not considered because it is difficult to distinguish individual events, especially given the relatively coarse sampling interval (30 s). If multiple earthquakes occurred on the same day, we selected the larger Mw event for our analysis. We use earthquake data from the F-net Catalog (based on the F-net Broadband Seismograph Network; Fukuyama et al., 1998) which includes a focal mechanism for each event; we use these focal mechanisms to predict the theoretical static volumetric strain for each event as described in Section 4.4.2.

After removal of tidal and oceanographic signals (Eq. (4.1)), clear step changes in pressure are apparent and correspond to regional and large teleseismic events (Fig. 4.4(a)). However, there are still local trends in the data related to recovery from drilling perturbations and to instrument drift. In order to define the magnitude of individual pressure steps, we de-trended the data by assuming a constant drift rate defined over a moving three-month window. For data prior to December 27, 2010 (less than three months after the start of data collection), a one-month window was used instead. To define the size of pressure steps, we calculated a 10 minute average of de-tided and de-trended pressure before and after each event (Fig. 4.5).

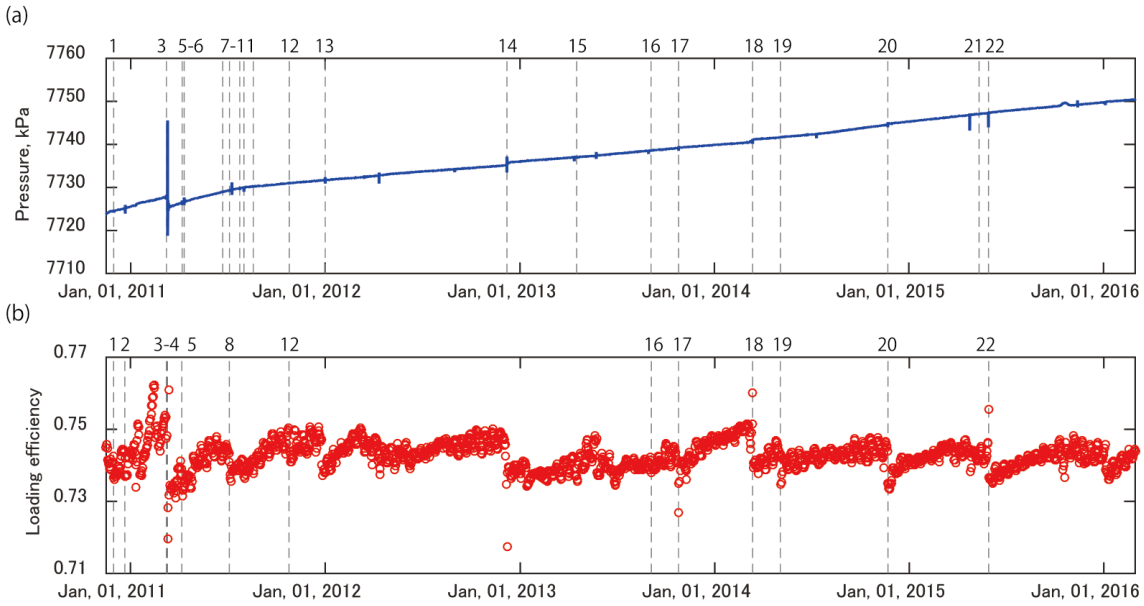

Figure 4.4. Time series of (a) pressure and (b) loading efficiency. (a) Pore pressure with tides removed, corrected as described in the text. The dashed lines indicate the timing of earthquakes that produced detectable changes in pressure and/or loading efficiency. The numbers above dashed lines correspond to the events listed in Table 4.3.

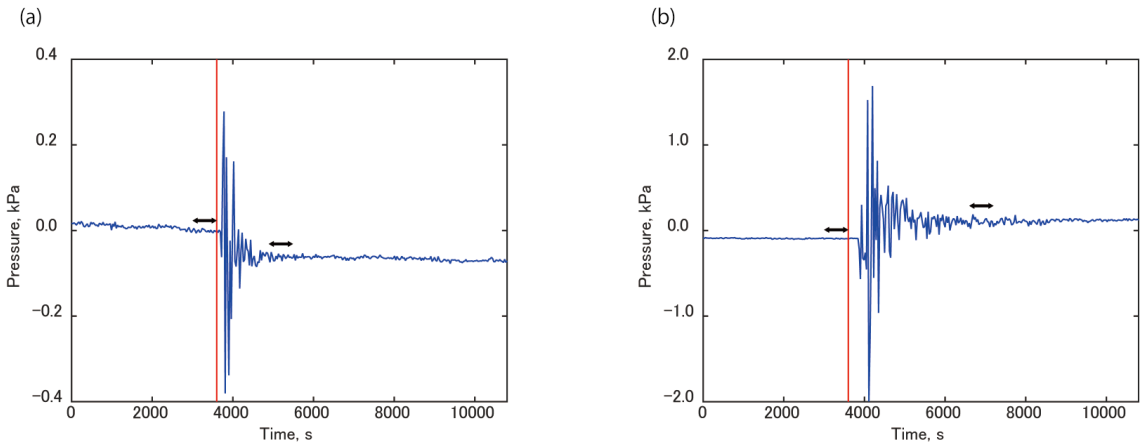

Figure 4.5. Examples of pressure step changes. (a) Example of pressure decrease in response to an earthquake on Nov. 30, 2010 (Event 1 listed in Table 4.3). (b) Example of pressure increase (earthquake on Dec. 7, 2012; Event 14 listed in Table 4.3). The black arrows show the periods used to define a 10 minute average before and after the event. Red line is origin time of the earthquake.

4.4. Results and Discussions

The overall amplitude and phase lag (if present) responses to cyclic loading provide information about formation hydraulic properties (e.g., Wang and Davis, 1996; Sawyer et al., 2008). In addition, shifts in these quantities over time reflect hydrological perturbations in the formation or to the well completion that yield insights into transient hydrological and deformation processes (e.g., Elkhoury et al., 2006; Kinoshita et al., 2015).

4.4.1. Amplitude and Phase Responses: Constraints on Formation Properties

Our analysis reveals essentially no phase lag within the limits of our 30 s sampling interval, and an overall value of γ=0.74 ±0.004 (2σ), with small but clearly resolvable changes superimposed on the time series (Fig. 4.4(b)). The loading efficiency we obtain is similar to that of γ=0.73 reported by Hammerschmidt et al. (2013b) using pressure records from the previously deployed SmartPlug. The standard deviation in any given single year of the timeseries is slightly smaller than that for the entire dataset (2σ=~±0.003) and we consider this as a detection limit for resolving changes in loading efficiency that occur over short timescales (i.e., those associated with earthquakes). To identify transient changes in loading efficiency that could be linked to individual earthquake or other events, we apply an additional criterion that the loading efficiency must recover.

4.4.1.1. Loading Efficiency and Formation and Fluid Compressibilities

Generally, the lack of phase lag in formation pressure relative to the reference pressure signifies good hydraulic coupling between the formation and observatory (e.g., Gibson, 1958; Sawyer et al., 2008). This is consistent with the placement of the hydraulic screens spanning a fractured and presumably permeable interval associated with and immediately above the megasplay fault (Expedition 319 Scientists, 2010; Kopf et al., 2016). Unrestricted hydraulic communication between the formation and well should also lead to near zero amplitude damping of the formation's response to periodic loading as measured in the borehole sensing volume (Sawyer et al., 2008; Hammerschmidt et al., 2013b). This lends confidence that the loading efficiency of 0.74 observed in the borehole is correctly representative of that of the formation.

The formation's 1-D loading efficiency is given by (Wang, 2004; Sawyer et al., 2008):

$$\gamma = \frac{\beta_f'}{\beta_f' + n\beta_w} \tag{4.2a}$$

where

$$\beta_f' = \frac{1+\nu}{3(1-\nu)}\beta_f \tag{4.2b}$$

and β_f and β_w are the formation and fluid volumetric compressibilities (Pa^{-1}), respectively, β_f' is the 1-D vertical formation compressibility (Pa^{-1}), n is fractional porosity, and *v* is the Poisson's ratio (all variables and their values are listed in Table 4.2). However, for values of sediment compressibility consistent with values measured on core samples from equivalent depths of the monitoring interval and assuming pure seawater as pore filling phase, γ determined from Eqs. (4.2) would be > 0.95 (e.g., Wang and Davis, 1996; Davis et al., 2009).

In order to explain the observed value of γ=~0.74, the required formation compressibility would be ~10 times smaller than measured in laboratory experiments for sediments from the megasplay, or similar lithologies elsewhere (e.g., Guo et al., 2011). Alternatively, the presence of a small amount of either free or dissolved gas in the interstitial fluids could lead to decreased loading efficiency (Wang and Davis, 1996; Wang et al., 1998). This occurs because the compressibility of gas is much higher than that of seawater. To evaluate this possibility, we modify Eq. (4.2) to consider the effects of gas compressibility and solubility (Wang et al., 1998). In this case, the term $n\beta_w$ in Eq. (4.2a) is replaced by β_{w+g} (Wang et al., 1998):

$$\begin{aligned}\beta_{w+g} &= \frac{1}{V}\left[V_w\beta_w + V_g\beta_g + \chi V_\chi\left(\beta_g - \beta_w - \beta_\chi\right)\right] \\ &= \left(1 - n_g\right)\beta_w + n_g\beta_g + (1 - n_g)\chi(\beta_g - \beta_w - \beta_\chi)\end{aligned} \tag{4.3}$$

where V is volume (m^3), β is compressibility (Pa^{-1}), χ is volumetric solubility, and the subscripts, w, g and χ represent water, gas and dissloved gas, respectively. Wang et al. (1998) showed the ratio of bulk moduli of water and water-dissolved gas as a function of gas fraction with various confining pressures (Fig. 4.6(a)). Their estimation of volumetric solubility of methane gas for confining pressures (Fig. 4.6(b)) shows $\chi = 0.018$ at the pressure-temperature conditions of the monitoring depth of the GeniusPlug with hydrostatic pressure of 31 MPa and 20 ℃. We searched the values of gas fraction to obtain $\gamma = 0.74$ using Fig. 4.6 and the formation properties listed in Table 4.2. A volumetric gas content of ~0.5 % would be sufficient to explain the observed loading efficiency. The presence of dissolved and possibly free gas in the in situ pore fluids is supported by the observation of abundant free gas in the geochemical sampling coils of the GeniusPlug upon recovery and depressurization (Saffer et al., 2017).

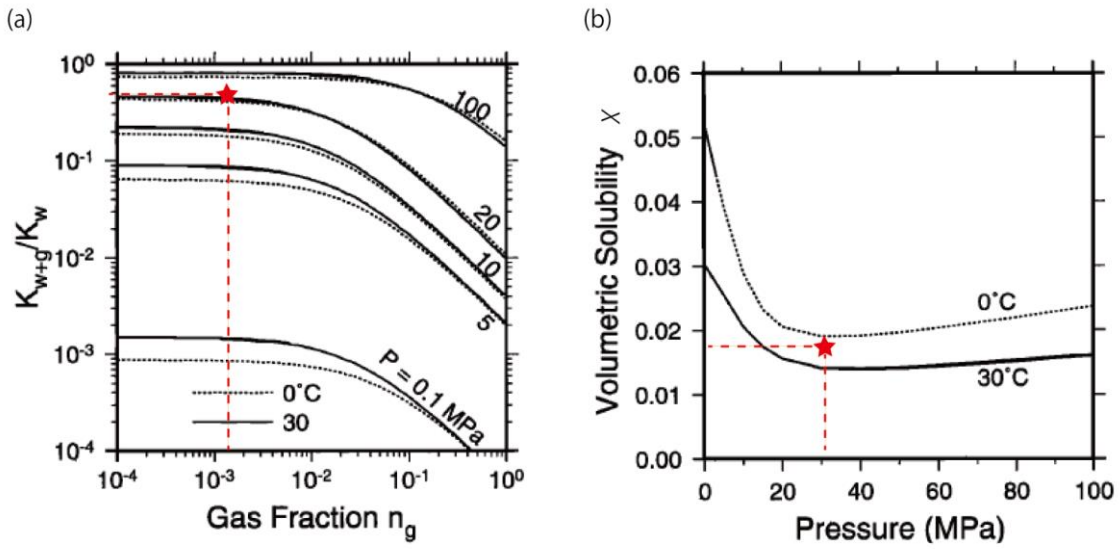

Figure 4.6. Bulk modulli of water and water-dissolved gas and volumetric solubility of methane gas. (a) Bulk modulli of water and water-dissolved gas against gas fraction with various confined pressures (modified Wang et al., 1998). Bold and dashed lines show the variation of $\frac{K_{w+g}}{K_w}$ at 30 ℃ and 0 ℃, respectively. (b) Volumetric solubility of methane gas against confined pressures (modified Wang et al., 1998). Bold and dashed lines show the variation of χ at 30 ℃ and 0 ℃, respectively. The Red stars indicate the values of $\frac{K_{w+g}}{K_w}$ and volumetric solubility used in our calculation assuming the condition of the observatory depth with hydrostatic pressure of 31MPa and 20 ℃.

Table 4.2. Definitions and values (where appropriate) of variables used in the text.

Variable	Definition	Dimension
γ	Average 1-D Loading efficiency	0.74
β_f	Formation compressibility, Pa^{-1}	7.0×10^{-9}
β_f'	1-D vertical formation compressibility, Pa^{-1}	2.9×10^{-9}
β_w	Fluid compressibility, Pa^{-1}	4.0×10^{-10}
β_{steel}	Steel compressibility, Pa^{-1}	5.0×10^{-12}
β^*	Instrument compressibility, Pa^{-1}	3.3×10^{-10}
β_D	Formation-instrument compressibility ratio	28.9
n	Porosity	0.38
v	Poisson ratio	0.10
r_{to}	Tubing outer radius, m	0.044
r_{go}	GeniusPlug outer radius, m	0.100
r_{ci}	Casing inner radius, m	0.112
r_{co}	Casing outer radius, m	0.122
r_{so}	Screen outer radius, m	0.142
L_t	Tubing length, m	19.19
Z	GeniusPlug length, m	1.65
H	Observatory system Length, m	145.97
h	Screen part length, m	18.39
V_w	Volume of water, m^3	5.60
V_{steel}	Volume of steel part, m^3	1.25
V	Total volume, m^3	6.85
μ	Fluid viscosity, Pa·s	1.0×10^{-3}
$P(r,t)$	Pressure, Pa	-
P_D	Dimensionless pressure	-
r	Distance, m	-
r_D	Dimensionless distance	-
t	time, s	-
t_D	Dimensionless time	-
f	Frequency, rad	-
f_D	Dimensionless frequency	-
S_D	Dimensionless fluid source term	-
A	Amplitude, %	-
ζ	Phase lag, rad	-

4.4.1.2. Hydraulic Diffusivity

The lack of phase lag also allows us to define a lower bound on formation hydraulic diffusivity. We follow the approach of Sawyer et al. (2008), who considered measured pressure variations in a borehole in response to periodic fluctuations of pore pressure to reflect radial flow of fluid into and out of the sensing volume from the surrounding rock (Gibson, 1958). Here, we ignored a vertical flow which can be represented in terms of a series of dimensionless parameters (Gibson, 1958; Hsieh et al., 1987; Sawyer et al., 2008);

$$\frac{\partial^2 p_D}{\partial r_D^2} + \frac{1}{r_D}\frac{\partial p}{\partial r_D} + S_D(t_D) = \frac{\partial p_D}{\partial t_D} \tag{4.4}$$

where the dimensionless pressure (p_D), radius (r_D), time (t_D), fluid source term if present (S_D), and frequency (f_D) in radians are given by:

$$p_D = \frac{p(r,t)}{p(\infty,t)} \tag{4.5}$$

where p is the pore pressure in the formation and $p(\infty,t)$ represents the pore pressure in the far field, away from the influence of the well (all variables and their definitions are listed in Table 4.2).

$$r_D = \frac{r}{r_{so}} \tag{4.6}$$

$$t_D = \frac{ct}{r_{so}} \tag{4.7}$$

$$S_D(t_D) = f_D \cos(f_D t_D) \tag{4.8}$$

$$f_D = \frac{r_{so}^2 f}{c} \tag{4.9}$$

where r is the horizontal distance from the center of borehole (pressure sensor is installed at the center of borehole; m), r_{so} is the screen outer radius (m; Fig. 4.7), t is time (s) and c is hydraulic diffusivity (m^2/s). We took the frequency of a diurnal tide (1/24h) for f (s^{-1}) as a representative value.

In this model, the measured amplitude and phase response to pressure fluctuations in the formation depends on the hydraulic diffusivity of the formation, the frequency of the fluctuations, and the ratio of formation and sensing volume compressibilities (Fig. 4.8) (Hsieh et al., 1987; Sawyer et al., 2008). The formation and instrument compressibility ratio (β_D), which governs the response of the pressure monitoring system (the sealed borehole volume) to fluid mass exchange with the formation. The formation-instrument compressibility ratio is given by (Sawer et al., 2008):

$$\beta_D = \frac{\pi r_{so}^2 H \beta_f}{\beta^* V} \tag{4.10}$$

In our case, formation compressibility (β_f) is constrained by laboratory experiments (Table 4.2). Saffer et al. (2011) performed the CRSC (Constant Rate-of-Strain Consolidation) tests on core samples from the underthrust slope apron (UNIT IV) at Site C0004, located 3.5 km away along-strike. In this experiment, the specimen is deformed at a constant rate of uniaxial strain and lateral deformation is confined by a steel ring. Circumferential pressure (back pressure) is controlled during the experiment and a formation compressibility can be estimated from changes in specimen height, total axial stress and pore pressure of the specimen (See Saffer et al. (2011) for the details).

Here we derive the instrument compressibility (β^*), which represents the aggregate of the fluid and steel compressibilities in the sensing volume. This parameter includes the fluid in the borehole casing below the retrievable packer and above the cement plug at the base of the casing, as well as the steel tubing of the instrument package (Fig. 4.7). The volumes of water (V_w) and steel (V_{steel}) in the sensing volume of the observatory are defined as:

$$V_w = \pi\{r_{ci}^2 H - (r_{to}^2 L_t + r_{go}^2 \mathrm{Z})\} \tag{4.11}$$

$$V_{steel} = \pi H\left(r_{co}^2 - r_{ci}^2\right) + \pi(r_{to}^2 L_t + r_{go}^2 \mathrm{Z}) \tag{4.12}$$

where L_t is the length of steel pipe (3" tubing) above the instrument package (m; Fig. 4.7), *Z* is the length of the instrument package (m), *H* is the length of the open casing volume below the packer and above the cement (m), and r_{to} is the tubing outer radius (m), r_{go} is the GeniusPlug outer radius (m), r_{ci} is the casing inner radius (m), r_{co} is the casing outer radius (m). The total volume (V) is simply the sum of V_w and V_{steel} (m^3), and the instrument compressibility (β^*) is given by the aggregate of the two, weighted by the volumetric proportions of each:

$$V = V_w + V_{steel} \tag{4.13}$$

$$\beta^* = \beta_w \frac{V_w}{V} + \beta_{steel} \frac{V_{steel}}{V} \tag{4.14}$$

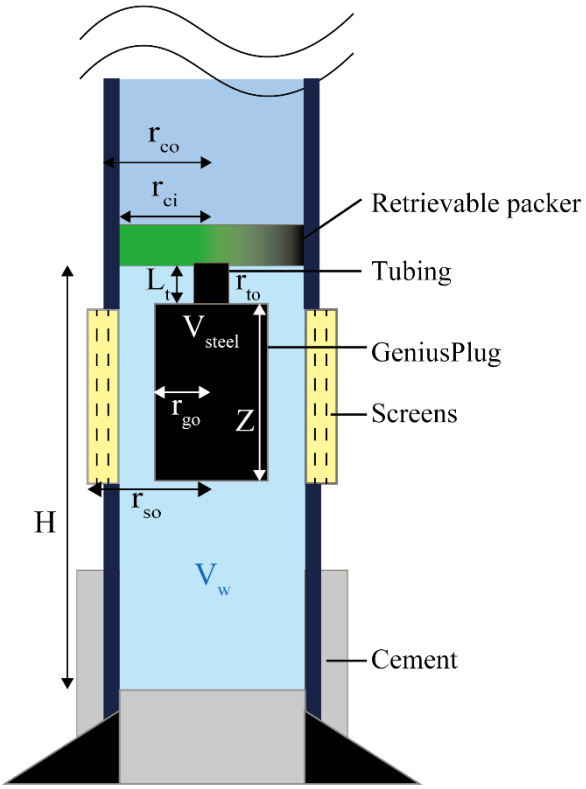

Figure 4.7. Engineering specifications of Hole C0010A and GeniusPlug (modified from Kopf et al., 2016).

One of boundary conditions represents the pressure communication between the formation and borehole (Sayer et al., 2008) is:

$$\frac{\partial p_D^m}{\partial t_D} = \beta_D \frac{\partial P_D}{\partial r_D} \qquad \text{at} \qquad r_D = 1 \tag{4.15}$$

where p_D^m is dimensionless pressure at the screen which is normalized following Eq. (4.5).

We assumed a no-flow boundary condition for a long distance from the observation borehole;

$$\frac{\partial P}{\partial r} \to 0 \qquad \text{at} \qquad r \to \infty \tag{4.16}$$

Sawyer et al. (2008) modified Hsieh et al. (1987)'s model for the case of a sealed borehole, and derived the following relationship between amplitude (A) and phase shift (ζ) in pore pressure relative to the ocean tidal loading (reference pressure), which depends on the dimensionless frequency (f_D) and the formation-instrument compressibility ratio (β_D) as shown in Fig. 4.8 (see Eq. (4.10)).

$$A = (E^2 + F^2)^{-\frac{1}{2}} \tag{4.17}$$

$$\zeta = -\tan^{-1}\left(\frac{F}{E}\right) \tag{4.18}$$

where the imaginary parameters E and F are;

$$E = 1 - \frac{f_D}{\beta_D}\left[\Psi Ker\left(\sqrt{f_D}\right) + \Phi Kei\left(\sqrt{f_D}\right)\right] \tag{4.19}$$

$$F = \frac{f_D}{\beta_D}\left[\Phi Ker\left(\sqrt{f_D}\right) + \Psi Kei\left(\sqrt{f_D}\right)\right] \tag{4.20}$$

$Ker(x)$ and $Kei(x)$ are the real and imaginary parts of Kelvin functions of order zero, and Φ and Ψ are given by (Sawyer et al., 2008):

$$\Phi = -\frac{[Ker_1(\sqrt{f_D}) + Kei_1(\sqrt{f_D})}{\sqrt{2f_D[Ker_1^2(\sqrt{f_D}) + Kei_1^2(\sqrt{f_D})]}} \tag{4.21}$$

$$\Psi = -\frac{[Ker_1(\sqrt{f_D}) - Kei_1(\sqrt{f_D})}{\sqrt{2f_D[Ker_1^2(\sqrt{f_D}) + Kei_1^2(\sqrt{f_D})]}} \tag{4.22}$$

Generally, there is a time delay between pressure change in formation and pressure in the observatory because of the effects of wellbore storage ($\beta^* V$). Above some threshold frequencies, pressure in the observatory cannot equilibrate with variations in real pore pressure, leading to damping of the amplitude response and phase lag (Fig. 4.8); at frequencies below this threshold, the response of measured pressure is correct. This frequency dependence of the amplitude-phase response allows us to place bounds on the formation hydraulic diffusivity. For the formation-instrument compressibility ratio of our system (β_D=~29), a hydraulic diffusivity > 9.1×10^{-6} $m^2\ s^{-1}$ is required to explain the lack of phase lag. Here, the value of A in Eq. (4.17) corresponds with that of loading efficiency because both values are ratios between changes in pore pressure and reference pressure. The lack of phase lag also requires a 100 % amplitude response – i.e., that there is no damping between

the formation and borehole (c.f., Fig. 4.8), consistent with our interpretation that the observed loading efficiency (γ=0.74) is best explained as a true formation response possibly caused by a small amount of gas.

The value of hydraulic diffusivity can be converted to that of permeability by (Wang, 2000):

$$k = c\mu S_s \tag{4.23}$$

where k is permeability and μ is fluid viscosity (10^{-3} Pa · s). The specific storage, S_s is estimated independently:

$$S_s = \rho g\left(\beta_f + n\beta_w\right) \tag{4.24}$$

A hydraulic diffusivity > 9.1×10^{-6} m^2 s^{-1} corresponds to a permeability > 6.4×10^{-13} m^2 without consideration of gas dissolution. A similar, but less complete, analysis of the previously deployed SmartPlug data, yielded an estimated lower bound for hydraulic diffusivity of > 1.5×10^{-5} m^2/s (Hammerschmidt et al., 2013b). For comparison, Dugan and Daigle (2011) performed the CRSC (Constant Rate-of-Strain Consolidation) tests for core samples from the thrust wedge (Unit II) at Site C0004, and obtained a matrix permeability more than two to three orders of magnitude lower than

ours, of 3.8×10^{-15} - 1.6×10^{-16} m^2. This difference is likely due to the fact the borehole screens samples a larger volume that includes fractures (e.g., Boutt et al., 2012), and the fact that the CRSC tests measured vertical permeability.

The lower bound of fault zone permeability we obtain is generally consistent with the range of values reported for other subduction fault zones (Saffer, 2015). For example, Fisher and Zwart (1997) measured in situ permeabilities of 6.0×10^{-16} - 1.6×10^{-13} m^2 for the Barbados accretionary complex décollement zone in a series of drillstem packer experiments at the depth of 398-536 mbsf. The geology of a test site in the Barbados accretionary prism is characterized by accreted claystone and ash from clays and silt stones (Moore et al., 1988; Shipley et al., 1994). Screaton et al. (2000) reported a value of 1.2×10^{-14} m^2 for the Barbados accretionary prism from cross-hole tests over a distance of ~45 m. The permeabilties of 6.0×10^{-14} - 1.6×10^{-11} m^2 for the frontal thrust fault of the Oregon accretionary prism were reported by Screaton et al. (1995) from drillstem packer experiments similar to those of Fisher and Zwart (1997). The lithology of their test site consists of terrigenous silty clay and occasional sand layers, and the borehole extending for 178.5 mbsf penetrates the fault zone (Screaton et al., 1995). In contrast, Brown et al. (1995) obtained the permeability of $10^{-17} - 10^{-15}$ m^2 from laboratory experiments on core samples from the Oregon frontal thrust controlling effective stress (Saffer et al., 2015). The reported field observations, though sparse, are also consistent with large-scale fault permeabilities estimated from numerical modeling studies at

several margins, including Costa Rica (Spinelli et al., 2006; $\geq 10^{-14}$ m^2), Barbados (Bekins et al., 1995; 10^{-14} m^2 at steady state and 10^{-13} -10^{-11} m^2 in transient simulations), and Nankai (Skarbek and Saffer, 2009; 10^{-15} -10^{-13} m^2, although the scales of these permeabilities assume a few tens of kilometers which cannot be obtained from laboratory and in situ experiments.

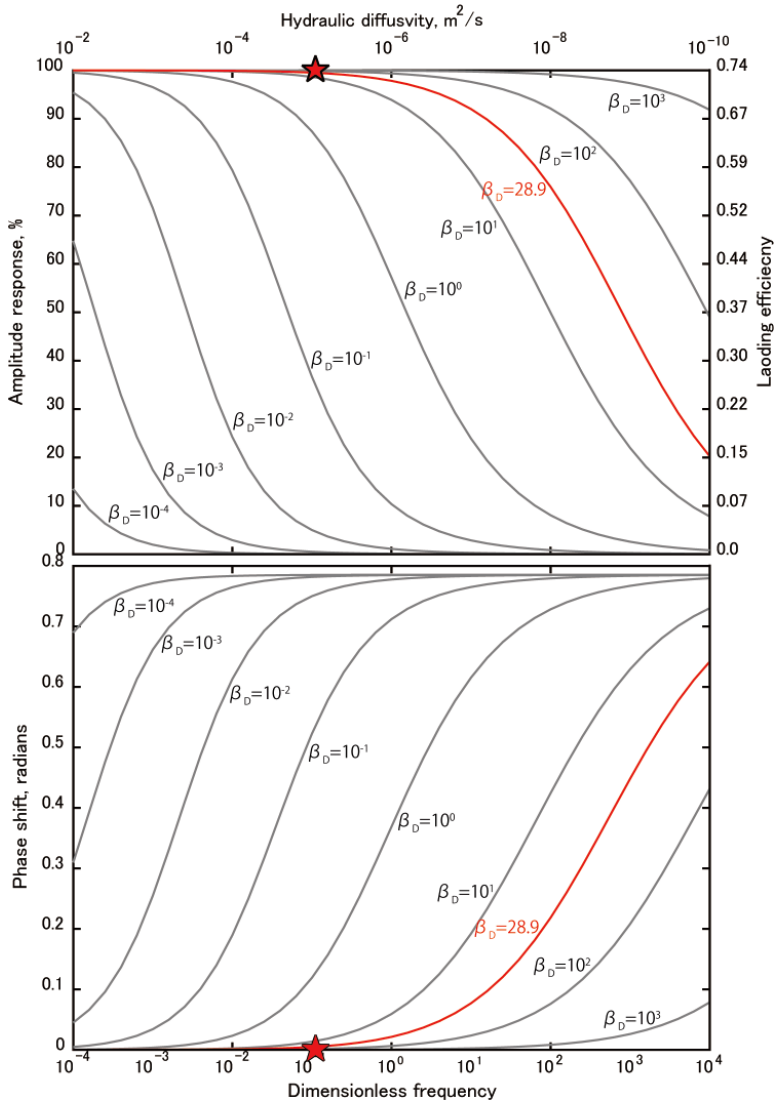

Figure 4.8. Predicted amplitude (A) and phase lag (ζ) in formation pressure relative to reference pressure versus hydraulic diffusivity (top axis) and dimensionless frequency (bottom axis; $f_D = \frac{r_{so}^2 f}{c}$).

This represents the pressure propagation between formation and observatory. Several values of formation and instrument compressibility ratio (β_D) are shown; for a given period, hydraulic diffusivity can be estimated from a known compressibility ratio and observed phase lag and/or amplitude damping. Red stars are our observations which show 100% amplitude response of formation pressure to the reference pressure and zero phase lag, respectively (See the details in the main text). Then, we obtained a hydraulic diffusivity > 9.1×10^{-6} m^2/s for the GeniusPlug, β_D=28.9.

4.4.2. Responses to Earthquakes

4.4.2.1. Changes and Recovery of Pore Pressure and Loading Efficiency

From 70 earthquakes that met the magnitude-distance criteria 22 events produced changes either in pore pressure and/or loading efficiency. The magnitude of pressure steps ranges from 14-230 Pa (tens to hundreds of times larger than the precision of pressure measurements of ±0.7 Pa). Changes in loading efficiency range from 0.003-0.029. We detected 20 events associated with pressure steps and 17 of these are increases. In contrast, all of 13 events, changes in loading efficiency are decreases. In several cases, events resulted in only a change in pressure, and 11 of the 22 events produced changes in both pressure and loading efficiency (Table 4.3).

Global compilations document a magnitude-distance threshold for a wide range of hydrologic effects from earthquakes, including changes in groundwater level, increase in streamflow, and liquefaction (e.g., Matsumoto et al., 2003a; Wang and Manga, 2010b). Our observations follow a similar pattern, with detectable changes in both pore pressure and loading efficiency following a

systematic trend in which responses appear to be controlled by earthquake magnitude and epicentral distance (Fig. 4.9). Smaller earthquakes, or more distal larger earthquakes, do not lead to observed perturbations in either pressure or loading efficiency.

Wang et al. (2006) suggested that seismic energy density (SED), defined as the maximum seismic energy available in a unit volume to do work on rock or sediment (Wang and Manga, 2010b), is the primary factor governing the magnitude-distance threshold. They suggested that, in their global catalog of hydrologic perturbations, the thresholds for changes in groundwater level and liquefaction correspond to SED of ~10^{-3} J/m^3 and ~10^{-1} J/m^3, respectively (Fig. 4.9). Our data suggest a similar threshold applies to changes in pressure and loading efficiency along the megasplay, and that it is most similar to the threshold for changes in water levels (~10^{-3} J/m^3), whereas the SED associated with liquefaction responses in the global dataset is generally higher than that encountered at our site for most events.

The recovery of changes in both pressure and loading efficiency following earthquakes is also observed clearly, and generally exhibits a systematic increase in recovery time with increased magnitude of perturbation (Fig. 4.10). We define the recovery time as the time required after the earthquake for the value of pressure or loading efficiency to return to its prior value. The prior values of pressure and loading efficiency are defined by a 10 minute average and 3 day average, respectively. For the pressure, it is possible that the pressure perturbations produced by propagation of seismic

waves of other earthquakes temporarily exceeds the prior value. We ignored this factor and compared the trends of pressure before and after the earthquakes. Estimated step changes in pore pressure could have errors of ~20 Pa because of the variation in a 10 minute average of the prior value. Recovery of loading efficiency is generally slower than pressure recovery. For the largest change in pressure (230 Pa), recovery takes ~108 days, whereas the smallest detectable change in pressure (14 Pa) recovers in as little as 21 h (Fig. 4.10(a) and Table 4.3). In contrast, the largest changes in loading efficiency ($\Delta\gamma$=0.009-0.029) recover over times of ~27 to > 130 days, and the smallest observable changes ($\Delta\gamma$=0.003) recover in less than one day (Fig. 4.10(b) and Table 4.3). We hypothesize that the differences in recovery times for pressure and loading efficiency reflect a difference in processes. In the case of pressure, regional fluid flow re-equilibrates pressure head relatively rapidly. In contrast, recovery of loading efficiency depends on recovery of the formation's elastic properties, which is related to re-establishment of pore structure and grain contacts.

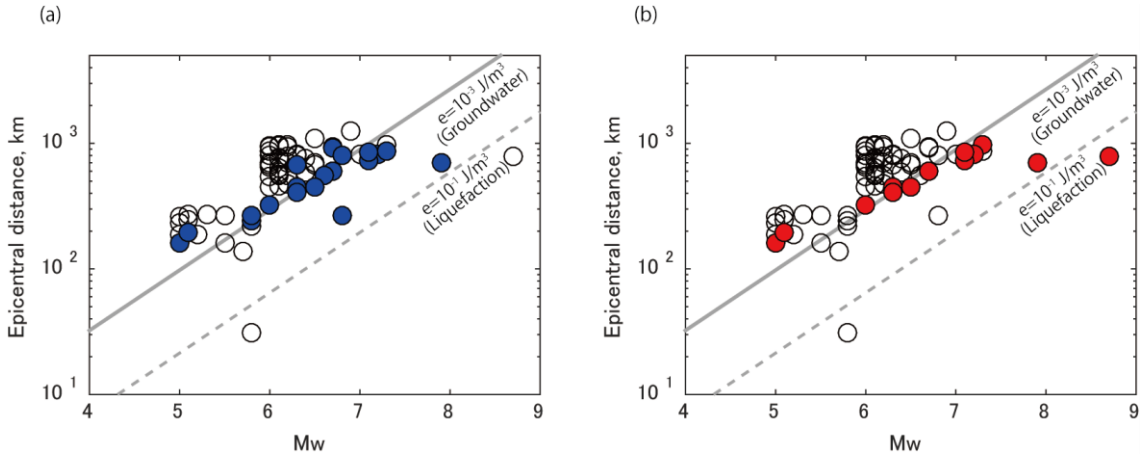

Figure 4.9. Earthquake magnitudes and epicentral distances from Site C0010. Blue and red circles show events which produce detectable changes in (a) pressure and (b) loading efficiency; open circles show events that did not produce detectable perturbations. Gray solid and dashed lines represent the thresholds for groundwater level changes and liquefaction, respectively (Wang and Manga, 2010b).

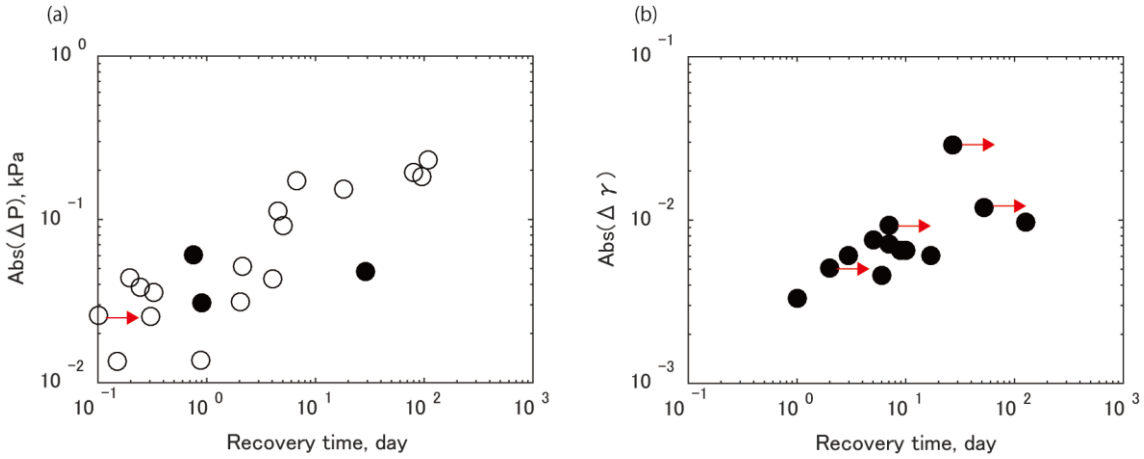

Figure 4.10. Recovery times for changes in (a) pressure and (b) loading efficiency. The open and solid circles represent increases and decreases in pressure and loading efficiency. The red allows indicate events for which subsequent large earthquakes interfered with the recovery. Consequently, only a lower bound on recovery time can be estimated (Table 4.3).

Table 4.3. Seismic events which induced changes in pressures and/or loading efficiency.

No.	Date (UTC)	Latitude (°)	Longitude (°)	Mw	Epicentral distance (km)	ΔP (kPa)	ΔP recovery time (day)	Δγ	Δγ recovery time (day)	Static volumetic strain	Theoretical ΔP (kPa)	$\int P^2 dt$ ($kPa^2 \cdot s$)	PGV (cm/s)
1	2010/11/30 3:24	28.36	139.59	6.7	606	-6.1×10^{-2}	0.75	-6.5×10^{-3}	9	4.8×10^{-11}	2.3×10^{-4}	0.54	-
2	2010/12/21 17:19	27.05	143.94	7.3	977	-	-	-7.1×10^{-3}	7	3.4×10^{-10}	-	6.65	-
3	2011/3/9 2:45	38.33	143.28	7.2	826	5.1×10^{-2}	More than 2.13	-5.1×10^{-3}	More than 2	3.8×10^{-12}	1.8×10^{-5}	1.53	-
4	2011/3/11 5:46	38.10	142.86	9.0	782	-	-	-2.9×10^{-2}	More than 27	-1.6×10^{-8}	-	629.18	-
5	2011/4/7 14:32	38.20	141.92	7.1	731	2.5×10^{-2}	0.30	-4.6×10^{-3}	6	-2.3×10^{-10}	-1.1×10^{-3}	1.54	-
6	2011/4/11 8:16	36.95	140.67	6.6	553	2.6×10^{-2}	0.10	-	-	-3.6×10^{-10}	-1.7×10^{-3}	4.10	-
7	2011/6/22 21:50	39.95	142.59	6.7	919	1.3×10^{-2}	0.15	-	-	-4.9×10^{-12}	-2.3×10^{-5}	0.12	-
8	2011/7/5 10:18	33.99	135.23	5.0	161	-3.1×10^{-2}	0.90	-6.1×10^{-3}	17	5.9×10^{-11}	2.8×10^{-4}	0.42	-
9	2011/7/24 18:51	37.71	141.63	6.3	673	1.4×10^{-2}	0.89	-	-	1.0×10^{-12}	4.7×10^{-6}	0.03	-
10	2011/8/1 14:58	34.71	138.55	5.8	241	3.6×10^{-2}	0.33	-	-	1.1×10^{-10}	5.0×10^{-4}	4.55	-
11	2011/8/19 5:36	37.65	141.80	6.3	679	3.8×10^{-2}	0.24	-	-	-2.8×10^{-12}	-1.3×10^{-5}	0.18	-
12	2011/10/25 19:34	32.18	138.38	5.1	196	-4.8×10^{-2}	28.93	-6.5×10^{-3}	10	2.5×10^{-12}	1.2×10^{-5}	0.74	-
13	2012/1/1 5:27	31.43	138.57	6.8	265	4.3×10^{-2}	4.08	-	-	1.1×10^{-9}	5.0×10^{-3}	3.34	-
14	2012/12/7 8:18	37.82	144.32	7.3	862	1.9×10^{-1}	80.11	-	-	-5.9×10^{-12}	-2.8×10^{-5}	15.54	-
15	2013/4/17 8:57	34.05	139.35	5.8	265	4.4×10^{-2}	0.19	-	-	-2.0×10^{-10}	-9.5×10^{-4}	0.58	-
16	2013/9/4 0:18	29.94	139.42	6.5	446	1.1×10^{-1}	4.55	-3.3×10^{-3}	1	3.7×10^{-11}	1.7×10^{-4}	0.38	-
17	2013/10/25 17:10	37.20	144.57	7.1	845	1.7×10^{-1}	6.71	-6.1×10^{-3}	3	-2.5×10^{-10}	-1.2×10^{-3}	3.56	-
18	2014/3/13 17:06	33.69	131.89	6.3	449	1.5×10^{-1}	18.30	-1.2×10^{-2}	More than 52	6.5×10^{-12}	3.1×10^{-5}	9.99	-
19	2014/5/4 20:18	34.94	139.50	6.0	324	9.2×10^{-2}	5.07	-7.6×10^{-3}	5	7.2×10^{-11}	3.4×10^{-4}	0.10	-
20	2014/11/22 13:08	36.69	137.89	6.3	404	2.3×10^{-1}	107.58	-9.3×10^{-3}	More than 7	-3.8×10^{-11}	-1.8×10^{-4}	1.55	0.19
21	2015/5/12 21:12	38.86	142.15	6.8	800	3.1×10^{-2}	2.03	-	-	-1.2×10^{-11}	-5.4×10^{-5}	0.13	0.07
22	2015/5/30 11:23	27.86	140.68	7.9	707	1.8×10^{-1}	96.13	-9.7×10^{-3}	128	1.1×10^{-9}	5.1×10^{-3}	84.19	0.27

4.4.2.2. Relationship of Perturbations to Static and Dynamic strains

To investigate potential mechanisms for the observed perturbations in pore pressure and loading efficiency, we evaluate the static and dynamic strains expected for the earthquakes listed in Table 4.3. We estimate the static volumetric strain theoretically, based on solutions of Okada (1992) and the focal mechanisms reported by F-net (the National Research Institute for Earth Science and Disaster Prevention).

Dynamic strain is often determined by using peak ground velocity (PGV); however, we were unable to use local seismic data from nearby instruments in the seafloor DONET observatory (Dense Oceanfloor Network system for Earthquakes and Tsunamis) because seismic data are only available for small portion of our study period (after October in 2014). Then, from a proportional relationship of pore pressure and strain at an undrained condition, we estimated integrated square pressure amplitude "$\int p^2\ dt$ " for each event over a 30 minute window of the pressure records, which provides a proxy for the integrated square dynamic strain. According to a relationship between pressure and strain under undrained conditions ($p = -BK_u\Delta\varepsilon$), pore pressure could be proportional to strain change in the high frequency range (Roeloffs, 1996). To verify the utility of $\int p^2\ dt$ as a proxy for dynamic strain energy in light of the low pressure sampling rate, we assess the relationship between $\int p^2\ dt$ and PGV for events during the time interval when DONET data are available at the closet ocean bottom seismometer (OBS) (Site KMD 13, located 1.2 km to the Northeast of Hole C0010A). PGV was

defined from the OBS record by filtering for frequencies of 0.1 – 10Hz. We document a clear correlation between PGV and $\int p^2\ dt$ (Fig. 4.11) indicating that $\int p^2\ dt$ provides a viable proxy for dynamic strain. We note that the $\int p^2\ dt$ likely underestimates the strain energy because the 30 s sampling interval does not allow detection of energy at frequencies > ~0.016 Hz.

Fig.4.12 shows the relationship between changes in pressure and loading efficiency, and predicted static strains and $\int p^2\ dt$ (as a proxy for dynamic strains), respectively. We find that there is a clear trend in which larger $\int p^2\ dt$ produces larger changes in both pressure and loading efficiency (Fig. 4.12(b), (d)), whereas any correlation between expected static volumetric strain and the observed hydrological perturbations is less clear (Fig. 4.12(a), (c)).

To further investigate the possible role of static strain in driving the hydrological changes, we compute the expected pore pressure response to the predicted static volumetric strain for each earthquake shown in Fig. 4.13. We assume a conversion factor of 4.7 kPa μstrain^{-1}, as reported by Wallace et al. (2016) and Araki et al. (2017), and based on the formulation of Wang (2004). This conversion factor is in excellent agreement with the observed pressure changes associated with a well-constrained Mw 6.0 earthquake nearby, which provides a "field calibration" of the formation response (Wallace et al., 2016). Our analysis demonstrates that the predicted changes in pressure are tens to hundreds of times smaller than those observed (Fig. 4.13). This difference cannot be explained by local trends of pressure or instrument drift, and suggests that static strains are unlikely to be a factor

in causing the pressure changes.

On the basis of the stronger correlation between dynamic strain (or with $\int p^2 \, dt$ as a proxy) and perturbations in both pressure and loading efficiency, together with the lack of evidence for static strains as a cause of the pressure steps, we interpret the hydrological effects we observe to reflect responses to dynamic strain (e.g., Hammerschmidt et al., 2013a). In fact, the change in pressure started during the seismic wave passage, which was confirmed using the available DONET data (Fig. 4.14). This interpretation is also consistent with global observations indicating that dynamic strain is a primary driver for triggering of earthquakes and mud volcano eruptions, and to changes in groundwater level (e.g., Kilb et al, 2000; Kitagawa et al., 2006; Manga and Wang, 2007).

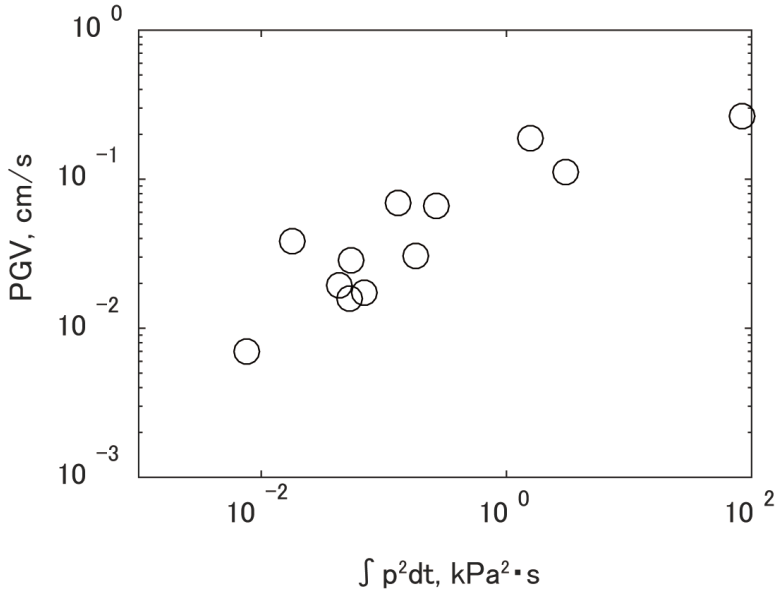

Figure 4.11. Assessment of relationship between $\int p^2\ dt$ and PGV (peak ground velocity). $\int p^2\ dt$ and PGV were estimated for the earthquakes listed in Table 4.4, from the time period when DONET ocean bottom seismometer (OBS) data were available.

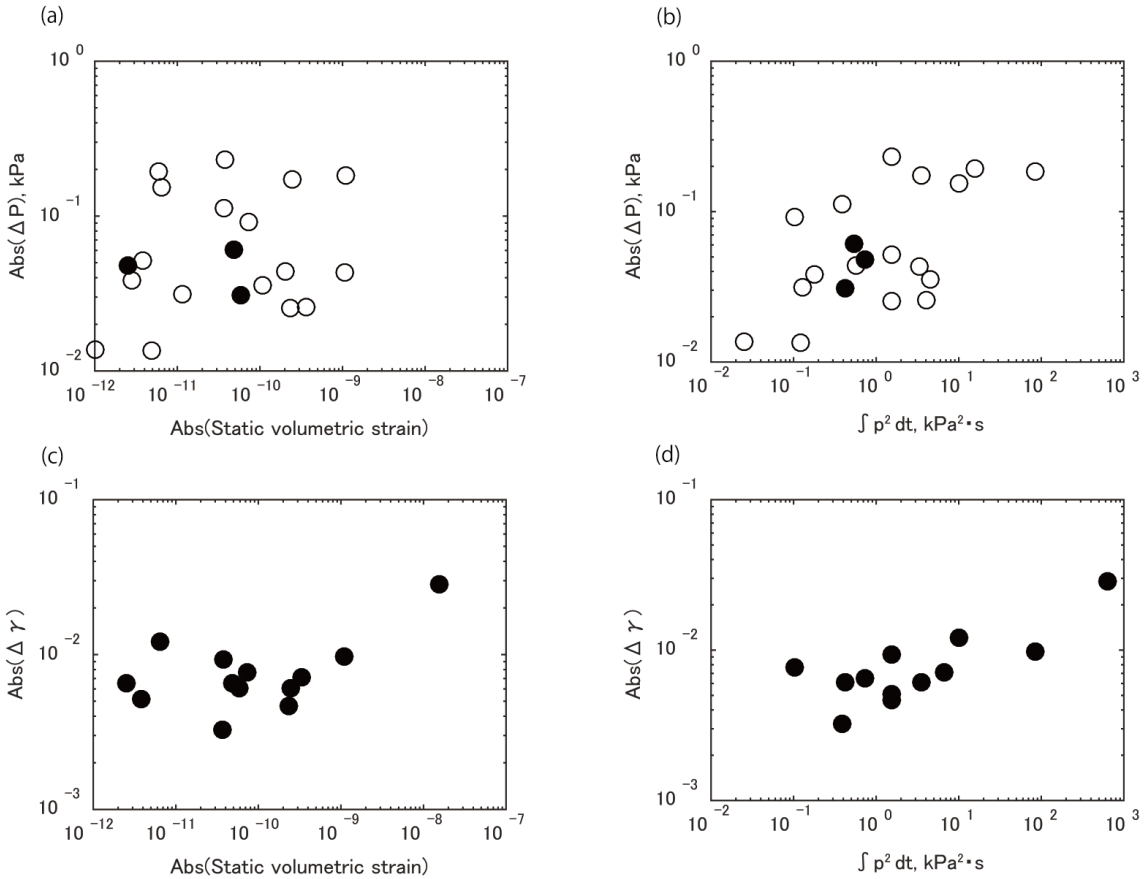

Figure 4.12. Relationship between hydrologic perturbations and static and dynamic strains. Panels (a) and (b) show changes in pore pressure versus (a) theoretical static volumetric strain and (b) $\int p^2 \, dt$. Panels (c) and (d) show changes in loading efficiency versus (c) theoretical static volumetric strain and (d) $\int p^2 \, dt$. Open and solid circles represent increases and decreases in pressure or loading efficiency, respectively.

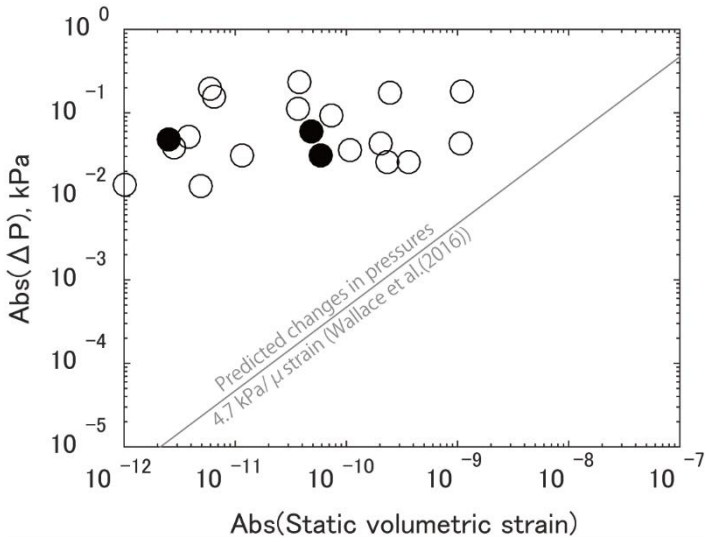

Figure 4.13. Comparison of observed changes in pressure (symbols; open = pressure increases; solid = pressure decreases), and predicted pressure changes (gray line) on the basis of calculated static strains for each earthquake listed in Table 4.3.

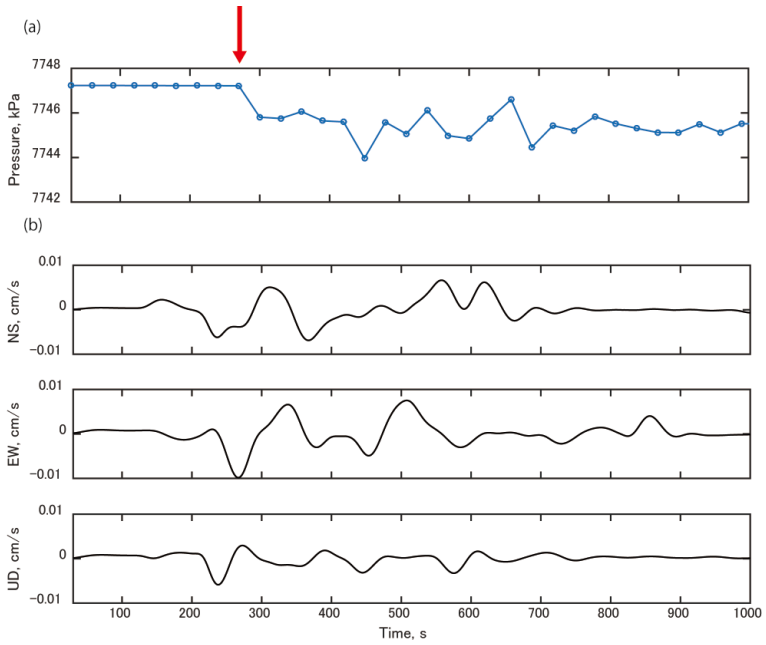

Figure 4.14. Timing of pressure change during seismic wave passage. (a) Pressure change at the time of the earthquake occurred on May 30, 2015 (Table 4.3). Ground velocity records of (b) NS, (c) EW and (d) UD components, respectively after low-pass filters (cut-off frequencies of 0.017 Hz). Origin

of the x-axis represents the time of occurrence of the earthquake and the red arrow indicates the initial change in pressure.

Table 4.4. Seismic events used for the comparison between $\int p^2 \, dt$ and PGV in Fig. 4.11.

No.	Date (UTC)	Latitude (°)	Longitude (°)	Mw	Epicentral distance (km)	$\int P^2 dt$ ($kPa^2 \cdot s$)	PGV (cm/s)
1	22/11/2014	36.69	137.89	6.3	404	1.5E+00	1.9E-01
2	16/02/2015	39.87	143.19	6.7	944	2.7E-01	6.7E-02
3	20/02/2015	39.91	143.73	6.1	978	4.3E-02	2.0E-02
4	25/02/2015	31.09	142.14	6.1	565	5.3E-02	1.6E-02
5	10/05/2015	31.23	142.15	6.1	559	1.8E-01	3.0E-02
6	12/05/2015	38.86	142.15	6.8	800	1.3E-01	6.9E-02
7	30/05/2015	27.86	140.68	7.9	707	8.4E+01	2.7E-01
8	23/06/2015	27.70	140.18	6.5	697	1.8E-02	3.8E-02
9	01/09/2015	31.47	142.14	6.0	549	7.0E-02	1.7E-02
10	13/11/2015	30.94	128.59	6.8	804	3.0E+00	1.1E-01
11	11/01/2016	44.43	141.21	6.3	1312	7.5E-03	7.0E-03
12	14/01/2016	41.97	142.80	6.7	1116	5.4E-02	2.8E-02

4.4.2.3. Mechanisms for Changes in Pressure and Loading Efficiency

In almost all cases, the perturbations we document represent increases in pressure and decreases in loading efficiency. Many, but not all, of these occur in response to the same earthquakes (Table 4.3). We suggest two potential mechanisms to explain these observations (Fig. 4.15). The first is disaggregation of sediment particles leading to partial liquefaction, which is well known as a response of unconsolidated sediments and soils to earthquake-induced shaking (e.g., Finn, 1981; Ishihara, 1985). Shaking-induced collapse of pore spaces or closure of fractures would drive both an increase in pore

pressure and an increase in formation stiffness (leading to a decrease in loading efficiency; c.f., Eq. (4.2a)). An increase in stiffness of ~13-15 % would be required to explain the observed changes in γ. In this scenario, the recovery of loading efficiency and pore pressure could be explained by time-dependent softening (i.e., via grain boundary sliding) of the formation, and pressure diffusion, respectively. This mechanism for increased pore pressure and decreased loading efficiency is broadly consistent with a wide range of observed hydrologic perturbations induced by earthquakes, in which ground shaking is invoked as a primary cause of fracture and soil structures reorganization or damage (Manga and Wang, 2007).

A second potential mechanism is the exsolution of dissolved gas in response to shaking. In this scenario, interstitial water contains dissolved gas, and as seismic waves pass, the gas exsolves. Because the compressibility of free gas is much larger than that of dissolved gas, this phenomenon would produce decreases in loading efficiency (c.f., Eqs. (4.2a) and (4.3)). In this case, an increase in compressibility of the gas-water mixture (β_{w+g}) by ~15 % (corresponding to an increase from ~0.5 % to ~1 % by volume of free gas) would be required to explain the observed changes in γ. In terms of the difference of recovery time in pressure and loading efficiency, the initial pressure decrease for inducing gas exsolution is not produced by compression and extension of rock mass associated with seismic waves. Exsoluted gas should be re-dissolved into fluid immediately in this case. We infer that the hydraulic condition was shifted from undrained to drain induced by formation of fracture such as

unclogging. Pressure in the rock mass is released and gas bubbles are generated simultaneously. Strong exsolution and expansion of gas would exceed leakage of pressure and it results in increase in pressure. Pressure diffusion is fast, which leads to a rapid recovery of pressure through fracture than loading efficiency. In contrast, the recovery of loading efficiency is related to escape of bubbles from the rock mass because of changing buoyancy. Unclogging of sediments is also a possible mechanism to re-produce an undrained condition, which may enhance pore pressure in the rock mass and force gases re-dissolve into fluid. Given the observation of abundant gas bubbles in the GeniusPlug fluid sampling coils upon recovery (Saffer et al., 2017), we suggest that the mechanism relating to gas bubbles is more plausible than first model. In the first model for disaggregation of sediment particles, there has been no evidence for "time-dependent softening" of the formation which is required to explain the recovery of loading efficiency. In contrast, the second model can explain not only observed hydrological perturbations produced by earthquakes but also damping of loading efficiency, $\gamma = 0.74$ (as discussed in Section 4.4.1).

Three observed pressure steps were decreases (Table 4.3), which suggests that pressure release from the fracture exceeds pressure increase by gas exsolution. It is also possible that the coarse sampling rate obscures small pressure increase. Nine events (Table 4.3) changed only pressure but not loading efficiency, which is often observed at the onshore boreholes (e.g.., Koizumi and Kinoshita, 2017). One possible cause of this is the difference of scale between the observed pressure and the tidal

response of pressure. The wave length of Earth tide is larger than that of seismic waves. Then, observations of changes in pressure without any anomaly of tidal response suggest that these hydrological perturbations occurred in a smaller local region.

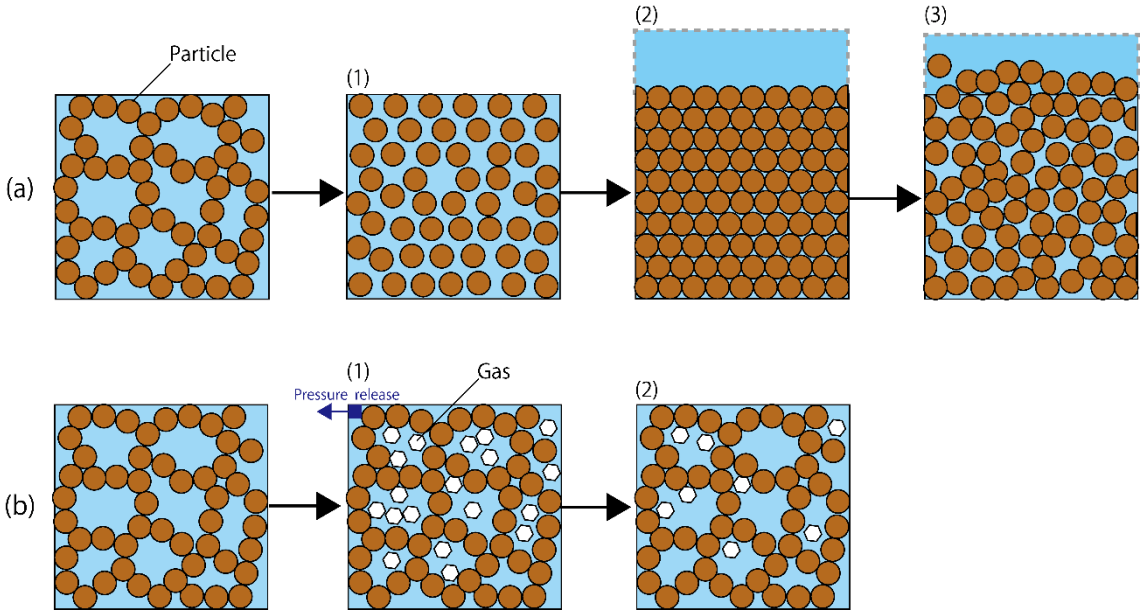

Figure 4.15. Schematic of two potential mechanisms explaining the suite of observations. Earthquake shaking could lead to either (a) disaggregation of sediment particles or (b) exsolution of dissolved gas in interstitial water. Both mechanisms can explain increases in pressure, decreases in loading efficiency, and recovery of both quantities. In (a), (1) disaggregation of particles by ground shaking, (2) collapse of pore spaces or closure of fractures. Fluid goes out upward and rock mass in part of original size becomes stiffer. (3) time-dependent softening of formation and pressure diffusion. In (b), interstitial water originally contains dissolved gas. (1) seismic wave breaks undrained rock mass and gas exsolves from the interstitial water associated with pressure leakage. (2) Recoveries of pressure and loading efficiency are related to time-dependent diffusion of gas bubbles or re-dissolution into interstitial water by healing of damaged parts.

4.5. Summary

We investigated a timeseries of pore pressure monitored continuously within a major fault zone in the active Nankai Trough accretionary complex. Our analysis shows that the pressure record provides a highly sensitive measure of hydrological perturbations associated with earthquakes, and reveals several small but detectable changes in both formation pore fluid pressure and poroelastic properties.

One key observation is that there is essentially no phase lag in formation pressure relative to the seafloor reference pressure, yet the amplitude of the pressure response in the observatory is damped by a factor of ~0.74. This can be explained by a combination of rapid fluid pressure diffusion between the formation and the borehole (suggesting high hydraulic diffusivity), and a small amount of dissolved gas in the interstitial waters, that increases the compressibility of pore fluids and thus decreases the formation loading efficiency. This explanation differs somewhat from previous interpretations of the pressure response (e.g., Hammerschmidt et al., 2013a, b), which attributed both effects to limited fluid mass transport between the formation and borehole (e.g., Sawyer et al., 2008) but were not able to reconcile the clear amplitude damping and lack of any phase lag. On the basis of our interpretation, we find a lower bound on formation (fault zone) hydraulic diffusivity of 9.1×10^{-6} m^2/s (corresponding to a permeability > 6.4×10^{-13} m^2), broadly consistent with other reported fault zone permeabilities in subduction zones (e.g., Saffer, 2015).

The responses to earthquakes, in almost all cases, are manifested as increases in pore pressure and

decreases in loading efficiency. Detectable changes of both quantities follow a systematic trend that larger earthquakes, or those with closer epicenters, produce larger changes of both pressure and loading efficiency. The magnitude-distance threshold for the perturbations we report is similar to the threshold for changes in water levels in global compilations from primarily onshore observations (10^{-3} J/m^3; Wang and Manga, 2010b).

A comparison between expected static volumetric strain and pressure energy density reveals that dynamic strain is likely the primary driver of the observed changes. On the basis of our results, we suggest two potential mechanisms to explain the perturbations and subsequent recoveries: (1) shaking-induced reorganization of sediment structure that leads to pore pressure increase and modest stiffening of the substrate; or (2) exsolution of gas that drives both a small pressure increase and an increased fluid phase compressibility. The latter is most consistent with observations of gas in the pore fluids at the same depth as the pressure monitoring interval.

Our study demonstrates the value of borehole monitoring as a highly sensitive and continuous measurement of formation physical properties, which provides new insights into the hydrological behavior of an active fault zone along a subduction plate boundary.

Chapter 5. Estimation of Hydraulic Diffusivity from Pore Pressure Response to the Ocean Drilling in the Nankai Subduction Zone

5.1. Introduction

In situ hydraulic properties such as diffusivity and permeability are important for a wide range of geological and geomechanical processes in subduction zones. In particular, they have important effects on many activities in the Earth's crust, such as heat transport, chemical transport, supporting biological communities, fluid and mass fluxes, and the control of pore pressure on mechanical processes. Also these fluids properties affect both the long-term strength of the crust and faults (and in situ stress state), as well as earthquake behavior (e.g., Screaton et al., 1990; Kato et al., 2003; Spinelli and Wang, 2008; Saffer and Tobin, 2011). Despite this importance to such a broad suite of key processes, in situ permeability, especially, at relevant scales of tens to several hundreds of meters, is generally not well constrained. This is a particularly important issue in active tectonics settings where pervasive faulting and fracturing likely lead to scale dependence.

Much of existing constraint on formation hydraulic properties in subduction zone comes from laboratory measurements on intact core samples, or from inverse modeling that yields constraints on the large scale permeability, such as tens of meter to kilometers, required to maintain inferred pore pressures or to allow transport of heat or chemical signals (e.g., Fisher and Hounslow, 1990; Ikari and

Saffer, 2012; Lauer and Saffer, 2012). In a few cases, cross-hole or single well tests have been used to estimate permeability using responses to perturbations in pressure (Screaton et al., 2000; Fisher et al., 2008). At the Nojima fault in western Japan, which ruptured during the 1995 Kobe earthquake (Mw 7.3), water injection tests have been performed every few years and an observed decrease in permeability is considered to be relate to the healing process of the fault zone (Kitagawa and Kano et al., 2016). Although water injections for the purpose of energy development such as investigation of reservoir capacity, is performed onshore, there are few reports of in situ measurements of hydraulic properties offshore for understanding of geotectonic processes.

Here, we use a set of inadvertent cross-hole perturbation tests to define formation-scale (~100 m scale) hydraulic diffusivity and permeability within the accretionary prism and Kumano basin in the Nankai subduction zone. We evaluate the response of pore pressure in a sealed observatory borehole to drilling at two nearby wells. We use a 2-D numerical model, and define best-fit hydraulic parameters using a grid search approach. We then compare our result with previous measurement of permeability at the core scale and single hole, then discuss the implications for the scale-dependence of permeability.

5.2. Geological Setting and Borehole Observatory (LTBMS: Long-Term Borehole Monitoring System)

A permanent observatory, LTBMS (Long-Term Borehole Monitoring System) was installed during

IODP Expedition 332 in 2010 at Hole C0002G. This borehole is located in the southeastern part of the Kumano Basin and penetrated Pleistocene and Quaternary basin-filling sediments, and the uppermost accretionary prism to a total depth of 980 meters below sea floor (mbsf) (Fig. 5.1(a)). The LTBMS is a comprehensive observation system, including four pressure monitoring ports, a broadband seismometer, accelerometers, geophones, a tiltmeter, a volumetric strainmeter, and a thermistor string (Expedition 332 Scientists, 2011b). The data are transmitted through a submarine cable network; DONET, and which enables access to real time data. The four pressure ports include three installed at different sub-seafloor depth (ports P1, P2, and P3, numbered from deepest to shallowest). The port at the seafloor (P4) that provides an oceanographic reference and allows removal of tidal and other oceanographic signals to assess pore pressure variations in the formation (e.g., Davis et al., 2009; Araki et al., 2017) (Fig. 5.2). The resolution of Paroscientific Digiquartz pressure transducers are within ~10 parts per billion of full-scale pressure, or ~0.7 Pa (Expedition 332 Scientists, 2011b) and the sampling interval was one minute from 2010 to 2012, then, changed to one second in 2012. The Paroscientific gauges are also used for the temporary observatory, SmartPlug and GeniusPlug installed at Site C0010 and the accuracy of the instruments was verified with calibration tests (See Chapter 4; Expedition 332, Scientists, 2011b; Hammerschmidt et al., 2013b). We focus on the pressure records in the deepest (P1) and shallowest (P3) pressure ports, which were installed to monitor pressure in the upper accretionary prism, which is composed of Miocene silt, mud and sand, and the Kumano basin

which is composed of Quaternary silt turbidites and hemipelagic mud (Table 5.1; Expedition 315 Scientists, 2009). The open holes are provided at 937-980 mbsf and 757-780 mbsf, respectively. Bedding dip of the accretionary prism is ~30-60°, in contrast, the forearc basin has a relatively low angle dip $\leq$ 15°. Pore pressures at all monitoring intervals in Hole C0002G are near-hydrostatic; this is also consistent with downhole pressure measurements at Site C0009A located about 20 km landward (Saffer et al., 2013), and with predictions from models that simulate coupled sedimentation loading and pore pressure development (e.g., Guo et al., 2011).

P2 pressure port was installed within the cemented section to monitor the coupling between observatory and formation, and we don't use the P2 record in this study (Fig. 5.2).

5.3. Observed Pressure Response to Nearby Drilling Operations

The pressure records from the observatory in C0002G were analyzed to study the response formation pressure to drilling and coring operations in two nearby boreholes (C0002H and C0002I) located about 100 m to the southwest (Fig. 5.1(b)). After removal of the effects of tidal loading using the reference pressure (P4) (See Chapter 4; Eq. (4.1)), the P1 and P3 pressure data show clear responses to the drilling operations. The P1 record increased gradually, with onsets corresponding to the times that the drillbit reached the accretionary prism in each of the adjacent boreholes (Fig. 5.3). The P3

record also increased responding to the drilling, however the onset is delayed from the time that the drillbit reached the depth corresponding to P3.

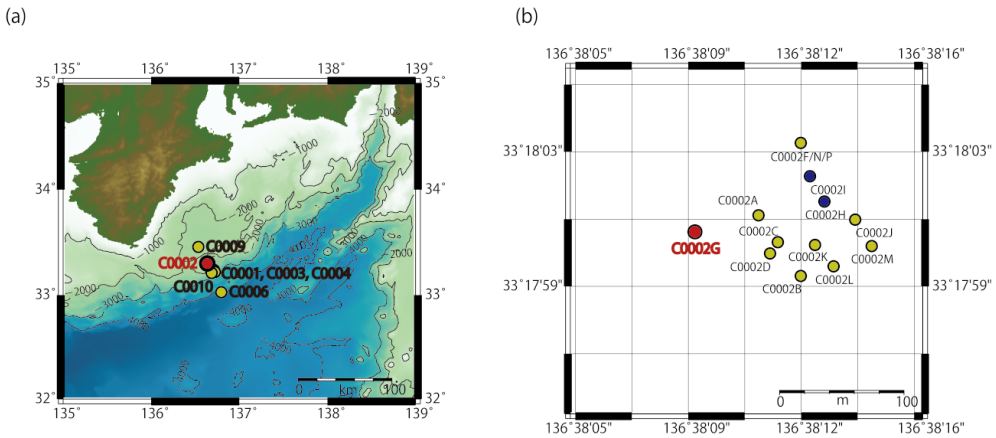

Figure 5.1. Location of NanTroSEIZE drillsites. (a) Map of the drilling sites (circle). Borehole observatories (LTBMS: Long Term Borehole Monitoring System) were installed at Sites C0002 and C00010, and we use the data of Site C0002 (red circle). (b) The detailed map of Site C0002 (circles show the location of each borehole). LTBMS is located at Hole C0002G (red circle) and its pressure records responded to the drilling and coring operation at Hole C0002H and C0002I (blue circles) which are located 104 m and 99 m from Hole C0002G, respectively.

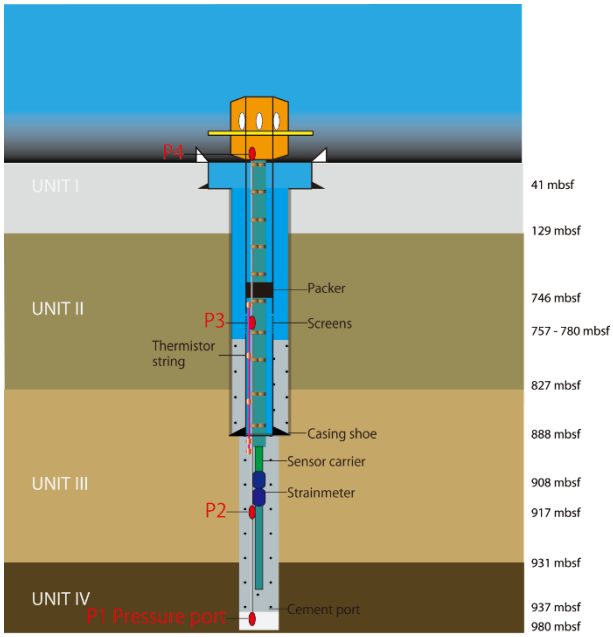

Figure 5.2. Diagram of the LTBMS observatory at Hole C0002G (Modified from Expedition 332 Scientists, 2011d).

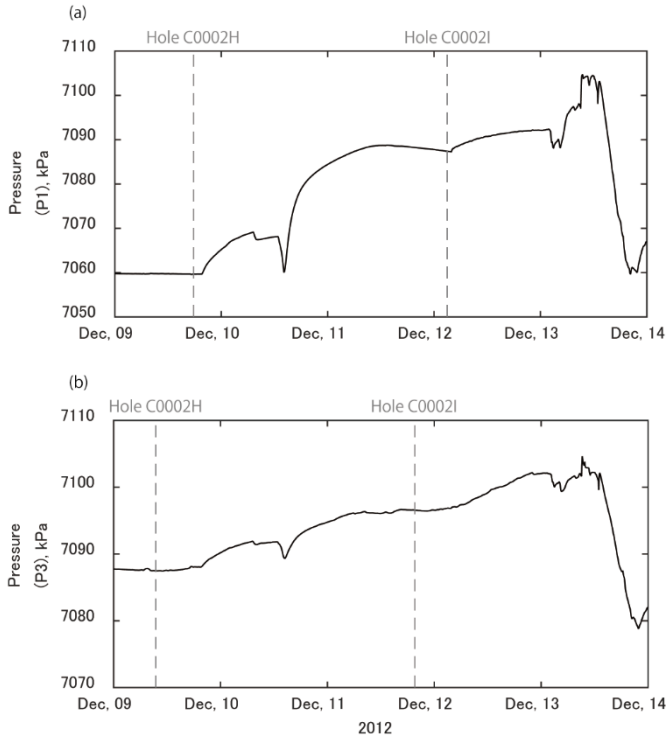

Figure 5.3. Time series of pressure records of (a) P1 and (b) P3 in Hole C0002G during the drilling operations. Gray dashed lines show the times that the drillbit in Holes C0002 H and C0002I reaches the depths corresponding to P1 (937 mbsf) and P3 (757 mbsf) pressure ports.

Table 5.1. Lithologies of Site C0002.

Site	C0002
Water depth, m	1936 m
Unit	Structural geology
Unit I (0-135.5 mbsf)	Quaternary upper forearc basin Sandy/silty mud
Unit II (135.5-830.4 mbsf)	Lower forearc basin Sandy/silty Turbidites and hemipelagic mud
Unit III (830.4-935.6 mbsf)	Basal forearc basin Hemipelagic mud
Unit IV (935.6-1400 mbsf)	Accretionary prism Sandy/silty turbidite sequences

5.4. Modeling Methods

The consistent responses of pressure in the observatory at Hole C0002G to drilling at nearby holes provides an opportunity to estimate in situ formation hydraulic properties. The amplitude of elastic wave produced by vibrations from the drilling is quite small since there is no difference in seismic noise levels of pressure observed by LTBMS before and during the drilling. These very small amplitudes should have no significant effect on the fluid structure. Here, we assume that the perturbations in pressure result from lateral diffusion of pressure from the active wells during drilling operations, and thus represent a set of inadvertent cross-hole experiments (e.g., Screaton, et al., 2000).

To assess formation hydraulic properties, we developed a 2-D transient numerical model of fluid pressure diffusion in the horizontal plane. Pressure diffusion is described in two dimensions by;

$$\frac{\partial p}{\partial t} = c\left(\frac{\partial^2 p}{\partial x^2} + \frac{\partial^2 p}{\partial y^2}\right) \tag{5.1}$$

where p is fluid pressure and c is hydraulic diffusivity.

Our model domain extends for 2 km × 2 km, with a grid size of 5 m. For our first-order analysis, and in the absence of clear evidence to suggest otherwise, we specify, that the aquifer is isotropic, and homogeneous. We assume that pore pressures are initially hydrostatic at P1 and P3, which are at depths of 28.6 and 26.6 MPa, respectively, on the basis of regional observations at Sites C0002 and C0009, and the results of sedimentation loading models (Guo et al., 2011; Saffer et al., 2013). We calculated the change in pressure expected in Hole C0002G associated only with drilling, and then added the expected hydrostatic pressure for the depths of P1 and P3 for understanding of site condition.

We assumed that lateral diffusion of fluid at the drilled boreholes initiate at the time the drillbit reaches the depths corresponding to the depths of the P1 and P3 pressure ports. For the calculation of Eq. (5.1), we used a finite difference method. The time step of the calculation is every 60s.

In the case of riserless drilling, as was conducted at Holes C0002H and C0002I (the “source” wells), seawater is circulated during drilling operation to clear cuttings from the hole. The circulated

fluid and cuttings flows through the inner bore of the drill pipe, through the bit, and then returns upward in the annulus of the hole to the seafloor. The pressure at the bit exceeds hydrostatic pressure due to the combined effects of the cutting load, which increases the fluid density in the annulus, and dynamic pressure during active circulation. Therefore, we represent the source wells using a pressure boundary condition, rather treating them as injection well (Screaton et al., 2000).

During operations at Holes C0002H and C0002I, pressure at the bit was not measured directly. Because the downhole pressure in the source well is not known, we conduct a grid search to find values of both the hydraulic diffusivity and injection pressure that minimize the misfit between model predictions and observed pressures at the observatory. We searched for values of hydraulic diffusivity and injection pressure in increments of 0.01 m^2/s, 2.0 kPa, respectively, and define best fitting parameters on the basis of the root mean square (rms) error between model and observed pressure at Hole C0002G.

Formation permeabilities can be calculated from the values of obtained hydraulic diffusivities by Eqs. (4.23) and (4.24). The formation compressibility estimated from CRSC (Constant Rate-of-Strain Consolidation) tests for core samples with fluid viscosity of 10^{-3} Pa · s derived a specific storage of 5.0×10^{-5} m^{-1} (See Section 4.4.1.; Table 5.2; Guo et al., 2011). The value of specific storage ignores the dissolved gases which has a small effect on estimates of permeability. We assume a constant specific storage because variations of hydraulic diffusivity are more sensitive and variable than that of

specific storage (Xue et al., 2013).

5.5. Results

We estimated the hydraulic diffusivity using pore pressure data of Hole C0002G responding to the drilling of Holes C0002H and C0002I. These values are representative for the average flow on a scale of about 100 m. Although we constrained diffusion direction as horizontally, the trajectories of model prediction correspond well with observed pressure (Fig. 5.4). Analyses of the P1 records resulted in estimates of the hydraulic diffusivity of 0.21 and 0.41 m^2/s for Holes C0002H and C0002I, respectively. On the other hand, the estimates of hydraulic diffusivity from the P3 records were 0.03 and 0.04 m^2/s, which are ten times smaller than values from the P1 records.

For the evaluation of estimated injection pressure of 26-146 kPa, we reviewed the drilling parameters of NanTroSEIZE Expedition 314 in 2007. During this expedition, logging while drilling (LWD) was conducted at Hole C0002A (Fig. 5.2(b)) and annular pressure in the drilled borehole was measured. Observed annular pressure is ~30 MPa at 1000 mbsf corresponding to overburden pressure and the drilling disturbances which the larger density of injected specific fluid than seawater may produce them. The fluctuations of annular pressure produced by injection are within 500 kPa which suggests that our estimation of 26-146 kPa is within a reasonable range because injection pressure for the drilling is not constant during the operations.

For the sensitivity of the trade-off between hydraulic diffusivity and injection pressure, we investigated the combinations in terms of the fit to the observed data (Fig. 5.5). The stars indicate best fit values but it is possible that there are other possible solutions. Therefore, our results show one of solutions which can fit well the observed pressure perturbations.

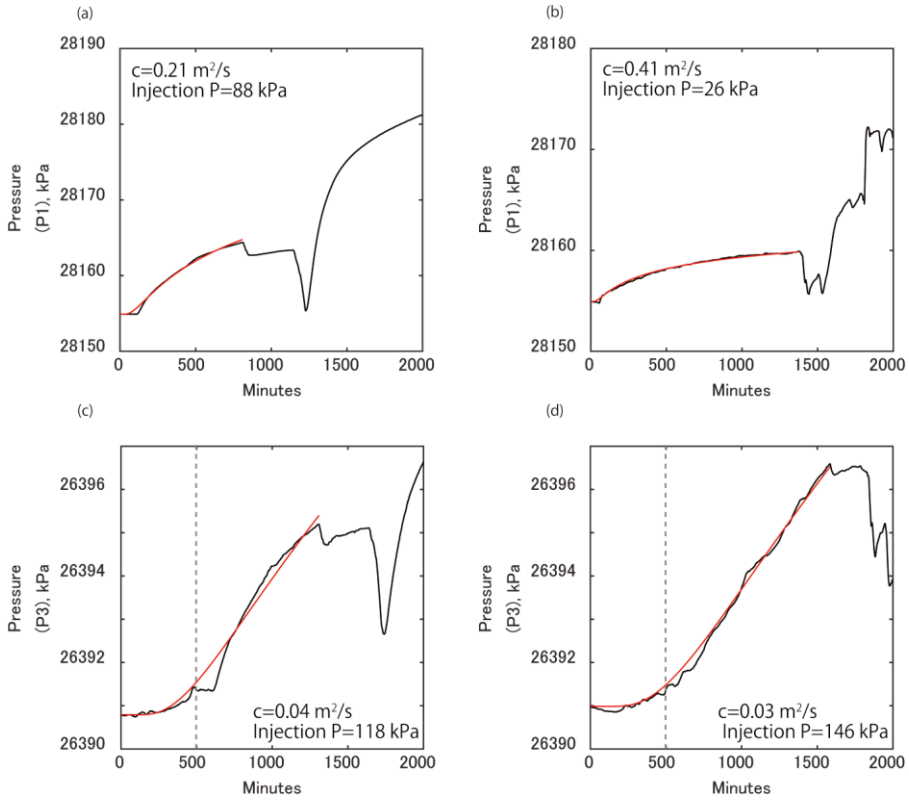

Figure 5.4. Comparison between simulated (red lines) and observed (black lines) pressure perturbations. The P1 records of drilling in Holes C0002H (a) and C0002I (b). The P3 records of drilling in Holes C0002H (c) and C0002I (d). Horizontal diffusion is started when the drillbit reaches depths corresponding to P1 and P3. Origin of the x-axis represents the time that the drillbit reaches the depth corresponding to pressure port depth. The dashed gray lines in panels (c) and (d) indicate the time that the drillbit reaches the depth corresponding to P1. Estimated hydraulic diffusivity (c) and injection pressure (Injection P) are also shown.

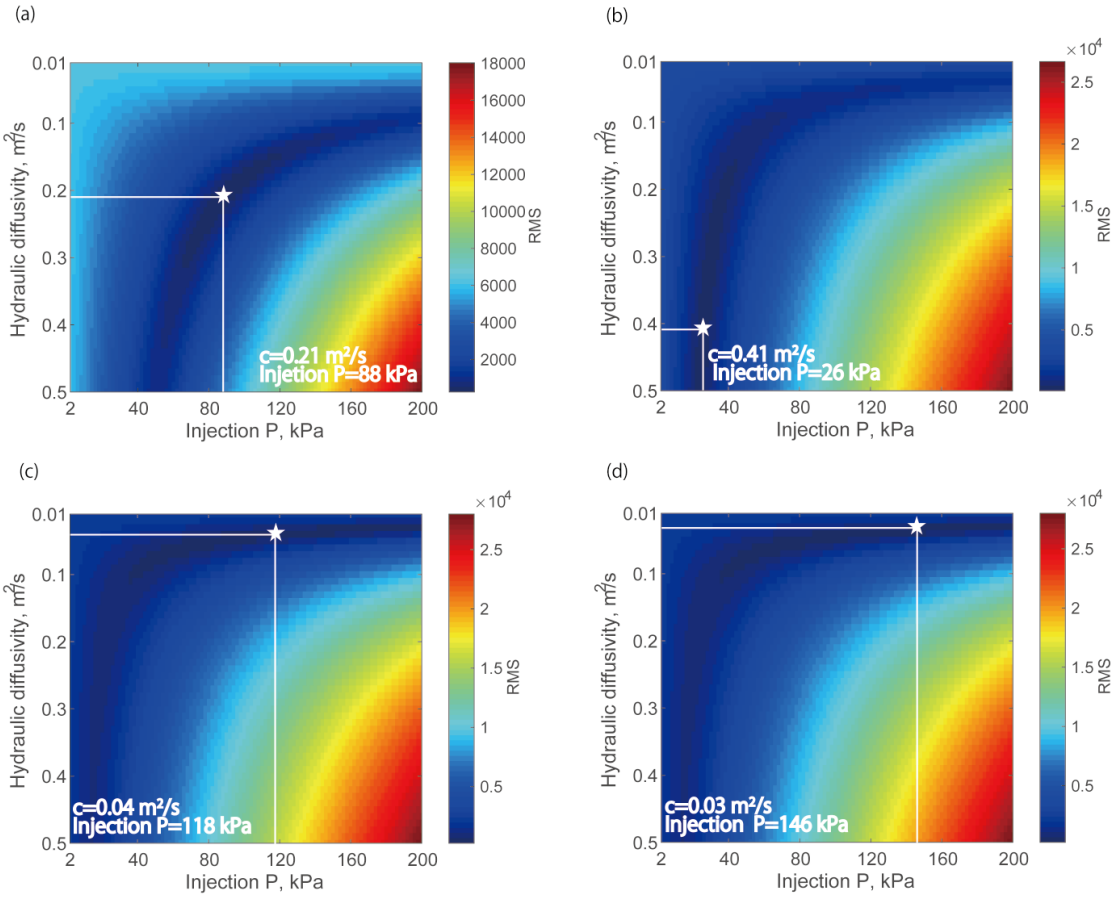

Figure 5.5. Contour plots of rms fit to the observed data for possible values of hydraulic diffusivity and injection pressure. P1 results for drilling in Holes C0002H (a), C0002I (b) and P3 results for drilling in Holes C0002H (c), C0002I (d). White stars represent the best combination of hydraulic diffusivity (c) and injection pressure for which the model can fit well the observed pressure perturbations.

5.6. Discussions

5.6.1. Potential Hydrological Perturbation Surrounding Hole C0002G

From the results of our modeling and parameter search, the P1 records can be simulated well with the assumed perturbation of pressure. On the other hand, small fluctuations in the observed records of

P3 do not fit the modeling very well (Fig. 5.4). In particular, the behavior of P3 records shows a mismatch at the time that drillbit reached the depth corresponding to P1, which may suggest the effect of vertical flow. It may be possible that the similarity between the P1 and P3 records after 500 s (Fig. 5.4(a), (c)) was produced by fluid invasion to the P3 depth in region between the source and observatory borehole. The depth of P1 is over 200 m more than P3, which is greater than the horizontal distances between the observatory at C0002G and Holes C0002H and C0002I. We observe that the horizontal permeability at the P3 depth is smaller than that of the P1 depth. And we speculate that the vertical permeability surrounding Hole C0002G is much larger than horizontal permeabilities. Drilling of boreholes can cause significant disturbances to the surrounding formation, which can produce high vertical permeability. We suggest that horizontal diffusion causes fluids to arrive at the P1 depth of Hole C0002G prior to the arrival at the P3 depth, and then vertical flow carries the fluid from the P1 depth to the P3 depth. Indeed, estimated horizontal hydraulic diffusivity at the P1 depth is 10 times larger than that of P3 depth. In other words, fluids at the P1 depth arrive at Hole C0002G 10 times faster than for the P3 depth. This pattern of flow considers only strictly horizontal and vertical flow. Actually paths of fluid flow are likely more complicated and need to be clarified with additional information about injection pressure and the detailed local geology structure.

5.6.2. Scale Dependence of Permeability

Scale dependence of hydraulic properties of rock mass/formation has been discussed at several

studies. Whitaker and Smart (2010) suggests the scale dependence of hydraulic conductivity for the Carbonate aquifers in the Bahamas. Although the hydraulic conductivity values were estimated in a different ways, the value increases linearly with scale size. Becker and Davis (2003) also compiled permeabilities obtained by several methods including injection tests and geothermal simulations for the upper crust of the Juan de Fuca Ridge. Generally, the permeabilities estimated from laboratory experiments are relatively small, in contrast, the values obtained from numerical simulation tend to be large. The dependence of permeability is not only on scale size but also depends on depth and formation age, which has been previously reported (Fisher et al., 1998; Becker and Davis, 2003). Compiled permeabilities for the Juan de Fuca Ridge show that permeabilities of great depth have small values which corresponds with the effects of normal stress and associated porosity (Fisher et al., 1998).

The Nankai subduction zone is a suitable site for investigation of the scale dependence of permeability because laboratory experiments using core samples and in situ measurement of permeability have been performed at our study site (e.g., Dugan and Daigle, 2011; Saffer et al., 2013). We compared our results with previous studies which estimated permeabilities from laboratory experiments (Guo et al., 2011; Valdez et al. (unpublished)), single hole experiments including SP (Single-Probe), DD (Draw Down) and HF (Hydraulic Fracture) experiments (Saffer et al., 2011; Boutt et al., 2012; Saffer et al., 2013). In addition to the data of Site C0002, we added the data of Site C0009, where geological units correspond to those at Site C0002 (Expedition 319 Scientists, 2010). P-wave

velocities from physical logging data also suggest a similarity of geological feature for the two sites (Expedition 314 Scientists, 2009; Expedition 319 Scientists, 2010).

Guo et al. (2011) conducted uniaxial CRSC (Constant Rate-of-Strain Consolidation) tests for 10 samples of Site C0002, which are from the shallow region of the Kumano basin ~920 mbsf. For the deeper portions corresponding to the accretionary prism at 1200-1250 mbsf, Valdez et al. (unpublished) performed CRSC tests on 6 samples of Site C0009. The range of permeabilities estimated from the above laboratory experiments assuming in situ effective normal stress is 2.5×10^{-18} - 5.3×10^{-17} m^2.

Boutt et al. (2012) and Saffer et al. (2013) performed the DD, HD, and SP tests using the Schlumberger's Modular Formation Dynamics Tester tool (MDT) at Site C0009 during Expedition 319 in 2009 (Expedition 319 Scientists, 2010). The DD and HD tests were performed at 1539.2–1540.2 mbsf corresponding to the accretionary prism, and utilized packers to produce an isolated region in the borehole. Permeability can be estimated from the response of pressure to injected fluids in the isolated section. The tests gave permeabilities of 6.0×10^{-17} - 1.2×10^{-16} m^2, and 1.5×10^{-15} - 5.5×10^{-15} m^2, respectively (Boutt et al., 2012). Whereas six SP tests were conducted at 729.9-1464.9 mbsf which yielded permeabilities of 6.5×10^{-17} - 1.9×10^{-14} m^2 (Saffer et al., 2013).

In addition, we estimated the permeability from pore pressure response to the tidal loading (See Chapter 4). The values of loading efficiency estimated from the P1 and P3 records are 0.64. This can

be calculated from the ratio between reference pressure (P4) and pore pressure in the formation (P1 or P3). We observed no phase lag in the P1 and P3 records relative to reference pressure which is similar to the observatory at Hole C0010A located 11 km away from Hole C0002G (Fig. 5.1(a); Chapter 4). The absence of phase lags indicates that changes in pore pressure in formation propagate to borehole without fluid diffusion. As in Chapter 4, we assumed that pressure communication between the formation and borehole maintains an undrained condition, and dissolved gas in interstitial water produces amplitude (loading efficiency) damping. By assuming the presence of methane gas as described in Chapter 4 and using the physical properties of Site C0002 shown in Table 5.2, we obtained a gas fraction of 1.0 %, which is required to produce a loading efficiency of 0.64. The value of the formation-instrument compressibility ratio of LTBMS ($\beta_D = 23.8$), 100 % amplitude response and no phase lag offer a hydraulic diffusivity $> 1.2 \times 10^{-5}$ m^2/s (6.1×10^{-13} m^2: assuming no gas dissolution; Fig. 5.6).

The collected permeabilities were estimated by several methods for different scales. The compiled results (Fig. 5.6) show a scale dependence of permeability with larger scales, having larger permeabilities. There may be two trends in the complied results because the degree of unit consolidation is different between accretionary prism and Kumano basin. Generally the former is more robust than latter (Saffer et al., 2013), but we could not distinguish different trends in our data set (Fig. 5.7). A variation of permeability of 2-3 orders of magnitude is often generated which may mask such

trends.

Cross-hole tests representing distances of about 100 m show the largest permeabilties, in contrast, laboratory experiments on samples the size of millimeters to centimeters show the smallest values. Estimation using tidal loading gives minimum possible permeabilities because there are no phase lags, and the arrows above stars in Fig. 5.7 denote that the values may be higher than shown permeabilities. Furthermore, scale definition of tidal loading is difficult, and horizontal arrows below stars indicate that the dimension is undefined.

The scale dependence of permeability may be produced by the increasing in sized and numbers of cracks and faults associated with complicated structures. In a large complicated rock mass, it is likely that fluids find a high permeability path by flowing through various cracks and deformations, so the estimated permeability from fluid flow will be quite high. In contrast, experimental measurements on small scales samples may be more representative of the competent portions of the rock, and not the pathways through which the fluid flows. Currently, we cannot provide a definitive explanation for the scale dependence of the permeabilities but understanding these values in terms of the geologic structure will contribute to the understanding of the fluid properties in the fault zone and associated evaluation of stress conditions.

Table 5.2. Definitions and values of variable used for the calculation of permeability based on tidal loading.

Variable	Definition	Dimension	
		P1 (980 bsf)	P3 (780 mbsf)
γ	Average 1-D Loading efficiency	0.64	
β_f	Formation compressibility, Pa^{-1}	5.0×10^{-9}	
β_f'	vertical formation compressibility,	2.0×10^{-9}	
β_w	Fluid compressibility, Pa^{-1}	4.0×10^{-10}	
β_{steel}	Steel compressibility, Pa^{-1}	5.0×10^{-12}	
β^*	Instrument compressibility, Pa^{-1}	3.4×10^{-10}	
β_D	Formation-instrument compressibility ratio	23.8	
n	Porosity	0.37	0.35
v	Poisson ratio	0.10	
r_{to}	Tubing outer radius, m	0.0445	
r_{ci}	Casing inner radius, m	0.1122	
r_{co}	Casing outer radius, m	0.1222	
r_{so}	Screen outer radius, m	0.1422	
H	Observatory system Length, m	43.0	69.1
h	Screen part length, m	43.0	18.6
V_w	Volume of water, m^3	1.43	2.30
V_{steel}	Volume of steel part, m^3	0.28	0.45
V	Total volume, m^3	1.71	2.75
μ	Fluid viscosity, Pa·s	1.0×10^{-3}	
$P(r,t)$	Pressure, Pa		
P_D	Dimensionless pressure		
r	Distance, m		
r_D	Dimensionless distance		
t	time, s		
t_D	Dimensionless time		
f	Frequency, rad		
f_D	Dimensionless frequency		
S_D	Dimensionless fluid source term		
A	Amplitude, %		
ζ	Phase lag, rad		

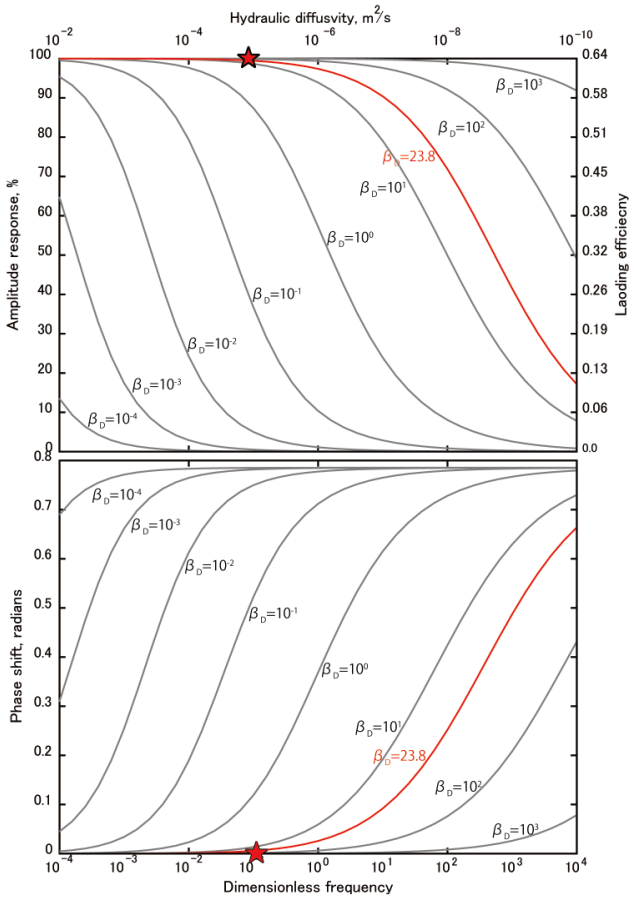

Figure 5.6. Predicted amplitude (A) and phase lag (ζ) in formation pressure relative to reference pressure as a function of hydraulic diffusivity (top axis) and as a function of dimensionless frequency (bottom axis; $f_D = \frac{r_{so}^2 f}{c}$). Several values of formation and instrument compressibility ratio (β_D) are shown; for a given period, hydraulic diffusivity can be estimated from a known compressibility ratio and observed phase lag and/or amplitude damping. Red stars are our observations which show 100% amplitude response of formation pressure to the reference pressure and zero phase lag (See the details in Chapter 4). Then, we obtained a hydraulic diffusivity > 1.2×10^{-5} m^2/s for the LTBMS, β_D=23.8.

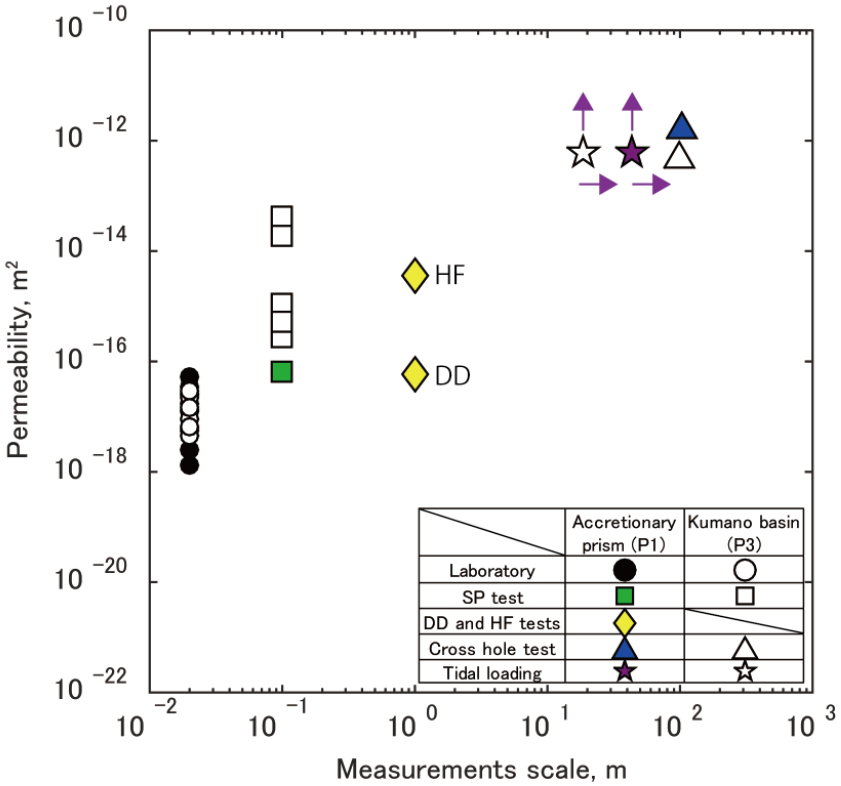

Figure 5.7. Scale dependence of permeability. Permeabilities estimated from several methods are shown. Circles are laboratory experiments, squares are Single-Probe tests, diamonds are Draw-Down and Hydraulic Fracture tests, triangles are Cross-hole tests and stars are for tidal loading, respectively. Filled symbols indicate the permeabilities corresponding to P1 depth (937 mbsf) and open symbols are for the P3 depth (757 mbsf). For the permeability estimated from tidal loading, we could not determine the exact values because there is no phase lag between tidal loading and formation pressure. The vertical arrows above the stars indicate possibly larger permeability since no phase lag is observed. The horizontal arrows below the stars indicate that it is difficult to define the scale of tidal loading.

5.7. Summary

In situ measurement of permeability at offshore sites using multiple boreholes is difficult and rare, however, the pressure records of LTBMS, which detected the nearby drilling and coring operations,

unexpectedly enabled estimates for the permeability at a scale of about 100 m. In addition, pressure response to the tidal loading gives the permeability on a different larger scale. Combining these results with other experimental tests for permeability on smaller scales, we can see differences in the permeability over different scale length. Combining data analyses of pressure response to drilling and tides with experimental results on core samples, show the power of integrating results over many scale lengths and is a great example of interdisciplinary investigations of the NanTroSEIZE project.

Chapter 6. Conclusions

Borehole monitoring at onshore and offshore sites have recorded valuable data, which help our understanding of hydrological systems of the subsurface. There are many previous studies that reported changes in pressure and water level associated with earthquakes (e.g., Roellofs, 1996; Brown et al., 2005; Wang and Manga, 2010a), and the recent increase in borehole observations reflects the importance of these studies. However, the mechanisms of the hydrological perturbations have not been well established and there are still many unresolved issues. An important scientific objective is the elucidation of relationships between seismic processes and fluids effects, and as a first step the mechanisms of subsurface hydrological perturbations have to be understood.

In this thesis, I mainly described borehole pressure and water level data. Not only coseismic and preseismic responses, but also estimates of physical properties of the rock mass such as hydraulic diffusivity. By integrating seismic, geological and hydrological data, several mechanisms were proposed that can illustrate changes in pressure (water level), physical properties of rock mass and time dependent recovery (Fig. 6.1).

In Chapter 2, we estimated time series of physical properties of the local rock mass using tidal responses of pore pressure and groundwater level, and showed clear changes at the time of the 2011 Tohoku earthquake. Some previous studies reported coseismic changes in tidal response that were detected within 300 km from the epicenter, and they concluded that the main cause is dynamic stress

associated with seismic waves (e.g., Elkhoury et al., 2006). In contrast, we obtained large changes in tidal responses at 500-1000 km away from the epicenter. The detailed analyses suggest that the static strains produced by the mainshock was large enough to affect the hydrological systems located within 500-600 km from the epicenter. This is the first and unique observation of large effects of static strains on physical properties of rock mass have been observed. In contrast, the dynamic strains might have been dominant at more than 700-800 km distances.

In Chapter 3, we described the preferential hydrological perturbations in the subsurface. One of our study sites (Site KST) shows a similar response to several earthquakes, that is an exponential increase in groundwater level and subsequent decrease associated with fluids diffusion. We searched for the location of the diffusion source in the aquifer, and magnitude of change in water head there produced by the earthquakes. Although the amount of change in groundwater level and required time for the change are different for each earthquake, the estimated sources were located at almost the same distance ~20 m from observation site. Geological features of Site KST suggest that water flow from the mountain to the borehole was triggered by the earthquakes. Similar recovery of water level also implies that there is a preferential hydrological condition and the disturbed subsurface hydrology tends to return to that condition.

In Chapter 4, we investigated changes in pore pressure observed at an oceanic borehole located in the Nankai subduction zone, Japan. In most cases, the hydrological perturbations produced by

earthquakes were characterized by increases in pressure and decreases in loading efficiency (the same quantity with tidal response in Chapter 2). The fact that there is no observed phase lag in formation pressure relative to the tidal loading, is a key to revealing the mechanism. We suggest that the amplitude damping of the formation pressure is caused by the stiffness of the formation, not by fluids diffusion. We focused on characteristics of gas which is highly compressible, and proposed that small amount of gas can easily produce change in the stiffness of formation. The behavior of gas, such as exsolution and dissolution depending on ambient pressure, can explain the coseismic increase in pressure, decrease in loading efficiency and recovery processes. Our proposed explanation is important because it can avoid misinterpretation that large changes in pressure always reflect great amount of damage in the formation.

In Chapter 5, we estimated in situ permeability for the Kumano basin and accretionary prism in the Nankai subduction zone at the 100 m scale by utilizing pressure perturbations produced by drilling operation at nearby sites. Model simulations based on the diffusion equation fit well with observed pressure perturbations. In addition, comparing with previous studies, a scale dependence of permeability was derived, which indicates a higher permeability for larger scales. This trend may suggest increases in size and number of cracks and faults with mass scale. These results can be used to simulate the permeability at the fault scale, which would lead to estimation of local stress condition on the fault.

The studies presented in this thesis verify the ability and utility of borehole observations for understanding the subsurface hydrological conditions. Estimation of physical properties of rock mass using tidal response enables continuous observations without any anthropogenic disturbances. We used onshore and offshore borehole data, but the fundamental features are the same and show the great dependency of site-characteristics. It is difficult to clearly distinguish the effects of static and dynamic strains, but we are able to provide detailed mechanisms of hydrological perturbations from several types of data.

There still remain difficulties in borehole observations, such as the limitation of borehole depth and definition of monitoring region. It is also a problem how the data observed in a borehole can be extrapolated to greater depths of the seismogenic zone. In terms of understanding the earthquake sources, the advance of borehole observations in the ocean floor provides solutions for overcoming the depth limitation, because very low frequency earthquakes (VLFEs) and slow slip events (SSEs) have been observed at relatively shallow depths < 10-12 km in the Nankai subduction zone (e.g., Ito and Obara, 2006; Sugioka et al., 2012). Because of the expense and logistical complications, we cannot construct as many boreholes observatories as we would like to rapidly advance this field, so integrated studies and interpretations for the available data are required. Many borehole observation sites have introduced multiple instruments that record a wide variety of measurements, and the contribution of combining these data is excitedly anticipated. This thesis is a first step in combining geophysical and

geological borehole observations for a better understanding of the subsurface hydrology and its association with on stress changes and rock mass properties, as related to seismic events.

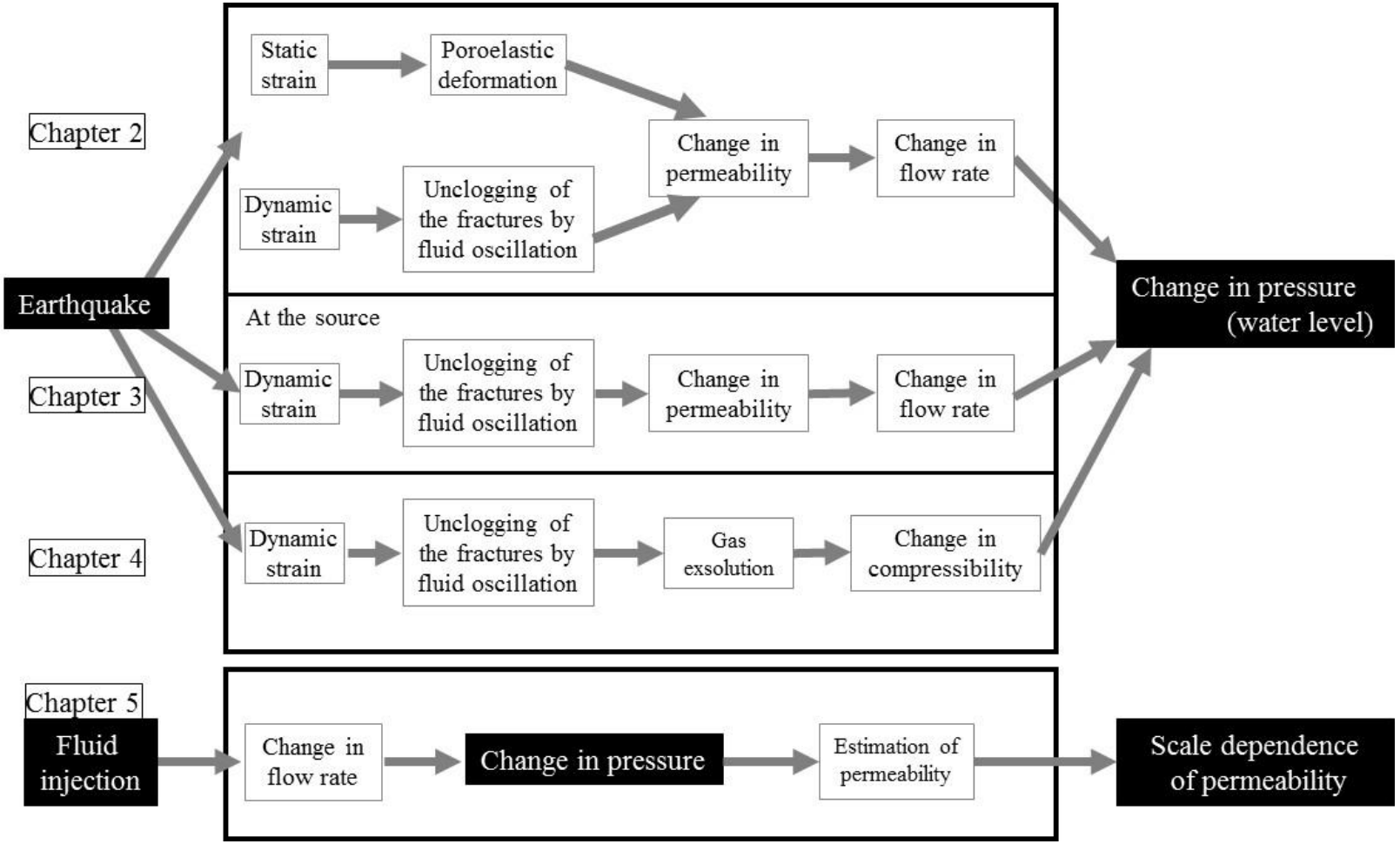

Figure 6.1. Diagram showing various processes for hydrological perturbations that are discussed in the chapters of this thesis.

Citations for published work

Chapter 2 has been published as follows:

Kinoshita, C., Y. Kano, and H. Ito (2015), Shallow crustal permeability enhancement in central Japan due to the 2011 Tohoku earthquake, *Geophysical Research Letters*, 42, doi:10.1002/2014GL062792.

Chapter 4 has been submitted as follows:

Kinoshita, C., D. Saffer, A. Kopf, A. Rosner, L. M., Wallace, E. Araki, T. Kimura, Y. Machida, R. Kobayashi, E. Davis, S. Toczko, S. Carr (2017), Changes in physical properties of the Nankai Trough megasplay fault induced by earthquakes, detected by continuous pressure monitoring, *Journal of Geophysical Research.*

References

Akaike, H. (1980), Likelihood and the Bayes procedure, in"Bayesian Statistics", ed. by J. M. Bernardo, M. H. DeGroot, D. V. Lindley and A. F. M. Smith, University Press, Valencia,143-166.

Aoki, Y., T. Tamano and S. Kato (1982), Detailed structure of the Nankai Trough from migrated seismic sections, *In Studies in Continental Margin Geology*, edited by J. S. Watkins and C. L. Drake, AAPG Mem., 34, 309–322.

Araki, E., D. M. Saffer, A. J. Kopf, L. M. Wallace, T. Kimura, Y. Machida, S. Ide, E. Davis, IODP Expedition 365 shipboard scientists (2017), Recurring and triggered slow-slip events near the trench at the Nankai Trough subduction megathrust, *Science*, 356, 1157-1160.

Becker, K. and E. E. Davis (2005), A review of CORK designs and operations during the Ocean Drilling Program. In Fisher, A. T., Urabe, T., Klaus, A., and the Expedition 301 Scientists, *Proc. IODP*, 301: College Station TX (Integrated Ocean Drilling Program Management International, Inc.), doi:10.2204/iodp.proc.301.104.2005.

Bekins, B. A., A. M. McCaffrey and S. J. Dreiss (1995), Episodic and constant flow models for the origin of low-chloride waters in a modern accretionary complex, *Water Resour. Res.*, 31, 3205-3215.

Boutt, D. F., D. Saffer, M.-L. Doan, W. Lin, T. Ito, Y. Kano, P. Flemings, L. C. McNeill, T. Byrne, N. W. Hayman, and K. T. Moe (2012), Scale dependence of in-situ permeability measurements in the Nankai accretionary prism: The role of fractures, *Geophys. Res. Lett.*, 39, L07302, doi:10.1029/2012GL051216.

Brodsky, E. E., E. Roeloffs, D. Woodcock, I. Gall, and M. Manga (2003), A mechanism for sustained groundwater pressure changes induced by distant earthquakes, *J. Geophys. Res.*, 108(B8), 2390.

Brodsky, E.E. and S. Prejean (2005), New constraints on mechanisms of remotely triggered seismicity at Long Valley Caldera, *J. Geophys. Res.*, 110, B04302.

Brown, K. M., M. D. Tryon, H. R. Deshon, L. M. Dorman, S. Y. Schwartz (2005), Correlated transient fluid pulsing and seismic tremor in the Costa Rica subduction zone., *Earth Planet. Sci. Lett.*, 238, 189 - 203.

Candela, T., E. E. Brodsky, C. Marone and D. Elsworth (2014), Laboratory evidence for particle mobilization as a mechanism for permeability enhancement via dynamic stressing, *Earth Planet. Sci. Lett.*, 392, 279-291.

Carslaw, H. S., and J. C. Jaeger (1959), *Conduction of Heat in Solids*, Oxford: Clarendon Press.

Chadha, R. K., C. Singh and M. Shekar (2008), Short note: transient changes in well-water level in bore wells in Western India due to the 2004 Mw 9.3 Sumatra earthquake, *Bull. Seismol. Soc. Am.*, 98(5), 2553–2558.

Cox, S. C., H. K. Rutter, A.Sims, M. Manga, J. J. Wier, T. Ezzy, P. A.White, T. W. Horton and D. Scott (2012), Hydrological effects of the Mw7.1 Darfield (Canterbury) earthquake, 4 September 2010,

New Zealand, *New Zealand Journal of Geology and Geophysics*, 55, 231–47.

Davis, E. E., K. Becker, K. Wang and M. Kinoshita (2009), Co-seismic and post-seismic pore-fluid pressure changes in the Philippine Sea plate and Nankai decollement in response to a seismogenic strain event off Kii Peninsula, Japan, *Earth Planets Space*, 61, 649–657.

Davis, E. E., M. Heesemann and K. Wang (2011), Evidence for episodic aseismic slip across the subduction seismogenic zone off Costa Rica: CORK borehole pressure, observations at the subduction prism toe, *Earth Planet. Sci. Lett*., 306, 299-305.

Davis, E. E., M. Kinoshita, K. Becker, K. Wang, Y. Asano and Y. Ito (2013), Episodic deformation and inferred slow slip at the Nankai subduction zone during the first decade of CORK borehole pressure and VLFE monitoring, *Earth Planet. Sci. Lett.*, 368, 110–118.

Detournay, D. and A. Cheng (1993), Fundamentals of poroelasticity. In: Fairhurst, C. (Ed.), Comprehensive Rock Engineering, Pergamon, 113–171.

Doan, M. L. and F. H., Cornet (2007), Small pressure drop near a fault induced by small teleseismic waves, *Earth planet. Sci. Lett.*, 258, 207-218.

Dugan, B. and H. Daigle (2011), Data report: permeability, compressibility, stress state, and grain size of shallow sediments from Sites C0004, C0006, C0007, and C0008 of the Nankai accretionary complex. *Proc. IODP, 314/315/316*, Tokyo.

Elkhoury, J. E., E. E., Brodsky and D. C. Agnew (2006), Seismic waves increase permeability, *Nature*, 441, 1135–1138.

Elkhoury, J. E., A. Niemeijer, E. E. Brodsky and C. Marone (2011), Laboratory observations of permeability enhancement by fluid pressure oscillation of in situ fractured rock, *J. Geophys. Res.*, 116, B02311, doi:10.1029/2010JB007759.

Expedition 314 Scientists (2009), Site C0002, *Proc. IODP*, 314, Tokyo.

Expedition 315 Scientists (2009), Site C0002, *Proc. IODP*, 315, Tokyo.

Expedition 319 Scientists (2010), Site C0010, *Proc. IODP*, 319, Tokyo.

Expedition 332 Scientists (2011a), The SmartPlug and GeniusPlug: simple retrievable observatory systems for NanTroSEIZE borehole monitoring, *Proc. IODP*, 332, Tokyo.

Expedition 332 Scientists (2011b), Methods, *Proc. IODP, 332*, Tokyo.

Expedition 332 Scientists (2011c). Site C0010, *Proc. IODP*, 332, Tokyo.

Expedition 332 Scientists (2011d). Site C0002, *Proc. IODP*, 332, Tokyo.

Finn, W. D. L. (1981), Liquefaction Potential: Development since 1976, P*roc. International Conference on Recent Advances in Geotechnical Engineering and Soil Dynamics*, St. Louis, Missouri, 655 -681.

Fisher A. T. and M. W. Hounslow (1990), Transient fluid flow through the toe of the Barbados accretionary complex: constraints from Ocean Drilling Program Leg 110: heat flow studies and simple models, *J. Geophys. Res.*, 95, 8845–58.

Fisher, A. T. and G. Zwart (1997), Packer experiments along the decollement of the Barbados accretionary complex: Measurements of in situ permeability, *Proc. Ocean Drill. Program*, Sci. Results, 156, 199-218.

Fisher, A. T., E. E. Davis, and K. Becker (2008), Borehole-to-borehole hydrologic response across 2.4 km in the upper oceanic crust: Implications for crustal‐scale properties, J. *Geophys. Res.*, 113, B07106, doi:10.1029/2007JB005447.

Fukuyama, E., M. Ishida, D. S. Dreger and H. Kawai (1998), Automated seismic moment tensor determination by using on –line broadband seismic waveforms, *Zishin 2*, 51, 149-156 (in Japanese).

Geothermal Engineering Co., Ltd (2008), Construction of groundwater water observatories for predictions of the Tonankai and Nankai earthquakes, Geothermal Engineering Co., Ltd (in Japanese).

Gibson, R. E. (1958), The progress of consolidation in a clay layer increasing in thickness with time, *Geotechnique*, 8(4), 171–182.

Greene, H. G., J. G. Taggart, M. T. Ledbetter, R. Barminski, T. E. Chase, K. R. Hicks and C. Baxter (1991), Offshore and onshore liquefaction at Moss Landing spit, central California-Result of the October 17, 1989, Loma Prieta earthquake, *Geology*, 19, 945-949.

Guo, J., W. Likos, M. Underwood, R. Skarbek, N. Adamson, D. Saffer (2011), Data report: consolidation characteristics of sediments from Sites C0002, C0006, and C0007, IODP Expeditions 315 and 316, NanTroSEIZE Stage 1, *Proc. IODP*, 314/315/316, Washington, DC.

Hammerschmidt, S., E. E. Davis and A. Kopf (2013a), Fluid pressure and temperature transients detected at the Nankai Trough Megasplay Fault: Results from the SmartPlug borehole observatory, *Tectonics*, 600, 116-133.

Hammerschmidt, S. B., E. E. Davis, A. Hüpers and A. Kopf (2013b), Limitation of fluid flow at the Nankai Trough megasplay fault zone, *Geo-Mar. Lett.*, 33, 405-418.

Hirose, T., Y. Hiramatsu and K. Obara (2010), Characteristics of short‐term slow slip events estimated from deep low‐frequency tremors in Shikoku, Japan, *J. Geophys. Res.*, 115, B10304, doi:10.1029/2010JB007608.

Hsieh, P., J. Bredehoeft and J. Farr (1987), Determination of aquifer transmissivity from earth tide analysis, *Water Resour. Res.*, 23, 1824-1832.

Hubbert, M. K., and W. W. Rubey (1959), Role of fluid pressure in mechanics of overthrust faulting, *Geol. Soc. Am. Bull.*, 70, 115– 166.

Hydrographic Bureau (1948), Report on the Nankai earthquake in 1946 (Change of the land surface and damage), *Hydrogr. Bull. Spec*. Number, 201, 117 (in Japanese).

Igarashi, G. and H. Wakita (1991), Tidal responses and earthquake-related changes in the water level of deep wells, *J. Geophys. Res.*, 96, 4269-4278.

Ikari, M. J. and D. M. Saffer (2012), Permeability contrasts between sheared and normally

consolidated sediments in the Nankai accretionary prism, *Marine geology*, 295–298, 15, 1–13.

Imakiire, T., and T. Kobayashi (2011), The crustal deformation and fault model of the 2011 off the Pacific coast of Tohoku earthquake, *Bull. GSI*, 59, 21–30.

Ishihara, K. (1985), Stability of Natural Deposits During Earthquakes, *Proc. International Conference on Soil Mechanics and Foundation Engineering*, San Francisco, 1, 321-376.

Itaba, S. and N. Koizumi (2007), Earthquake-related changes in groundwater levels at the Dogo hot spring, Japan, *Pure Appl. Geophys*. 164, 2397–2410.

Ito, Y. and K. Obara (2006), Dynamic deformation of the accretionary prism excites very low frequency earthquakes, *Geophys. Res. Lett.*, 33, L02311, doi:10.1029/2005GL025270.

Jonsson, S., P. Segall, R. Pedersen, and G. Bjornsson (2003), Post-earth-quake ground movements correlated to pore-pressure transients, *Nature*, 424, 179-182.

Kato, A., A. Sakaguchi, S. Yoshida, and H. Mochizuki (2003), Permeability measurements and precipitation sealing of basalt in an ancient exhumed fault of a subduction zone, *Bull. Earthquake Res. Inst. Univ. Tokyo*, 78, 83–89.

Kikuchi, M., M. Nakamura and K. Yoshikawa (2003), Source rupture processes of the 1944 Tonankai earthquake and the 1945 Mikawa earthquake derived from low-gain seismograms, *Earth Planets Space*, 55, 159-172.

Kilb, D. L., J. Gomberg and P. Bodin (2000), Triggering of earthquake aftershocks by dynamic stresses, *Nature*, 408, 570 – 574.

Kinoshita, C., Y. Kano and H. Ito (2015), Shallow crustal permeability enhancement in central Japan due to the 2011 Tohoku earthquake, *Geophys. Res. Lett.*, 42, doi:10.1002/2014GL062792.

Kinoshita, C., D. Saffer, A. Kopf, A. Rosner, L. M., Wallace, E. Araki, T. Kimura, Y. Machida, R. Kobayashi, E. Davis, S. Toczko, S. Carr (2017), Changes in physical properties of the Nankai Trough megasplay fault induced by earthquakes, detected by continuous pressure monitoring, J. Geophys. Res., (Under review).

Kinoshita, M., G. F. Moore and Y. N. Kido (2011), Heat flow estimated from BSR and IODP borehole data: Implication of recent uplift and erosion of the imbricate thrust zone in the Nankai Trough off Kumano, *Geochem. Geophys. Geosyst.*, 12, Q0AD18, doi:10.1029/2011GC003609.

Kitagawa, Y., N. Koizumi, M. Takahashi, N. Matsumoto and T. Sato (2006), Changes in groundwater levels or pressures associated with the 2004 earthquake off the west coast of northern Sumatra (M9.0), *Earth Planets Spac*e, 58, 173–179.

Kitagawa, Y. and N. Koizumi (2011), Changes in groundwater levels, groundwater pressures and discharge rates a day after the 2011 Off the Pacific Coast of Tohoku Earthquake (M9.0), Annual report on active fault and paleoearthquake researches, No.11, 309-318.

Kitagawa, Y. and N. Koizumi (2013), Detection of short-term slow slip events along the Nankai Trough via groundwater observations, *Geophysical Research Letters*, 40, 6079-6083.

Kitagawa, Y. and Y. Kano (2016), Changes in permeability of the Nojima fault damage zone inferred from repeated water injection experiments, *Earth Planets Space*, 68(185).

Koizumi, N. and C. Kinoshita (2017), Postseismic Well Water Level Increases at the Dogo Hot Spring in Japan, zisin2, 70, 125-134.

Kopf, A., D. Saffer, S. Toczko and the Expedition 365 Scientists (2016), International Ocean Discovery Program Expedition 365 Preliminary Report NanTroSEIZE Stage 3: Shallow Megasplay Long-Term Borehole Monitoring System (LTBMS), *Proc. IODP*, 365, Tokyo.

Lauer R. M. and Saffer D. M. (2012), Fluid budgets of subduction zone forearcs: the contribution of splay faults, *Geophys. Res. Lett.*, 39, L13604. http://dx.doi.org/10.1029/2012GL052182.

Lee, H.A. and N. C. Woo (2012), Influence of the M 9.0 Tohoku earthquake on groundwater in Korea, *Geosci. J.*, 16, 1-6.

Manga, M. (2001), Origin of coseismic and postseismic streamflow changes inferred from recession-flow analysis, *Geophysical Research Letters*, 28, 2133-2136.

Manga, M., Wang, C.-Y. and M. Shirzaei (2016), Increased stream discharge after the 3 September 2016 Mw 5.8 Pawnee, Oklahoma earthquake, *Geophys. Res. Lett.*, 43, doi: 10.1002/2016GL071268.

Matsumoto, K., T. Sato, T. Takanezawa, and M. Ooe (2001), GOTIC2: A program for computation of oceanic tidal loading effect, *J. Geod. Soc. Jpn.*, 47, 243–248.

Matsumoto, N., G. Kitagawa and E. A. Roeloffs (2003a), Hydrological response to earthquakes in the Haibara well, central Japan - I. Groundwater level changes revealed using state space decomposition of atmospheric pressure, rainfall and tidal responses, *Geophys. J. Int.*, 115, 885-898.

Matsumoto, N. and E. A. Roeloffs (2003b), Hydrological response to earthquakes in the Haibara well, central Japan – II. Possible mechanism inferred from time-varying hydraulic properties, *Geophys. J. Int.*, 155, 899-913.

Matsumoto, N. and N. Koizumi (2013), Recent Hydrological and Geochemical Researches for Earthquake Prediction in Japan, *Natural Hazards*, DOI:10.1007/s11069-011-9980-8.

McNeill, L., D. Saffer, T. Byrne, E. Araki, S. Toczko, N. Eguchi, K. Takahashi and the IODP Expedition 319 Scientists (2010), IODP Expedition 319, NanTroSEIZE Stage 2: first IODP riser drilling operations and observatory installation towards understanding subduction zone seismogenesis, *Sci. Drill.*, 10, 4-13.

Miyazaki, S. and K. Heki (2001), Crustal velocity field of southwest Japan: subduction and arc-arc collision, *J. Geophys. Res.*, 106, 4305–4326.

Miyazawa, M. (2011), Propagation of an earthquake triggering front from the 2011 Tohoku-Oki earthquake, *Geophys. Res. Lett.*, 38, L23307, doi:10.1029/2011GL049795.

Montgomery, D. R. and M. Manga (2003), Streamflow and Water Well Responses to Earthquakes,

Science, 300, 2047.

Moore, J. C., A. Mascle, E. Taylor, P. Andreieff, F. Alvarez, R. Barnes, C. Beck, J. Behrmann, G. Blanc, K. Brown, M. Clark, J. F., Dolan, A. Fisher, J. Gieskes, M. Hounslow, P. McLellan, K. Moran, Y. Ogawa, T. Sakai, J. Schoonmaker, P. Vrolijk, R. H. Wilkens and C. Williams (1988), Tectonics and hydrogeology of the northern Barbados Ridge: results from Ocean Drilling Program Leg 110, *Geol. Soc. Am. Bull.*,100:1578-1593.

Moore, G. F., N. L. Bangs, A. Taira, S. Kuramoto, E. Pangborn and H. J. Tobin (2007), Three-dimensional splay fault geometry and implications for tsunami generation, *Science*, 318, 1128-1131.

Moore, G. F., J.-O., Park, N. L. Bangs, S. P. Gulick, H. J. Tobin, Y. Nakamura, S. Sato, T. Tsuji, T. Yoro, H. Tanaka, S. Uraki, Y. Kido, Y. Sanada, S. Kuramoto and A. Taira (2009), Structural and seismic stratigraphic framework of the NanTroSEIZE Stage 1 transect, in NanTroSEIZE Project Stage 1, *Proc. IODP*, 314/315/316, Washington, DC.

Niwa, M., R.Takeuchi, H. Onoe, K. Tsuyuguchi, K. Asamori, K. Umeda and K. Sugihara (2012), Groundwater pressure changes in Cen-tral Japan induced by the 2011 off the Pacific coast of Tohoku Earthquake, *Geochem. Geophy. Geosy.*, 13, Q05020.

Okada, Y. (1992), Internal deformation due to shear and tensile faults in a half space, *Bull. Seismol. Soc. Am.*, 82, 1018–1040.

Onoue, K., Y. Umeda, K. Shigetomi, T. asada, Y. Hoso and K. Kondo (2005), Observations of groundwater in areas reported with the anomalous changes of water levels of wells prior to Showa Nankai Earthquake-Construction of data set-, *Disaster Prevention Research Institute annuals. B*,48, 185-190.

Park, J.-O., T. Tsuru, S. Kodaira, N. Takahashi, A. Nakanishi, S. Miura, Y. Kaneda and Y. Kono (2000), Out-of-sequence thrust faults developed in the coseismic slip zone of the 1946 Nankai earthquake (Mw=8.2) off Shikoku, southwest Japan, *Geophys. Res. Lett.*, 27, 1033-1036.

Roeloffs, E. A. (1996), Poroelastic techniques in the study of earthquake-related hydrologic phenomena, *Adv. Geophys.*, 37, 135–195.

Roeloffs, E. A. (1998), Persistent water level changes in a well near Parkfield, California, due to local and distant earthquakes, *J. Geophys. Res.*, 103, 869-889.

Rojstaczer, S. and S. Wolf (1992), Permeability changes associated with large earthquakes: an example from Loma Prieta, California, *Geology*, 20, 211-4.

Rutter, H. K., S. C. Cox, N. F. D. Ward and J. J. Weir (2016), Aquifer permeability change caused by a nearfield earthquake, Canterbury, New Zealand, *Water Resour. Res.*, 52, 8861–8878, doi:10.1002/2015WR018524.

Saffer, D.M. and H. J. Tobin (2011), Hydrogeology and mechanics of subduction zone forearcs: fluid flow and pore pressure, *Annual Review of Earth and Planetary Sciences*, 39, 157–186.

Saffer, D., J. Guo, M. B. Underwood, W. Likos, R. M. Skarbek, I. Song and M. Gildow (2011), Data report: consolidation, permeability, and fabric of sediments from the Nankai continental slope, IODP Sites C0001, C0008, and C0004, *Proc. IODP*, 314/315/316: Washington, DC.

Saffer, D. M, P. B. Flemings, D. Boutt, M.-L. Doan, T. Ito, L. McNeill, T. Byrne, M. Conin, W. Lin, Y. Kano, E. Araki, N. Eguchi and S. Toczko (2013), In situ stress and pore pressure in the Kumano forearc basin, offshore SW Honshu from down-hole measurements during riser drilling, *Geochem. Geophys. Geosyst.*, 14(5),1454–1470.

Saffer, D. M. (2015), The permeability of active subduction plate boundary faults, *Geofluids*, 15, 193–215.

Saffer, D., A. Kopf, S. Toczko and the Expedition 365 Scientists (2017), NanTroSEIZE Stage 3: Shallow Megasplay Long-Term Borehole Monitoring System, *Proc. IODP*, 365: College Station, TX (IODP).

Sawyer, A. H., P. Flemings, D. Elsworth and M. Kinoshita (2008), Response of submarine hydrologic monitoring instruments to formation pressure changes: theory and application to Nankai advanced CORKs, *J. Geophys. Res.*, 113, B01102.

Screaton E. J., D. R. Wuthrich and S. J. Dreiss (1990), Permeabilities, fluid pressures, and flow rates in the Barbados Ridge complex, *J. Geophys. Res.*, 95, 8997–9007.

Screaton, E. J., B. Carson and G. P. Lennon (1995), Hydrologic properties of a thrust fault within the Oregon accretionary prism, *J. Geophys. Res.*, 100, 20025-20035.

Screaton, E., B. Carson, E. Davis and K. Becker (2000), Permeability of a decollement zone: Results from a two-well experiment in the Barbados accretionary complex, *J. Geophys. Res*, 105, NO. B9, 21403-2, 410.

Seno T., S. Stein and A. E. Gripp (1993), A model for the motion of the Philippine Sea plate consistent with NUVEL-1 and geological data, *J. Geophys. Res.*, 98, 17941–17948.

Shih, C. F.-S., Y.-M. Wu and C.-H. Chang (2013), Significant coherence for groundwater and Rayleigh waves: evidence in spectral response of groundwater level in Taiwan using 2011 Tohoku earthquake, Japan, *J. Hydrol.* 486, 57–70.

Shipley, T. H., G. F. Moore, N. L. Bangs, J. C. Moore and P. L. Stoffa (1994), Seismically inferred dilatancy distribution, northern Barbados Ridge décollement: implications for fluid migration and fault strength, *Geology*, 22, 411-414.

Skarbek, R. M. and D. M. Saffer (2009), Pore pressure development beneath the décollement at the Nankai subduction zone: Implications for plate boundary fault strength and sediment dewatering, *J. Geophys. Res.*, 114, B07401. doi:10.1029/2008JB006205.

Spinelli, G. A., D. M. Saffer and M. B. Underwood (2006), Hydrogeologic responses to three-dimensional temperature variability, Costa Rica subduction margin, *J. Geophys. Res.*, 111, B04403.

Spinelli, G. A. and K. Wang (2008), Effects of fluid circulation in subducting crust on Nankai margin

seismogenic zone temperatures, *Geology*, 36(11), 887-90.

Strasser, M., G. F. Moore, G. Kimura, Y. Kitamura, A. J. Kopf, S. Lallemant, J.-O. Park, E. J. Screaton, X. Su, M. B. Underwood and X. Zhao (2009), Origin and evolution of a splay fault in the Nankai accretionary wedge, *Nature Geoscience*, 2, 648 – 652.

Sugioka, H., T. Okamoto, T. Nakamura, Y. Ishihara, A. Ito, K. Obana, M. Kinoshita, K. Nakahigashi, M. Shinohara and Y. Fukao (2012), Tsunamigenic potential of the shallow subduction plate boundary inferred from slow seismic slip, *Nature Geoscience*, 5, 414-418.

Tamura, Y., T. Sato, M. Ooe, and M. Ishiguro (1991), A procedure for tidal analysis with a Bayesian information criterion, *Geophys. J. Int.*, 104, 507–516.

Valdez, R. et al., The results of CRSC tests (Unpublished data).

Vorhis, R. C. (1967), Hydrologic effects of the earthquake of March 27, 1964, outside Alaska, *U.S. Geological Survey Professional Paper,* 544-C, 54.

Wada, H. and K. Ito (1995), Seismic activity in the vicinity of the Atotsugawa fault, central Japan, *Annual. Disas. Prev. Res. Inst., Kyoto. Univ.,* No.38 B-1 (in Japanese).

Wallace, L. W., E. Araki, D. Saffer, X. Wang, A. Roesner, A. Kopf, A. Nakanishi, W. Power, R. Kobayashi, C. Kinoshita, S. Toczko, T. Kimura, Y. Machida and S. Carr (2016), Near-field observations of an offshore Mw 6.0 earthquake from an integrated seafloor and subseafloor monitoring network at the Nankai Trough, southwest Japan, *J. Geophys. Res.*, 121, 8338–8351.

Waller, R. (1966), Effects of the March 1964 Alaska earthquake on the hydrology of south-central Alaska. U.S., *Geological Survey Professional Paper*, 544-A.

Wang, C.-Y., A. Wong, D. S. Dreger, M. Manga (2006), Liquefaction limit during earthquakes and underground explosions: implications on ground-motion attenuation, *Bull.Seismol. Soc. Am.*, 96, 355–363.

Wang, C.-Y. (2007), Liquefaction beyond the nearfield, *Seismol. Res. Lett.*, 78, 512–517.

Wang, C.-Y. and M. Manga (2010a), Earthquakes and water, *in Lecture Notes in Earth Science*, J. Reitner, M. H. Trauth, K. Stuwe, and D.Yuan (Editors), Springer, Berlin, Germany.

Wang, C.-Y. and M. Manga (2010b), Hydrologic responses to earthquakes a general metric, *Geofluids*, 10, 206-216.

Wang, C.-Y., M. Manga, M. Shirzaei, M. Weingarten and L.-P. Wang (2017), Induced seismicity in Oklahoma affects shallow groundwater, *Seismol. Res. Lett.*, 88.

Wang, F. H. (2000), Theory, of Linear Poroelasticity, Princeton University Press.

Wang, K. and E. E. Davis (1996), Theory for the propagation of tidally induced pore pressure variations in layered subseafloor formations, *J. Geophys. Res.*, 101, 11483–11495.

Wang, K., E. E. Davis and G. Kamp (1998), Theory for the effects of free gas in subsea formations on tidal pore pressure variations and seafloor displacements, *J. Geophys. Res.*, 103, 12339-12353.

Wang, K. (2004), Applying fundamental principles and mathematical models to understand processes

and estimate parameters, In Davis, E. E. and H. Elderfield, eds., *Hydrogeology of the ocean lithosphere*: New York, Cambridge University Press, 376-413.

Wessel, P. and W. H. F. Smith (1991), Free software helps map and display data, *Eos Trans. AGU*, 72, 445-446.

Woodcock, D. and E. Roeloffs (1996), Seismically induced water-level oscillation in a fractured-rock aquifer well near Grants Pass, Oregon, *Oregon Geology*, 58, 27–33.

Xue, L., H-B, Li, E. E. Brodsky, Z.-Q. Xu, Y. Kano, H. Wang, J. J. Mori, J.-L. Si, J.-L. Pei, W. Zhang, G. Yang, Z.-M. Sun, and Y. Huang (2013), Continuous permeability measurements record healing inside the Wenchuan earthquake fault zone, *Science*, 340, 1555–1559.

Yasuda, S., I. Towhata, I. Ishii, S. Sato and T. Uchimura (2013), Liquefaction-induced damage to structures during the 2011 great east Japan earthquake, *Journal of JSCE*, 1, 181-193.

Yoshida, S., Y. Takahashi and Y. Nshioka (1995), Geology of western Tsu – Report of local geology research (A scale of 1 to 50000), *Geological Survey of Japan*, 128(in Japanese).

Yoshimatsu, T., S. Nakaya and K. Terai (1999), Geology and thermal water of Kii Peninsula, Japan, *Urban Kubota*, 38, 56 (in Japanese).

Acknowledgements

I would like to give special thanks to Professors Yasuyuki Kano and James J. Mori for their support. They spared a lot of time to discuss with me despite their busy schedules, and gave me opportunities to join the conferences. I discussed a lot of scientists and can expand my research community. Their supports and valuable advices have improved my quantification as a scientist.

Professor Naoji Koizumi has taught me hydrogeology since I started this research, which helps my understanding of the data and results. Tectono-Hydrology Research Group, AIST provided me their borehole data and Doctors Norio Matsumoto, Yuichi Kitagawa and Satoshi Itaba discussed with me and explained the details of borehole monitoring. Professor Demian Saffer readily complied with my request that being a host of my visiting scholarship for a year. His support to my research still continues. I and Doctor Hisao Ito discussed a lot for my paper of Geophysical Research Letters, and his useful comments improved my paper. I also thank to my colleagues and friends for their encouragements. My parents trust me and has supported for long time. I would like to be nice to them.

This study was partly supported by MEXT KANAME grant (KAkenhi for NAnkai Megathrust Earthquakes 21107006) and Observation and Research Program for Prediction of Earthquakes and Volcanic Eruption. The mining section of Kamioka mine provided technical support for our measurement. I also acknowledge funding by the German Science Foundation (DFG grant KO2108/8-

1) and the Geological Survey of Canada for the GeniusPlug work, NSF grants OCE-0623633 and OCE-1334436 to Professor Demian Saffer supporting the pressure instrumentation and the efforts of Integrated Ocean Drilling Program (IODP) members. The Kyoto University Foundation supported my visiting scholarship and gave me opportunities to discuss with scientists who are specialists of my research field.

We used the F-net and focal mechanism Catalog operated by the National Research Institute for Earth Science and Disaster Prevention, and obtained seismic data of DONET from the Hi-net website. For preparation of figures, we used the Generic Mapping Tools (GMT) software (Wessel and Smith, 1991).